THESIS FOR THE DEGREE OF DOCTOR OF PHILOSOPHY

Polarization in the ELAIS-N1 LOFAR Deep Field

Sara Piras

Department of Space, Earth, and Environment
Chalmers University of Technology
Gothenburg, Sweden, 2024

Polarization in the ELAIS-N1 LOFAR Deep Field

Sara Piras

Copyright © 2024 Sara Piras
All rights reserved.

ISBN: 978-91-8103-129-4
Doktorsavhandlingar vid Chalmers tekniska högskola
Ny series nr 5587
ISSN 0346-718X
This thesis has been prepared using LaTeX.

Department of Space, Earth, and Environment
Chalmers University of Technology
SE-412 96 Gothenburg, Sweden
Phone: +46 (0)31 772 1000
www.chalmers.se

Printed by Chalmers Reproservice
Gothenburg, Sweden, December 2024

Abstract

The physical characteristics of cosmic magnetic fields are encoded in the polarization properties of extragalactic radio sources. Linearly polarized radiation undergoes Faraday rotation as it crosses a magneto-ionic medium, and the rotation of the polarization angle of the signal is equal to its wavelength squared times the Rotation Measure (RM). The RM is in turn proportional to the line-of-sight integral of the product of the magnetic field component along the line of sight and the density of thermal electrons. Mapping the values of the RM across the sky provides a means to constrain cosmic magnetic fields. For this purpose, statistical studies of the properties of polarized radio sources spread over cosmological distances are essential.

Low radio-frequency observations provide better precision on the inferred RM values than higher-frequency ones. On the other hand, low radio-frequency observations are more affected by depolarization, which affects the detection rate of polarized sources. The population of faint polarized extragalactic sources at low radio-frequency is still mostly unknown. In this context, the LOw Frequency ARray (LOFAR) plays an important role because of the sensitivity, angular resolution and precision on the inferred RM values that can be achieved through low-frequency broad-band polarimetry, allowing us to study the polarized radio emission at around 150 MHz in unprecedented detail.

In my work I have developed a new method to combine polarimetric observations made with slightly different frequency configurations and have then applied this method to LOFAR 115–177 MHz observations of the European Large Area ISO Survey-North 1 (ELAIS-N1) deep field, one of the deepest LOFAR Two-Metre Sky Survey (LoTSS) deep fields imaged so far. Within this field an area of 25 deg^2 was imaged at $6''$ of resolution. By combining 19 datasets each of eight-hour-long duration, I detected 33 polarized components, which corresponds to an average number density of 1.3 polarized component per square degree. This represents the deepest and highest-resolution polarization study at 150 MHz to date. I compared the results with other RM catalogs, quantified the depolarization properties of sources detected also at 1.4 GHz, and modeled the source counts in polarization from the counts in total flux density. The detected polarized sources were fully characterized and analyzed, and the extragalactic environment was investigated.

This work addresses both the technical and theoretical challenges in observing and interpreting low-frequency polarimetric data. It marks a significant

step in solving some of the complex issues modern radio astronomy faces, especially those related to processing the large amounts of data generated by new-generation radio interferometers.

Keywords: Polarization; galaxies: individual (ELAIS-N1); radio continuum: galaxies; physical data and processes: magnetic fields, physical data and polarization; methods: numerical, observational; techniques: polarimetric

List of publications

This thesis is based on the following publications:

[A] **S. Piras**, C. Horellou, J. E. Conway, M. Thomasson, S. del Palacio, T. W. Shimwell, S. P. O'Sullivan, E. Carretti, I. Šnidarić, V. Jelić, B. Adebahr, A. Berger, P. N. Best, M. Brüggen, N. Herrera Ruiz, R. Paladino, I. Prandoni, J. Sabater, and V. Vacca, "LOFAR Deep Fields: Probing the sub-mJy regime of polarized extragalactic sources in ELAIS-N1. I. The catalog". *A&A*, vol. 687, A267, 2024. doi:10.1051/0004-6361/202349085.

[B] **S. Piras**, C. Horellou, J. E. Conway, M. Thomasson, S. del Palacio, T. W. Shimwell, S. P. O'Sullivan, E. Carretti, V. Vacca, A. Bonafede, and I. Prandoni, "LOFAR Deep Fields: Probing the sub-mJy regime of polarized extragalactic sources in ELAIS-N1. II. Analysis". Manuscript submitted to *A&A*.

Other publications by the author, not included in this thesis, are:

[C] I. Šnidarić, V. Jelić, M. Mevius , M. Brentjens, A. Erceg, T. W. Shimwell, **S. Piras**, C. Horellou , J. Sabater, P. N. Best, A. Bracco , L. Ceraj, M. Haverkorn, S. P. O'Sullivan, L. Turić, and V. Vacca, "LOFAR Deep Fields: Probing faint Galactic polarised emission in ELAIS-N1". *A&A*, vol. 674, A199, 2023. doi:10.1051/0004-6361/202245124.

[D] N. Herrera Ruiz, S. P. O'Sullivan, V. Vacca, V. Jelić, B. Nikiel-Wroczynski, S. Bourke, J. Sabater, R.-J. Dettmar, G. Heald, C. Horellou, **S. Piras**, C. Sobey, T. W. Shimwell, C. Tasse, M. J. Hardcastle, R. Kondapally, K. T. Chyży, M. Iacobelli, P. N. Best, M. Brüggen, E. Carretti, and I. Prandoni, "LOFAR Deep Fields: probing a broader population of polarized radio galaxies in ELAIS-N1". *A&A*, vol. 648, A12, 2021. doi:10.1051/0004-6361/202038896.

Acknowledgments

I would like to express my deep gratitude to my supervisor, Cathy Horellou, for giving me the opportunity to conduct the research presented in this thesis and for guiding me with encouragement throughout every stage of the journey. I also sincerely thank my co-supervisor, Magnus Thomasson, and my examiner, John Conway, for their valuable insights, support, and readiness to engage in research discussions.

I am grateful to the Onsala Space Observatory Division for their financial support during my PhD studies.

A special thank you to my manager, Matthias Maerker, and the director of PhD Studies, Vincent Desmaris, for their care and attention to my well-being and mental health.

To the students, postdocs, faculty and administration at AoP and OSO, I appreciate the wonderful work environment you have fostered. I am especially thankful to Santiago del Palacio and Simon Casey for their guidance, help and patience.

I warmly thank Paulina, Pia, and Jasmine for easing the administrative side of things and for brightening my workdays at the university with their kindness and positivity.

My heartfelt thanks go to Prof. Devoto, Matteo, Federica, Francesca, and Valentina for encouraging me to pursue my dreams in Astronomy.

Grazie infinite a Carmen and David, Michela, Silvia, Alisa and Simone, Teresa, Deepika, and Kyoko for being my family in Sweden. Your unwavering support and the countless memories we have shared have made these years unforgettable, and I am endlessly grateful for having you all by my side.

To all my friends, near and far, though not all are named here, I deeply appreciate your presence and constant support throughout this journey.

Infine, la mia più profonda gratitudine va alla mia meravigliosa famiglia e a Gustavo, che hanno sempre sostenuto le mie scelte e ricordato ciò che conta davvero. Il vostro amore, incoraggiamento e affetto sono stati la mia ancora.

Acronyms

AGN	Active Galactic Nuclei
Apertif	APERture Tile in Focus
ASKAP	Australian Square Kilometre Array Pathfinder
ATCA	Australia Telescope Compact Array
ATLAS	Australia Telescope Large Area Survey
BLR	Broad-Line Region
CDF	Chandra Deep Field
CDF-S	Chandra Deep Field-South
DRAO	Dominion Radio Astrophysical Observatory
ELAIS-N1	European Large Area Infrared Space Observatory Survey-North 1
ELAIS-S1	European Large Area Infrared Space Observatory Survey-South 1
FIRST	Faint Images of the Radio Sky at Twenty-Centimeters
FR	Fanaroff–Riley
GMRT	Giant Metrewave Radio Telescope
GOODS-N	Great Observatories Origins Deep Survey-North
GRM	Galactic Rotation Measure
HBA/LBA	High Band Antenna/Low Band Antenna
IGM	Intergalactic Medium
LOFAR	LOw Frequency ARray
LOFAR-ERIC	LOFAR European Research Infrastructure Consortium

LoLSS	LOFAR LBA Sky Survey
LoTSS	LOFAR Two-Metre Sky Survey
LSS	Large Scale Structure
MeerKAT	Name given to the successor of the KAT (Karoo Array Telescope)
MKSP	LOFAR Magnetism Key Science Project
MWA	Murchison Widefield Array
NLR	Narrow-Line Region
NRAO	National Radio Astronomy Observatory
NVSS	NRAO VLA Sky Survey
POGS	POlarised GaLactic and Extragalactic All-Sky Murchison Widefield Array Survey
POSSUM	Polarisation Sky Survey of the Universe's Magnetism
RM	Rotation Measure
RMTF	Rotation Measure Transfer Function
RMSF	Rotation Measure Spread Function
RRM	Residual Rotation Measure
SMBH	Supermassive Black Hole
SPICE-RACS	Spectral and Polarisation in Cutouts of Extragalactic sources from the Rapid ASKAP Continuum Survey
SKA	Square Kilometre Array
KSP	LOFAR Key Science Project
TEC	Total Electron Content

VLA	Very Large Array
VLASS	Very Large Array Sky Survey
WENSS	WEsterbork Northern Sky Survey
WSRT	Westerbork Synthesis Radio Telescope

Contents

Abstract **i**

List of publications **iii**

Acknowledgments **v**

Acronyms **vi**

I Scientific context **1**

1 Introduction **1**
1.1 Extragalactic radio sources 2
1.2 The large-scale magneto-ionic medium 8
1.3 Motivation of this thesis 10

2 Polarization and Faraday rotation **15**
2.1 Synchrotron radiation 16
2.2 Polarization and Stokes parameters 17
2.3 Faraday rotation 20
2.4 Depolarization 24
2.5 The Faraday Rotation Measure Synthesis Technique 29

2.6 *qu*-fitting . . . 34
2.7 Rotation Measure Grid . . . 36

3 Polarized source counts **41**
3.1 Definition . . . 43
3.2 Measurements in total flux density and polarized flux density . 46
3.3 Modeling source counts in polarization . . . 48

4 Polarization with LOFAR **53**
4.1 LOFAR . . . 53
4.2 Constraining cosmic magnetic fields with LOFAR . . . 56

5 Polarization in the ELAIS-N1 LOFAR Deep Field **63**
5.1 The European Large-Area ISO Survey-North 1 (ELAIS-N1) . . 63
5.2 The ELAIS-N1 LOFAR Deep Field . . . 64
5.3 Observations . . . 65
5.4 Stacking polarization data . . . 66
Noise . . . 66
The stacking method . . . 70
Managing big data . . . 75
Improving the stacking technique . . . 76
5.5 Polarized source counts . . . 78
Comparisons with previous work at 1.4 GHz . . . 82
5.6 Rotation Measure and Residual Rotation Measure grids 86
5.7 LOFAR ELAIS-N1 Deep Field and Sky Survey comparison . . 87

6 Depolarization study of the reference source **89**
6.1 The data . . . 90
Uncertainties . . . 92
Faraday spectrum of source 07 in Cycle 2 . . . 92
6.2 The method . . . 93
The models . . . 93
Priors . . . 94
qu-fitting . . . 95
6.3 Results . . . 96
Discussion . . . 101

7 Summary of included papers **105**
7.1 Paper I 105
7.2 Paper II 107

8 Summary and possible future work **109**

Bibliography **111**

A Appendix **123**
A.1 Complex fractional polarization from two RM components interfering inside the beam. 123

II Papers **127**

A LOFAR Deep Fields: Probing the sub-mJy regime of polarized extragalactic sources in ELAIS-N1. I. The catalog **A1**

B LOFAR Deep Fields: Probing the sub-mJy regime of polarized extragalactic sources in ELAIS-N1. II. Analysis **B1**

Part I

Scientific context

CHAPTER 1

Introduction

Magnetic fields permeate the Universe across all scales and cosmic epochs. These fields intertwine with cosmic web filaments, influencing the Large Scale Structure of our Universe. Despite their ubiquity and important role in astrophysical processes, our knowledge and understanding of large-scale magnetic fields properties and origins is still limited.

The proposed theories for explaining the origin of cosmic magnetic fields can be divided into two main ideas: (1) the primordial scenario, where seed magnetic fields were produced in the early Universe, before the structure formation; (2) the astrophysical scenario, where astrophysical sources generated weak seed magnetic fields, that were amplified and then diffused into the surrounding medium. Regardless of the mechanism giving rise to the magnetic field seed, it is theorized that the fields underwent amplification via the structure formation processes, up to the values we currently observe (e.g. Durrer & Neronov 2013, and references therein). Constraining these hypotheses with observations presents difficulties. Traditionally, studies of cosmic magnetic fields focused on galaxy clusters, where structure formation altered the field seed, impacting its geometry and intensity (e.g. Feretti et al. 2012, and refer-

ences therein). Therefore, exploring cosmic filaments and voids is crucial, as they experience fewer structure formations, thereby allowing for insights into the magnetic field seed using modern radio interferometers.

A powerful way to probe cosmic magnetism is through observations of the linearly polarized radio emission from Active Galactic Nuclei (AGN) that arises from synchrotron processes. This radiation interacts with the cosmic magnetic fields it traverses, resulting in observable effects that reveal the presence and characteristics of these fields. However, there are significant challenges. One primary challenge lies in the low number density of polarized background sources at low radio frequencies (< 200 MHz), a favored frequency range for these studies. For this reason, it is essential to find new techniques to increase the number of detectable polarized background sources and to characterize them.

In this Chapter, I present a concise overview of the properties of the AGN employed as extragalactic background radio sources for probing the magneto-ionic medium along their lines of sight (Sect. 1.1). Next, I provide a short summary of the properties of magnetized media that the polarized radiation from AGN may traverse along its path (Sect. 1.2). Finally, I provide an overview of the scientific community's broader efforts to use observational data to explore extragalactic magnetic fields, outline the specific aims of this thesis, and describe how it contributes to and aligns with this research framework (Sect. 1.3).

1.1 Extragalactic radio sources

Radio galaxies which exhibit polarization at low radio frequencies are used to probe the extragalactic magnetized medium along their lines of sight. These sources are classified as AGN. Some of these AGN are powerful sources of energy in the Universe, with emission across the entire electromagnetic spectrum, from the radio band up to γ-rays. The unified model for AGNs states that they all share the same basic structure:

- a supermassive black hole (SMBH) in the center of the galaxy;
- an accretion disk that surrounds the central black hole and can emit X-rays and in the optical to UV spectrum;

- regions of emission lines: a broad-line region (BLR) and a narrow-line region (NLR);

- a toroidal dusty obscuring structure, rich in molecular gas and dust;

- occasionally, twin, highly collimated relativistic plasma jets, that originate in the vicinity of the SMBH, perpendicular to the accretion disk and visible in the radio band; sometimes, only one jet is observed, and in most sources where two jets are found one of them, the "counter-jet", is significantly weaker than the other.

The distinction between different types of AGN (quasars, blazars, radio galaxies...) depends on the viewing angle. Fig. 1.1 and Fig.1.2 show schematic representations of an AGN.

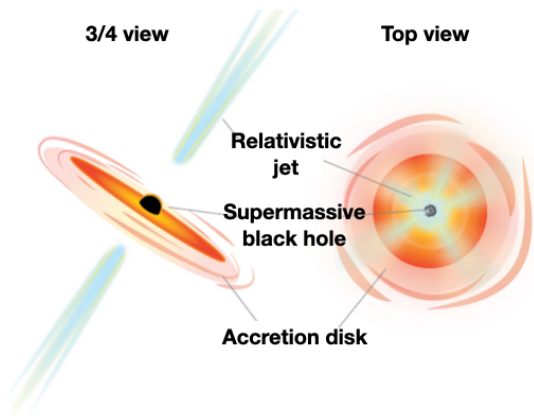

Figure 1.1: Representation of an AGN viewed from two different directions. The classification is based on the orientation with respect to the observer's line of sight. Credit: Sophia Dagnello, NRAO/AUI/NSF.

In the next sections I summarize the properties of quasars, blazars and radio galaxies following the description in the textbook *Galactic and Intergalactic Magnetic Fields* by Klein & Fletcher (2015).

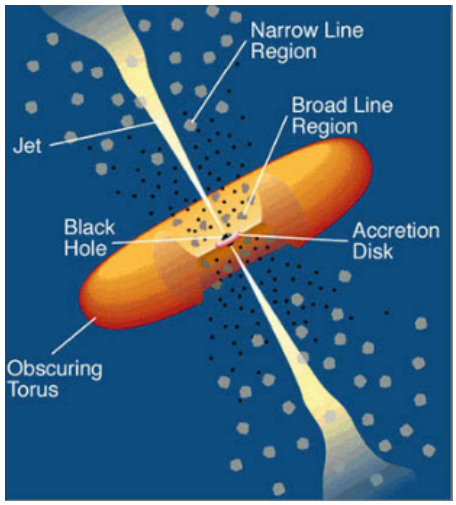

Figure 1.2: Schematic model of an AGN. From Urry & Padovani (1995).

Radio galaxies

Radio galaxies are almost always associated with optical elliptical galaxies. The radio emission is fueled by a pair of plasma jets that are initially relativistic and propagate in opposite directions outside the host galaxy. In many cases, the plasma slows down into ellipsoidal radio lobes that surround the radio jets. The morphology of the lobes depends on the interaction between them and the medium into which they are expanding. Fig. 1.3 shows *Cygnus A*, the first radio galaxy discovered and identified as such, and where the main features are indicated.

Radio galaxies, with integrated radio luminosities $L_{radio} \geq 3{\times}10^{41}$ erg s^{-1}, are very strong radio emitters. The observed synchrotron emission arises from relativistic particles with energies of ∼GeV gyrating in a magnetic field of the order of 10 μG.

Radio galaxies show a large variety of sizes, from the most compact (few pc) to the most extended structures covering hundreds of kiloparsecs and extending up to megaparsec scales. Traditionally, they are classified as "Faranoff-Riley" (FR) type I and type II (Fanaroff & Riley, 1974):

- FR II radio galaxies are powerful edge-brightened radio sources, due to

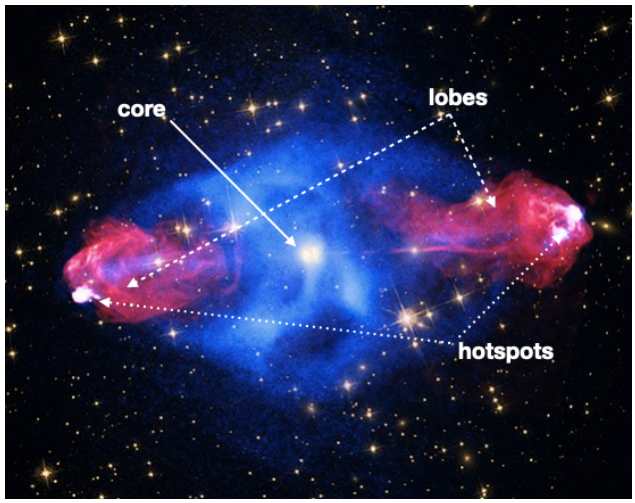

Figure 1.3: X-ray (in blue), optical (in yellow) and radio (in red) images of Cygnus A. Credits: X-ray: NASA/CXC/SAO; Optical: NASA/STScI; Radio: NSF/NRAO/AUI/VLA.

the presence of compact hot-spots (sometimes <1 kpc). The lobes are well separated, longer than wide. Sometimes they show weak and well collimated jets and in about 10% of the sources only one jet is seen. These sources are usually associated with quasars and/or distant galaxies. Most FR II radio galaxies have monochromatic radio luminosities above 10^{32} erg $s^{-1}Hz^{-1}$ at 1.4 GHz.

- FR I radio galaxies are weaker radio sources. The hot-spots are weak or absent and the lobes are not always so well aligned with the central object. Sometimes they also show pronounced distortions in their structure. At low resolution they appear with a higher brightness in the central part, which slowly decreases away from the core. This is why they are called edge-darkened. They are generally associated with nearby galaxies and/or galaxies in galaxy clusters. FR I radio galaxies typically have monochromatic radio luminosities below 10^{32} erg $s^{-1}Hz^{-1}$ at 1.4 GHz.

At low radio frequencies, detection of polarized emission generally coincides with the position of hotspots in FR II radio galaxies, while in FR I polariza-

tion usually comes from the central regions (Paper II). The detection rate of polarized FR II radio sources is generally greater than for of FR I (Van Eck et al., 2018), however Herrera Ruiz et al. (2021) suggested that the number of the latter was likely to increase in increasingly sensitive observations. Fig. 1.4 shows two examples of sources with morphologies of FR I and FR II radio galaxies, detected in the ELAIS-N1 LOFAR Deep Field (Sabater et al., 2021). On the left panel we can see that the core of the radio galaxy is brighter than the jets, while on the right panel the core is not visible but the hotspots and some diffuse emission in the lobes are clearly visible. Regarding polarization, in my work on ELAIS-N1 I detected polarized emission from the cores of FR I radio galaxies, and from one or both the hotspots of FR IIs.

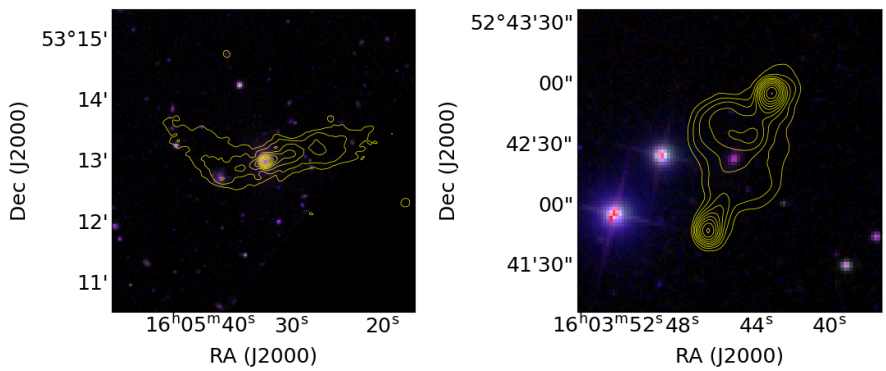

Figure 1.4: Example of sources with morphology of an FR I (left panel) and an FR II (right panel) radio galaxy. The images are from the Sloan Digital Sky Survey (SDSS) and the yellow contours show the 150 MHz LOFAR observations radio emission morphology from the image of Sabater et al. (2021) at 6″-resolution. I detected polarization from both of these sources.

Radio quasars

Historically, quasars were identified as optically star-like (quasi-stellar) objects (QSO) associated with strong radio sources and having optical emission-line spectra. Quasars are visible from radio wavelengths through X-ray energies, are the most luminous class of AGNs and the most luminous objects in the Universe, reaching luminosities from 10^{45} to 10^{49} erg s^{-1}. The most accredited

hypothesis foresees that they are connected to a period of violent merging of massive galaxies in the course of structure formation of the Universe, peaking in redshift range between $z \approx 2$ and $z \approx 0.4$. Not all quasars are strong radio emitting sources, and with respect to this characteristic, they are divided into *radio-quiet*, that comprise the majority of quasars, and *radio-loud*. Radio-loud quasars show radio jets, which sometimes produce large-scale lobes. Fig. 1.5 shows an example of a quasar detected in the ELAIS-N1 LOFAR Deep Field (Sabater et al., 2021), which I found to be polarized.

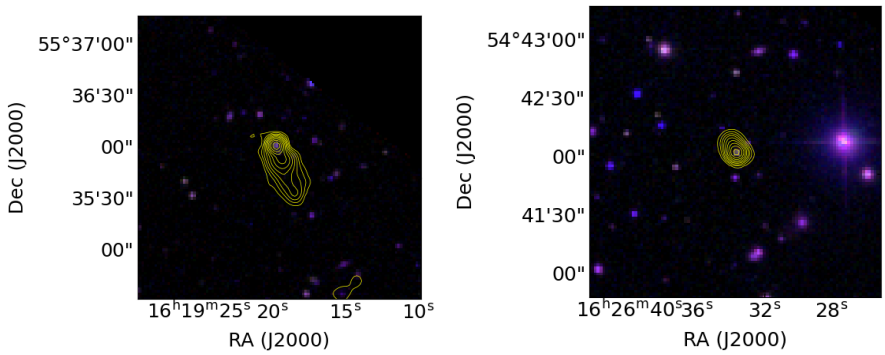

Figure 1.5: Example of a blazar (left panel) and a quasar (right panel). The images are from the Sloan Digital Sky Survey (SDSS) and the yellow contours show the 150 MHz LOFAR observations radio emission morphology from the image of Sabater et al. (2021) at 6″-resolution. I detected polarization from both of these sources.

Blazars

Blazars exhibit strong variability and are most likely AGN in which we are looking almost directly into the jet coming towards us, which results in strong relativistic boosting, in so-called relativistic Doppler boosting. At radio frequencies, they show generally high and variable polarization (e.g. Fan et al. 2008; O'Sullivan et al. 2023). In the right panel of Fig. 1.5 I show an example of a blazar in the ELAIS-N1 LOFAR Deep Field, from which I detected polarized emission.

1.2 The large-scale magneto-ionic medium

The polarized emission from background radio sources interacts via Faraday rotation with all the magneto-ionic structures along the line of sight, leaving traces in the signal we measure (see Chap. 2). It is therefore crucial to identify and characterize these background sources and the magneto-ionic structures along the different lines of sight to the polarized radio sources.

The magneto-ionic structure closest to us, particularly relevant at low radio frequencies, is the Galactic foreground. Beyond our Galaxy, we encounter magnetic fields of the cosmic web, including clusters and superclusters of galaxies, filaments, and voids, which together represent the large-scale structure of the Universe.

Magnetic fields in the Milky Way: the Galactic foreground

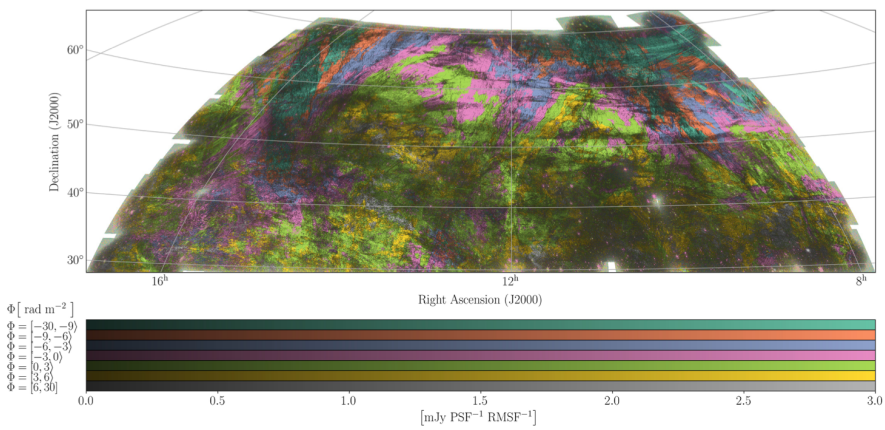

Figure 1.6: Image of polarized radio emission from our Galaxy detected with LOFAR at 150 MHz and 4.3′-resolution. Different colors show emission detected at different Faraday depths. From Erceg et al. (2022).

At low radio frequencies (< 5 GHz), the dominant emission mechanism of the magneto-ionic medium of the Galaxy is the diffuse synchrotron radiation from relativistic electrons that interact with the Galactic magnetic field. The analysis of the linearly polarized synchrotron signal from a large area observed

at low angular resolution provides information on the Galactic medium, revealing intricate polarized Galactic structures (e.g. Thomson et al. 2021; Erceg et al. 2022).

At higher resolution, the Galactic polarized emission is not detected in emission. However, the polarized emission detected from discrete background extragalactic sources (see Sect. 1.1) still interacts with the Galactic magneto-ionic medium, which affects the polarized signals that we measure toward these sources.

The density of free electrons and the magnetic field strength of the Galaxy decrease with distance from the Galactic plane, such that the higher absolute values of Galactic latitudes are preferable to minimize contamination from this foreground and study the extragalactic medium.

Fig. 1.6 shows the polarized emission from our Galaxy at 150 MHz and arcminutes resolution. The different colors represent the *Faraday depth*, a quantity that I will introduce in Chap. 2, that is proportional to the electron density and the magnetic field component parallel to the line of sight.

Magnetic fields in the cosmic web

The large-scale distribution of galaxies in the Universe is very complex and gaalxies are not uniformly scattered: there are clusters of galaxies and expansive interconnected filamentary structures of superclusters, with immense voids in between. While magnetic fields in galaxies and galaxy clusters are well studied at low radio frequencies (e.g. Vacca et al. 2022; Heesen et al. 2023), detecting magnetic fields in the cosmic filaments is particularly challenging because they are faint.

A recent study at 1.4 and 30 GHz has led to the detection of magnetic fields of 30–60 nG in the weaker filaments of the cosmic web (Vernstrom et al., 2021) through stacking of synchrotron emission.

Using a complementary method, through the use of the Rotation Measure properties of polarized radiation from background sources at 150 MHz, the strength of magnetic fields in filaments was estimated to be $\simeq$ 30 nG (Carretti et al., 2022), in agreement with what was found at higher frequency by Vernstrom et al. (2021).

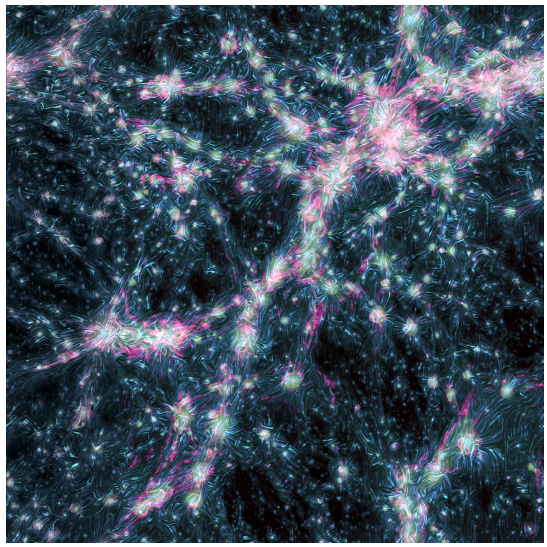

Figure 1.7: Simulation of the cosmic web, with filaments around clusters emitting radio emission, in pink. The magnetic fields are shown in cyan. Credit: F. Vazza, D. Wittor and J. West.

1.3 Motivation of this thesis

As we reviewed in the previous sections, detecting and characterizing extragalactic magnetic fields is challenging due to their weakness. One of the most powerful tools to probe these weak fields is through the measurement of Faraday Rotation Measures (RM) of polarized radio sources.

Faraday Rotation occurs when polarized radio waves travel through a magnetized plasma, causing the polarization angle to rotate. The amount of rotation is proportional to both the strength of the magnetic field along the line of sight and the electron density of all the magneto-ionic foregrounds in front of the polarized source. By measuring the Faraday rotation measure (RM) of the polarization angle of extragalactic radio sources, we can infer the magnetic field properties of the intervening media between the source and the observer. Observations of distant extragalactic polarized radio sources across the sky are used to create a RM grid, that combined with applying statistical techniques, allows us to address several key scientific challenges.

These include understanding how magnetic fields are generated and sustained in the Milky Way and other nearby galaxies, as well as their role in galaxy formation and evolution. RM grids help us study magnetic fields in various astrophysical environments such as HII regions, supernova remnants, planetary nebulae, and high-velocity clouds within the Milky Way. Further, the RMs grid allow to investigate the scales and strengths at which magnetic fields are generated in galaxy clusters, and how these properties correlate with the clusters' dynamical states. They will also help uncover the large-scale structure of the magnetized Universe, offering the potential to statistically detect magnetic fields in the cosmic web and their evolution in intervening galaxies and clusters over cosmic time (e.g. Johnston-Hollitt et al. 2015; Heald et al. 2020).

At high radio frequencies ($\sim$1–2 GHz), the NRAO VLA Sky Survey (NVSS; Condon et al. 1998; Taylor et al. 2009) was the first all-sky RM grid and remains a foundational dataset for studying the magnetic field of the Milky Way as well as large-scale structures beyond our Galaxy. Data from the latest and densest such RM grid by Hutschenreuter et al. (2022) is shown in Fig. 1.8.

Following this, numerous studies at various resolutions and frequencies have been conducted, each contributing to our understanding of cosmic magnetic fields. The diversity in resolution is crucial because it allows us to disentangle the contributions of the Galactic magneto-ionic medium from the extragalactic one. Indeed, high-resolution ($< 1'$) observations primarily detect extragalactic polarized emission, as they resolve out the diffuse Galactic synchrotron emission (e.g. Herrera Ruiz et al. 2021; Erceg et al. 2022, as illustrated in Fig. 1.6). Even at high spatial resolutions, the dominant foreground effect on the RM of each extragalactic source remains the Galactic medium, at least at low and intermediate Galactic latitudes. The presence of these Galactic RM effects however does not diminish the potential of RM grids for studying extragalactic magnetic fields. The key lies in leveraging statistical techniques and large RM datasets. The collection of dense RM measurements across a wide range of frequencies and angular resolutions allows researchers to model and remove the Galactic foreground effectively (e.g. Hutschenreuter et al. 2022), which is essential to study the extragalactic RM contribution. Despite the residual Galactic effects, variations in RM values can still reveal critical insights about the magnetic fields beyond our Galaxy.

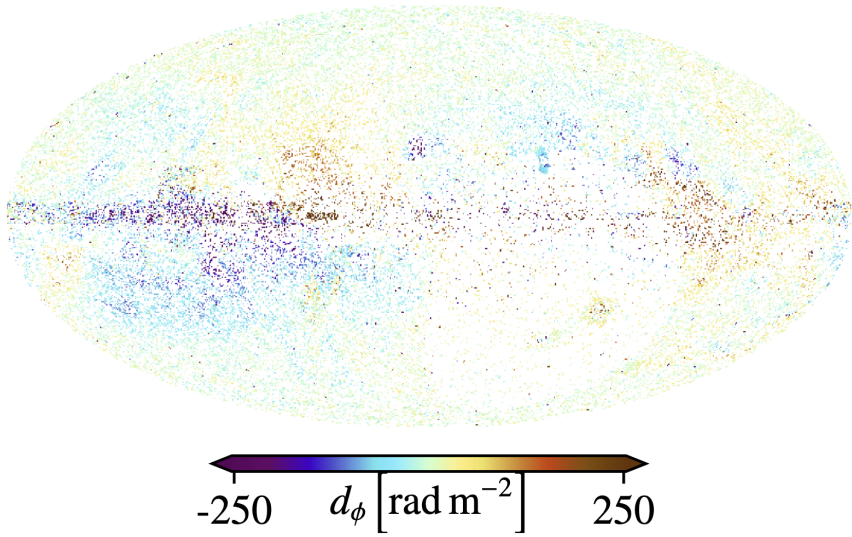

Figure 1.8: The RM grid data used by Hutschenreuter et al. (2022) shown on a sky projection in Galactic coordinates. The dataset consists of 55 190 RM values from 41 available surveys. This dataset was used to reconstruct the Galactic Faraday map. d_ϕ represents the RM values.

The RM grid will be significantly enhanced by future radio telescopes like the Square Kilometre Array (SKA), which will be capable of detecting millions of polarized sources with unprecedented sky coverage, sensitivity, and resolution. With such a dense RM grid, we will be able to statistically study variations in RM across a wide range of foreground cosmic structures, potentially revealing the magnetic field strengths and configurations in galaxies, galaxy clusters, and in the intergalactic medium (e.g. Johnston-Hollitt et al. 2015; Heald et al. 2020). For example, correlations between RM variations and foreground galaxy clusters could provide direct evidence of magnetized plasma in the intracluster medium, while correlations between RM and the redshift of background sources may offer the first clear detection of the intergalactic magnetic field threading the cosmic web.

Collecting RM values at different radio frequencies, complemented with the characterization of the polarized background source, helps us understand

which magneto-ionic medium is the source of the extragalactic RM. In this framework, the LOw Frequency ARray (LOFAR) plays a crucial role because of the sensitivity, angular resolution and precision on the inferred RM values that can be achieved through low-frequency broad-band polarimetry, allowing us to study the polarized radio emission at around 150 MHz in unprecedented detail. In the frequency range of 120 to 168 MHz, at a resolution of 20″ and observing time of 8 hours per pointing, the LOFAR Two-Metre Sky Survey (LoTSS) collected RM values in two large angular area northern fields (O'Sullivan et al., 2023). The comparison of these data with the data from NVSS allowed to discern the contribution on the RM from the local environment of the source from the contribution due to the cosmic web filament, and probe the strength and evolution of magnetic fields in such filaments(Carretti et al., 2022, 2023).

An issue however is that at low frequencies the current RM grids are less dense than at higher frequencies. ($\sim$1 source per square degree in the NVSS RM catalog and $\sim$0.4 source per square degree in the LoTSS-DR2 RM catalog), due to the fact that the polarized signal at low radio frequency is more affected by depolarization, which affects the detection rate of polarized sources and thus the number of RM available for the statistical analysis.

The work presented in this thesis contributes to the effort to construct denser RM grids at low frequencies. By combining polarimetric observations at 115–177 MHz from the LOFAR European Large Area ISO Survey-North 1 (ELAIS-N1) deep field, with a total integration time of 152 hours and a resolution of 6″ over a 25 deg^2 area, this study represents the deepest and highest-resolution polarization survey at 150 MHz made to date. With a density of 1.3 polarized components per square degree (almost three times that of LoTSS-DR2 RM) this work makes a significant step in uncovering the properties of faint polarized sources at low frequencies, which are mostly unknown.

While the detection of faint polarized sources and the determination of their RM in this thesis is an important achievement, its broader impact lies in shaping future RM studies that aim to measure millions of sources. It is hoped that the work presented in this thesis will help refine the planning of upcoming SKA and LOFAR2.0 surveys, enabling us to map the magnetic Universe with unprecedented detail and precision.

In the following chapters, I give the framework to understand the findings of

my research papers, showing how this work contributes to our understanding of cosmic magnetism and prepares the ground for next-generation polarization surveys. In Chap. 2 I introduce the techniques and principles used to probe cosmic magnetic fields through the analysis of Faraday rotation in polarized observations, while in Chap. 3 I explain the theory of the source counts and their importance in understanding the properties and evolution of polarized radio sources. In Chap. 4, I discuss the unique capabilities of LOFAR in probing cosmic magnetic fields. In Chap. 5 I introduce the ELAIS-N1 LOFAR deep field observations and provide more context and details to understand the work I carried out in Paper I and Paper II. Finally, in Chap. 6 I present some new, not yet published research work where I analyze the depolarization properties of a bright source detected in the ELAIS-N1 deep field analysis.

CHAPTER 2

Polarization and Faraday rotation

The observed radio signal that originates from synchrotron emission is linearly polarized. The interaction between such linearly polarized radiation and foreground magnetized plasma leads to Faraday rotation of the polarization angle of the emission, which therefore encodes information about the magneto-ionic medium between the emitting radio source and the observer.

In this Chapter, I introduce the concepts and the techniques that allow us to constrain cosmic magnetic fields through the study of the Faraday rotation of the observed polarized signal. To facilitate this exploration, I present a comprehensive review of polarization theory in radio astronomy. In Sect. 2.1 I give a brief summary of the fundamental aspects of synchrotron processes that arise in radio sources, underlying the mechanisms governing the production of linearly polarized emission. I introduce in Sect. 2.2 the Stokes parameters, used to describe the observed total and polarized radio emission. The Faraday rotation effect and depolarization mechanisms are introduced, respectively, in Sect. 2.3 and Sect. 2.4. In Sect. 2.5 and in Sect. 2.6 I review the techniques used to capture and study Faraday rotation signatures. Finally, I introduce in Sect. 2.7 the *Rotation Measure (RM) Grid*, a crucial resource for probing the cosmic magnetism.

2.1 Synchrotron radiation

The theory associated with the synchrotron emission mechanism is well explained and developed in the literature; for a more detailed description see *Radiative processes in astrophysics* by Rybicki & Lightman (1979) and *Galactic and Intergalactic Magnetic Fields* by Klein & Fletcher (2015).

Relativistic charged particles moving in a magnetic field are forced to undergo a helical motion, i.e. a combination of a circular motion in the plane perpendicular to the magnetic field lines and a linearly uniform motion in the direction of the magnetic field. Radiative losses are caused by the acceleration of these particles. The study of such radiation is possible by formulating some hypotheses on the physical conditions of the emitting plasma, in particular on the energy density of the particles and the magnetic field present, since the observation of the radiation alone provides information on the global interaction but not on the individual components that produce the emission. From observation of cosmic rays on Earth we expect that the energy spectrum $N(E)dE$ in the Milky Way is described by a power law:

$$N(E)dE \propto \; E^{-g}dE\,, \tag{2.1}$$

with $g \approx 2.4$. The specific intensity I_ν associated at the energy distribution is:

$$I_\nu \propto B_\perp^{1-\alpha}\,\nu^\alpha\,, \tag{2.2}$$

where $B_\perp$ is the magnetic field component perpendicular to the line of sight and α is the spectral index, which is related to the exponent, g, of the power law spectrum of the cosmic-ray electrons:

$$\alpha = \frac{1-g}{2}\,, \tag{2.3}$$

giving in the Milky Way $\alpha \approx -0.7$.

Synchrotron radiation produced by a single charge, due to the relativistic beaming effect, appears to be half concentrated in a cone with a half-width of about γ^{-1}, where γ is the Lorentz factor defined as $\gamma = \left(1 - v^2/c^2\right)^{-\frac{1}{2}}$, v is the speed of the particle and c is the speed of the light. Such a cone has an axis along the instantaneous direction of the velocity v of the emitting particle, while the other half of the radiation is essentially diluted over the entire solid

angle. It follows that, for a single electron moving around the lines of force of the magnetic field, the observer receives the radiation only when the velocity vector of the electron intercepts the line of sight. Synchrotron radiation is linearly polarized: since the direction of motion corresponds to the direction of emission, the radiation must be linearly polarized if we observe exactly along the plane of the orbit of the charged particle when the electron moves towards us. Elliptically polarized radiation, with lower intensity, occurs when the line of sight is slightly out of the plane but always within the γ^{-1} half-amplitude cone of radiation. The direction of the electric vector in case of linear polarization, or of the major axis of the ellipse in the case of elliptical polarization, is in the plane of the orbit of the charged particle and is therefore perpendicular to the direction of the magnetic field present. We receive radiation from a plasma of relativistic electrons only from those whose velocities form an angle $\leq \gamma^{-1}$ with the line of sight and if the magnetic field is ordered the radiation is still polarized. Since the velocities with which the electrons are introduced into the field are generally disordered, and therefore all different from each other, the planes of the orbits "useful" for receiving radiation will all be slightly different. The polarization ellipses will be equally right-hand and left-hand polarized, so the contributions of circular polarization will tend to cancel out on average. Therefore it will remain a state of linear polarization, with the electric vector perpendicular to the magnetic field.

2.2 Polarization and Stokes parameters

In most real cases, the magnetic field is not uniform and the polarization percentage of the radiation can be greatly reduced: regions with differently oriented magnetic fields give rise to differently oriented polarization orientations; these, averaging along the line of sight and in the beam of the observation instrument, tend to cancel out. The measurement of the polarization percentage therefore allows to estimate the degree of order of the magnetic field in the radio source or in the medium through which the radiation is propagating.

The radio emission can be empirically quantified using the Stokes parameters; for a more detailed discussion see *Tools of Radio Astronomy* by Wilson et al. (2013), *Essential Radio Astronomy* by Condon & Ransom (2016) and Robishaw & Heiles (2021).

Let us consider a monochromatic wave travelling along the $\hat{z}$ direction. The

polarization of the wave is defined by the motion of its electric field vector $\vec{E}$ as a function of time within a plane perpendicular to the direction of propagation. In the most general case, the locus traced out by $\vec{E}$ is an ellipse, as shown in Fig. 2.1. Quantifying this polarization ellipse is possible in terms of any orthonormal basis within the plane of polarization.

The orthogonal components of the polarization ellipse in linear basis at $z = 0$ are:

$$E_x(t) = E_{0,x} e^{i(2\omega t + \phi_x)},\ E_y(t) = E_{0,y} e^{i(2\omega t + \phi_y)}\,, \tag{2.4}$$

and in circular basis:

$$E_R(t) = E_{0,R} e^{i(2\omega t + \phi_R)},\ E_L(t) = E_{0,L} e^{i(2\omega t + \phi_L)}\,, \tag{2.5}$$

where t represents the time, $E_{0,x}$ and $E_{0,y}$ are the projections of $\vec{E}$ in the (x, y) plane, $\omega = 2\pi\nu$ is the angular frequency and ϕ_x and ϕ_y are constant phases, ans similar for the $E_R(t)$ and $E_R(L)$ components..

The orientation of the major axis of the polarization ellipse respect to the x axis is given by the angle χ:

$$\tan 2\chi = \frac{2E_{0,x}E_{0,y}\cos(\phi_y - \phi_x)}{E_{0,x}^2 - E_{0,y}^2} = \tan(\phi_R - \phi_L)\,. \tag{2.6}$$

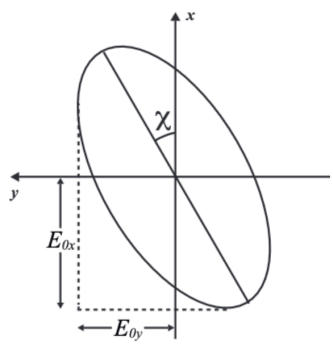

Figure 2.1: Example of ellipse drawn by the electric field vector $\vec{E}$ in Eq. 2.5 in the (x, y) plane and propagating in the z-direction. From Robishaw & Heiles (2021).

In astronomy we measure the power of a radiation, i.e. the time average of the square of the electric field or the time average of the product of the electric field with its complex conjugate. In particular, this is expressed through the *Stokes parameters*.

The Stokes parameters are linear combinations of power measurements in independent orthogonal polarizations and are denoted as *I, Q, U* and *V*; they can describe a completely polarized light, but also unpolarized light and partially polarized light. They are defined as:

- $I = \langle E_{0,x}^2 \rangle + \langle E_{0,y}^2 \rangle = \langle E_{0,R}^2 \rangle + \langle E_{0,L}^2 \rangle$,
- $Q = \langle E_{0,x}^2 \rangle - \langle E_{0,y}^2 \rangle = 2\langle E_{0,R} E_{0,L} \rangle \cos(\phi_R - \phi_L)$,
- $U = 2\langle E_{0,x} E_{0,y} \rangle \cos(\phi_y - \phi_x) = 2\langle E_{0,R} E_{0,L} \rangle \sin(\phi_R - \phi_L)$,
- $V = -2\langle E_{0,x} E_{0,y} \rangle \sin(\phi_y - \phi_x) = \langle E_{0,R}^2 \rangle - \langle E_{0,L}^2 \rangle$,

where the brackets $\langle\,\rangle$ denote a time average.

The Stokes parameter I quantifies the total intensity of the field; Q describes the preponderance of linearly horizontally polarized radiation over linearly vertically polarized radiation; U describes the preponderance of linear $+45^{\circ}$ polarized radiation over linear -45° polarized radiation; V quantifies the preponderance of right circularly polarized radiation over left circularly polarized radiation.

Comparing Eq.2.6 and the definition of the Stokes parameters, the polarization angle is defined as:

$$\chi = \frac{1}{2} \tan^{-1} \left(\frac{U}{Q} \right) . \tag{2.7}$$

The fractional linear polarization, or degree of linear polarization, is defined as the ratio of the intensity of the linearly polarized emission to the total intensity:

$$\mathrm{p} = \frac{\sqrt{Q^2 + U^2}}{I} ; \qquad 0 \leq \mathrm{p} \leq 1 . \tag{2.8}$$

As synchrotron radiation is linearly polarized, we can assume $V = 0$. The linearly polarized intensity can be written as a complex number:

$$P = Q + iU = \mathrm{p} I e^{2i\chi} . \tag{2.9}$$

The polarized signal is a fraction of the total signal. Considering an isotropic distribution of the speeds and uniform magnetic field, it is calculated that the intrinsic linear polarization fraction is $\mathrm{p} = (g+1)/(g+7/3)$; in the case of the Milky Way (with $g \approx 2.4$; Eq. 2.1) we can expect a maximum degree of linear polarization for a synchrotron source of $\mathrm{p} \approx 72\%$. We can see that 100% of linearly polarized signal is never reached; actually most sources show considerably lower polarization at radio frequencies. Indeed if the magnetic field is not spatially uniform, as happens in real astronomical cases, the polarization percentage can be greatly reduced, since the contributions originating in regions where the magnetic field has different orientations have, in turn, polarizations differently oriented; those, averaging along the line of sight, or within the solid angle defined by the resolving power of the observation instrument, tend to cancel out.

2.3 Faraday rotation

Linearly polarized electromagnetic radiation, propagating in a magneto-ionic medium, undergoes a rotation of its polarization plane. This effect is called Faraday rotation. A detailed derivation of Faraday rotation can be found in plasma physics textbooks, as Choudhuri (1998) and Gurnett & Bhattacharjee (2005), and in the paper of Ferrière et al. (2021).

Let us consider a linearly polarized wave that propagates in a magnetized plasma, with electron density n_e and magnetic field $\vec{B}$. The solution of the wave propagation consists in a superposition of a right-hand (RCP) and left-hand (LCP) circularly polarized waves. The phase velocity of the RCP wave is slightly higher than the other, so that a phase difference $\Delta\phi = \phi_R - \phi_L$ arises and increases between the RCP and LCP waves as they propagate in the medium. This causes the linearly polarized wave to change its polarization angle χ during the propagation, such that $\Delta\chi = \frac{1}{2}\Delta\phi$. The rotation, i.e. the Faraday rotation, occurs in the right-handed sense about the parallel component along the line of sight of the magnetic field, $B_{\parallel}$, if directed towards the observer. These concepts are illustrated in Fig. 2.2 and Fig. 2.3.

The Faraday rotation of the polarization angle of a linearly polarized wave emitted from a radio source is strongly dependent on the observing wavelength:

$$\chi = \chi_0 + \mathrm{RM}\,\lambda^2\,, \tag{2.10}$$

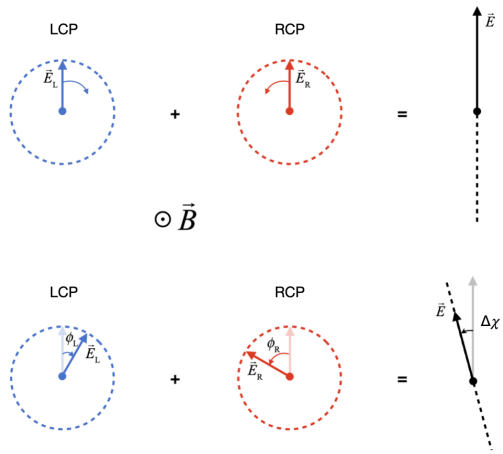

Figure 2.2: Adapted from Ferrière et al. (2021). Cartoon showing the electric field vectors of a linearly polarized radio wave, $\vec{E}$, in black, and of its left and right circularly polarized components, $\vec{E}_L$, in blue, and $\vec{E}_R$, in red, as defined with respect to the magnetic field, $\vec{B}$, and as seen when $\vec{B}$ points toward the reader. Top row: at the source and initial time. Bottom row: at distance from the source and time greater than the phase travel time. The dashed lines show the (linear or circular) figures traced out by the electric field vectors. The curved arrows in the top row indicate the sense of rotation of $\vec{E}_L$ and $\vec{E}_R$. The curved arrows in the bottom row show the angles through which $\vec{E}_L$ and $\vec{E}_R$ have rotated from their common initial direction at the source, which is along the orientation of linear polarization at the source. $\vec{E}_R$ has rotated more than $\vec{E}_L$, i.e. $\phi_R > \phi_L$, so the orientation of linear polarization has rotated in the right-handed sense. Hence, Faraday rotation is right-handed about $\vec{B}$.

where χ and χ_0 are respectively the observed and the intrinsic polarization angles (i.e. the polarization angle at the source), and RM is called *rotation measure*.

Traditionally, RM was obtained by observing χ at different wavelengths, and then determining its slope in the λ^2-space. Following the definition of Faraday rotation given previously, a positive value of RM indicates a magnetic field on average directed towards the observer, and a negative value of RM implies a magnetic field on average directed away the observer. Fig. 2.4 shows the

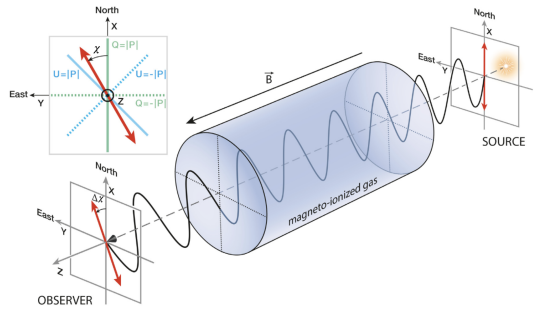

Figure 2.3: Adapted from Ferrière et al. (2021). Representation of the Faraday rotation effect on the polarized emission of a background radio source caused by the magneto-ionized gas. The electric field vector of the linearly polarized radio wave oscillates along the propagation direction, between the source (far side) and the observer (near side), and the polarization orientation (red double-headed arrow) undergoes Faraday rotation as the wave passes through a magneto-ionized region (blue shaded region). Faraday rotation is always right handed about the magnetic field, $\vec{B}$. When $\vec{B}$ points toward (away from) the observer, Faraday rotation is counterclockwise (clockwise) in the plane of the sky; this corresponds to a positive (negative) rotation angle, $\Delta\chi = \chi - \chi_0$ (eq. 2.10), in the IAU definition of the polarization angle (measured counterclockwise from north; see inset in the upper-left corner). The inset also shows the axes of the Stokes parameters Q and U (defined through Eq. 2.8), i.e. the (faded green) lines where $Q = \pm|P|$ (or $U = 0$) and the (faded blue) lines where $U = \pm|P|$ (or $Q = 0$).

polarization angle χ as a function of λ^2 (m^2) for a polarized source found in my work. The effect of Faraday rotation is clearly visible in the variation of χ; the loss of definition of the slope of the angle is due to the lower intensity of the signal, which in turn is due to depolarization and I will discuss in the Sect. 2.4.

In the ideal case of a non-emitting magnetized plasma being the only source for the rotation effect, the RM is equal to the Faraday depth ϕ:

$$\phi(l) = \frac{e^3}{8\pi^2 m_e^2 c^3 \epsilon_0} \int_{\text{source}}^{\text{observer}} B_{\parallel}\, n_e\, dl\,. \tag{2.11}$$

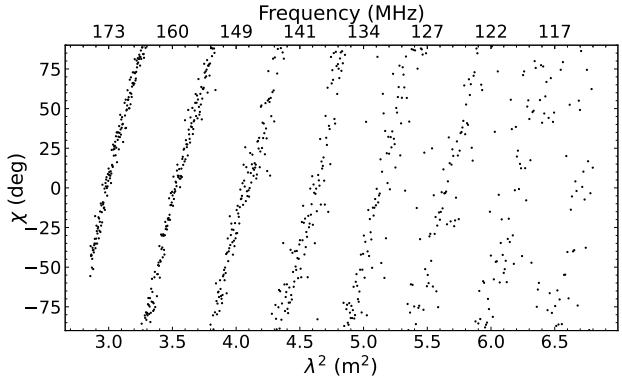

Figure 2.4: Polarization angle χ versus wavelength squared (m^2) for a source found to be polarized in my work (source 07 from Paper I). The rotation of the polarization angle is caused from the Faraday rotation effect, and its slope is the RM (here, RM≈ 6 rad m^{-2}). The loss of definition of the slope of the angle indicates depolarization.

In convenient units,

$$\phi(l) = 0.812 \int_{\text{source}}^{\text{observer}} \left(\frac{B_{\parallel}}{\mu\mathrm{G}}\right) \left(\frac{n_e}{\mathrm{cm}^{-3}}\right) \left(\frac{dl}{\mathrm{pc}}\right) \ \mathrm{rad\,m}^{-2}\,, \tag{2.12}$$

where e and m_e are, respectively, the charge and the mass of the electron, c is the speed of light, ϵ_0 is the permittivity of free space, $B_{\parallel}$ is the line of sight component of the magnetic field in the medium, n_e is the thermal plasma density and l is path length from the source to the observer. The positive or negative value of ϕ gives the average direction of the magnetic field as explained for the RM value.

In more realistic astrophysical cases, the polarization angle shows a non-linear behavior as function of λ^2, indicating a complex Faraday structure where synchrotron emission and Faraday rotation are spatially mixed (e.g. O'Sullivan et al. 2012; Pasetto et al. 2018).

Fig. 2.5 shows an example of the Stokes Q and U parameters for a polarized source detected in my work. The Faraday rotation causes the sinusoidal variations in the Stokes Q and U, visible when the signal-to-noise ratio is high enough. The decrease of the amplitude indicates the depolarization of the

signal.

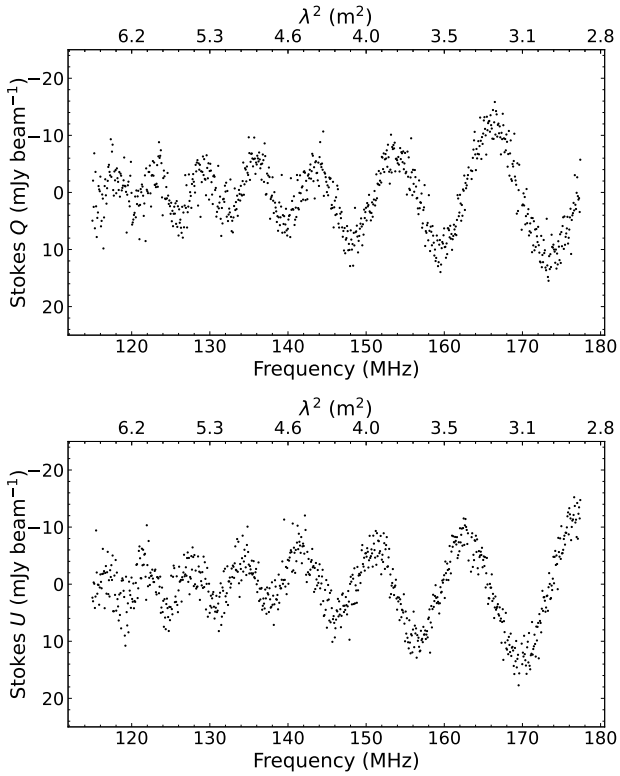

Figure 2.5: Example of a polarized source found in my work (source 07 from Paper I). Top panel: Stokes Q intensity as a function of frequency and wavelength squared λ^2 (bottom and top axes). Bottom panel: Stokes U intensity as a function of frequency and wavelength squared λ^2 (bottom and top axes). The effect of Faraday depolarization is visible in the decrease of the amplitude at lower frequency (larger λ^2).

2.4 Depolarization

A synchrotron polarized radiation that traverses a magneto-ionic medium can undergo two distinct phenomena: Faraday rotation and Faraday depolariza-

tion. Both of these effects can modify the polarization characteristics (polarized flux density and polarization angle) of the radiation. Depolarization arises due to the uniform and/or turbulent magnetic field of the magneto-ionic medium and it is common practice to distinguish between external and internal depolarization, based on whether it occurs during the propagation through the external medium or within the source itself. The degree of polarization of emission from extragalactic sources at 1.4 GHz and 150 MHz is of the order of a few percent (e.g. Tucci et al. 2004; O'Sullivan et al. 2023), therefore much lower that the theoretical value of $\approx 70\%$, indicating that a significant amount of depolarization occurs.

In this section I overview the analytical models aimed at describing the polarization behavior. Such studies on broad-band radio polarization are crucial to characterize the Faraday structure of radio AGN (e.g. O'Sullivan et al. 2012, 2017; Pasetto et al. 2018), as well as the foreground magneto-ionic material of the intracluster medium (e.g. Carretti et al. 2022, 2023), of nearby galaxies (e.g. Mao et al. 2015) and of the Galactic medium (e.g. Thomson et al. 2021).

The depolarization models are obtained from the model of the complex polarized signal in the presence of Faraday rotation in the simplest case:

$$p = \mathrm{p}_0 e^{2i(\chi_0 + \mathrm{RM}\lambda^2)} \,, \tag{2.13}$$

where p_0 is the intrinsic fractional polarization of radiation, χ_0 is the intrinsic polarization angle at the source of the emission and the RM describes the Faraday rotation due to a foreground magneto-ionic medium. Eq. 2.13 describes a sinusoidal behavior of the Stokes Q and U parameters, a constant behavior of the absolute value of p, $|p|$, and a linear behavior of χ (defined in Eq. 2.10), as a function of λ^2, as shown in Fig. 2.6 as example. The depolarization contributions are then added to this simplest model. A schematic representation of the models can be found in Fig. 2.8. Fig. 2.7 shows an example of a source affected by depolarization detected in my work.

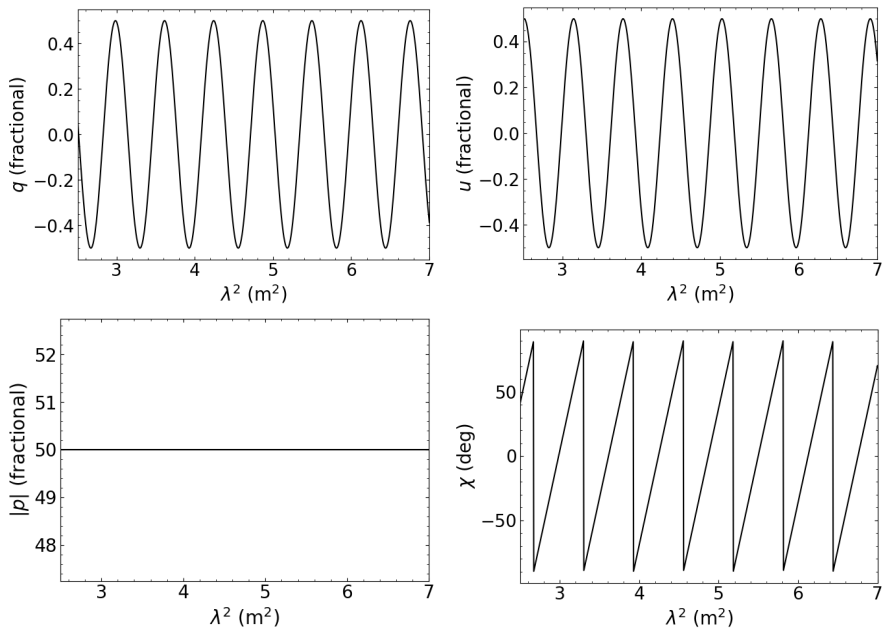

Figure 2.6: Example of polarized signal in presence of Faraday rotation as a function of wavelength squared λ^2 for a signal with $p_0 = 0.5$, $\chi_0 = 45^o$ and RM = 5 rad/m^2. Upper left panel: fractional Stokes parameter $q = Q/I$. Upper right panel: fractional Stokes parameter $u = U/I$. Bottom left panel: amplitude of the fractional polarization. Bottom right panel: polarization angle. The effect of Faraday rotation is visible in the sinusoidal behavior of q and u, in the constant behavior of the absolute value of p and linear behavior of χ.

These models provide a comprehensive yet simplified representation of the depolarization and it is conceivable that different models need to be combined to better describe an observed signal. For example, the changing of $|p|$, as an intra-band repolarization, can be due to multiple interfering RM components, either along the line of sight or on the plane of the sky on scales smaller than our spatial resolution. In fact, several studies have showed that the signal can traverse multiple Faraday-rotating and/or emitting regions and experience a combination of depolarization mechanisms along the line of sight and/or within the beam (e.g. Farnsworth et al. 2011, O'Sullivan et al. 2012 and

Pasetto et al. 2018). In Appendix A I show, as example, the resulting $|p|$ from two RM components interfering inside the beam.

I refer to Burn (1966), Sokoloff et al. (1998), Saikia & Salter (1988) and Pasetto (2021) for comprehensive reviews on the polarization of extragalactic radio sources.

External Faraday dispersion/beam depolarization

The radiation propagates in an external non-emitting Faraday screen. In the Faraday screen the magnetic fields are turbulent, the plane of polarization undergoes a random walk and the variation in the strength and/or direction within the observing beam area causes depolarization. Depolarization occurs also if the magnetic field of the Faraday screen is regular but inside the beam the signal is varying. This depolarization is described by the following equation:

$$p = \mathrm{p}_0 e^{-2\sigma_{\mathrm{RM}}^2 \lambda^4} e^{2i(\chi_0 + \mathrm{RM}\lambda^2)} \,, \tag{2.14}$$

where σ_{RM} is the Faraday dispersion about the mean RM across the source on the sky. The mechanism is represented in picture (e) of Fig. 2.8.

Internal Faraday dispersion

The emitting and Faraday-rotating regions are co-spatial and the magnetic field is both turbulent and regular. The depolarization is represented by picture (b) of Fig. 2.8 and by the equation:

$$p = \mathrm{p}_0 \, \frac{1 - e^S}{S} \,, \tag{2.15}$$

where $S = 2\sigma_{\mathrm{RM}}^2 \lambda^4 - 2i\mathrm{R}\lambda^2$, σ_{RM} is the Faraday dispersion of the internal random field and R is the Faraday depth through the slab.

Differential Faraday rotation

As in the internal Faraday dispersion case, the emitting and rotating regions are co-spatial but the magnetic field is only regular (i.e. the turbulent magnetic field component in Eq. 2.15 is neglected and $\sigma_{\mathrm{RM}} = 0$). In this scenario the radiation coming from the most distant regions will undergo a different amount of Faraday rotation with respect to the regions closest to the observer.

The complex fractional polarization is then given by:

$$p = \mathrm{p}_0 e^{2i\left(\chi_0 + \frac{1}{2}\mathrm{R}\lambda^2\right)} \frac{\sin R\lambda^2}{R\lambda^2} \,, \tag{2.16}$$

where the observable RM is equal to $\frac{1}{2}R$ in this case. The visual explanation can be found in picture (a) of Fig. 2.8.

In case there is a gradient in the Faraday depth within the source, and/or in a foreground screen but local to the emitting region, the magnetic field can be considered uniform. The Faraday depth assumes then the form of an RM and produces a gradient of RM (ΔRM) across the beam. If the internal depolarization is due to a smooth change in the RM across the beam, for a flat beam profile it is described by:

$$p \propto e^{4i\mathrm{RM}_0\lambda^2} \frac{\sin\left(2\Delta\mathrm{RM}\lambda^2\right)}{2\Delta\mathrm{RM}\lambda^2} \,, \tag{2.17}$$

where RM_0 is the initial value of RM within the region ΔRM represent the variation in RM across the beam. Picture (c) of Fig. 2.8 shows the mechanism.

If the gradient of RM originates in a foreground Faraday screen, for flat beam profile Eq. 2.16 comes to be:

$$p = \mathrm{p}_0 e^{2i\mathrm{RM}_0\lambda^2 - 2\sigma_{\mathrm{RM}}^2\lambda^4} \frac{\sin\left(\Delta\mathrm{RM}\lambda^2\right)}{\Delta\mathrm{RM}\lambda^2} \,, \tag{2.18}$$

where σ_{RM} is representative of the random magnetic field effect. The visual explanation is represented in picture (e) of Fig. 2.8.

Bandwidth depolarization

Eq. 2.10 shows that the rotation of the polarization angle increases with the wavelength, decreases with the frequency. If the RM of the polarization angle inside the band is too high, the polarization angle rotates too fast and we cannot resolve and see the rotation, resulting in bandwidth depolarization. For this reason it is fundamental to have a good spectral resolution in the receiver especially at longer wavelengths, i.e. at lower frequencies, where the Faraday rotation is stronger (decreases with the frequency).

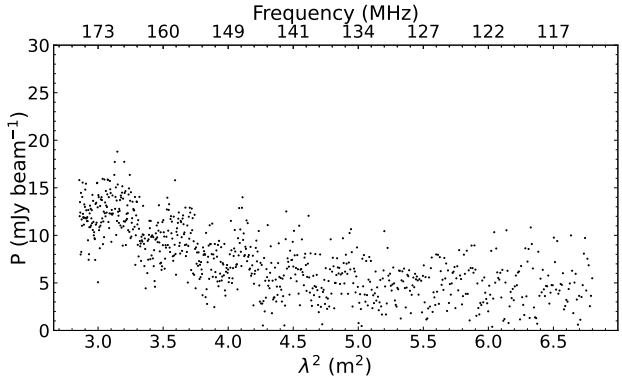

Figure 2.7: Example of polarized intensity as a function of wavelength squared λ^2 and frequency (bottom and top axes) for a polarized source found in my work (source 07 from Paper I). The effect of Faraday depolarization is visible in the decrease of the polarized intensity with λ^2.

2.5 The Faraday Rotation Measure Synthesis Technique

The assessment of the RM values is fundamental to map and characterize the polarized sources and the mgnetized medium across the sky. Traditionally, the RM was determined through a least-squares fit of the observed polarization angle as a function of the square of the observing wavelength (generally two or three). This approach can lead to potential problems (see Heald 2009; Burn 1966; Brentjens & de Bruyn 2005):

1. with polarization angles available at only a limited number of observing wavelengths, the resultant RM values may become ambiguous due to the wrapping of polarization angles within and between these bands. This is the so-called $n\pi$-ambiguity problem;

2. polarized emission from radio sources with different Faraday depth values, ϕ, and therefore different RM values, can be present in a single line of sight. The signal from these different components mixes, making a linear fit inappropriate;

3. polarization angles derived from a linear fit would not be attainable for

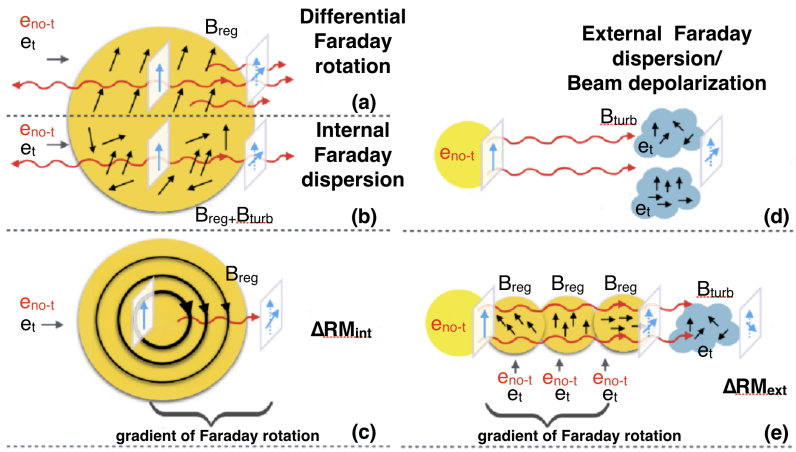

Figure 2.8: From Pasetto et al. (2018). Visual explanation of the depolarization mechanisms given in Sect 2.4. The red undulated arrows represent the synchrotron radiation and the blue arrows represent the polarization of the radiation; the length of this vector decreases when depolarization occurs. Black arrows represent the magnetic field direction. (a) and (b) the cases of internal depolarization where the synchrotron-emitting regions and the Faraday-rotating regions coexist (dark yellow with thermal, e_t, and nonthermal, e_{no-t}, electrons). (a) represents the *Differential Faraday rotation* (Eq. 2.16) where a regular magnetic field is present, (b) represents the *Internal Faraday dispersion* (Eq. 2.15) where a turbulent and a regular magnetic field is present, and (c) represents the depolarization due to an internal gradient of RM (Eq. 2.17); the magnetic field is uniform and throughout the region, the radiation undergoes both fractional polarization and polarization angle smooth changes. (d) represents the case of external depolarization where the synchrotron-emitting region (yellow circle containing e_{no-t}) and the Faraday-rotating region (blue cloud containing e_t) are separated (Eq. 2.14). Here the depolarization is due to the presence of a turbulent magnetic field or to beam depolarization. (e) represents the depolarization due to a gradient of RM due to the presence of a foreground magneto-ionic region (Eq. 2.18).

faint sources exhibiting high RM. Such sources, characterized by a low signal-to-noise ratio, would remain undetectable in individual channels. Even when integrating across all channels, their detection would be hin-

dered by bandwidth depolarization.

The rotation measure synthesis technique (Burn, 1966; Brentjens & de Bruyn, 2005) permits to overcome these problems.

Let us consider the scenario where multiple polarized sources are extended along the line of sight. The observed complex linearly polarized intensity $\mathcal{P}(\lambda^2)$ is the integration along the line of sight of the polarization emissivity $\varepsilon_{\rm P}(l)$, taking into account the Faraday rotation:

$$\mathcal{P}(\lambda^2) = \int_{\rm source}^{\rm observer} \varepsilon_{\rm P}(l) e^{2i(\chi_0(l)+\phi(l)\lambda^2)} dl \,, \tag{2.19}$$

where $\varepsilon_{\rm P}(l)$ is a fraction of the total emissivity $\varepsilon_{\rm I}(l)$, such that $\varepsilon_{\rm P}(l) = p\,\epsilon_{\rm I}(l)$.

Considering Eq. 2.11 and regarding l as a function of ϕ, we can change the integration variable and write:

$$\mathcal{P}(\lambda^2) = \int_{-\infty}^{\infty} \mathcal{F}(\phi) e^{2i\phi\lambda^2} d\phi \,, \tag{2.20}$$

where the quantity

$$\mathcal{F}(\phi) = \int_{-\infty}^{\infty} \varepsilon_{\rm P}(l)\, e^{2i\chi_0(l)} \delta(\phi - \phi(l)) dl \tag{2.21}$$

is named *Faraday dispersion function*, or *Faraday spectrum*. The Faraday dispersion function describes the intrinsic polarized flux as a function of the Faraday depth. Here, we highlight that the observed polarization originates from emission at all possible values of ϕ.

Eq. 2.20 has the form of a Fourier transform, that could, in principle, be inverted to find the intrinsic polarization in terms of observable quantities:

$$\mathcal{F}(\phi) = \int_{-\infty}^{\infty} \mathcal{P}(\lambda^2) e^{-2i\phi\lambda^2} d\lambda^2 \,, \tag{2.22}$$

if one makes assumption on the value on $\mathcal{P}(\lambda^2)$ for $\lambda^2 < 0$, indeed it has a physical meaning only for $\lambda^2 \geq 0$. In this context, Brentjens & de Bruyn (2005) introduced the weight function $W(\lambda^2)$, which is equal to 1 if $\mathcal{P}(\lambda^2)$ is measured and 0 otherwise. The observed polarized emission $\tilde{\mathcal{P}}(\lambda^2)$ can be

expressed as:

$$\tilde{\mathcal{P}}(\lambda^2) = W(\lambda^2)\mathcal{P}(\lambda^2) = W(\lambda^2)\int_{-\infty}^{\infty} \mathcal{F}(\phi)e^{2i\phi\lambda^2}d\phi\,. \tag{2.23}$$

The reconstructed Faraday dispersion function $\tilde{F}(\phi)$ is then:

$$\tilde{\mathcal{F}}(\phi) = K\int_{-\infty}^{\infty} \tilde{\mathcal{P}}(\lambda^2)e^{-2i\phi\lambda^2}d\lambda^2 = \tilde{\mathcal{F}}(\phi) * \mathcal{R}(\phi)\,, \tag{2.24}$$

with $K = \left(\int_{-\infty}^{\infty} W(\lambda^2)d\lambda^2)\right)^{-1}$. Here $*$ is the convolution operation and $\mathcal{R}(\phi)$ is the Rotation Measure Transfer Function (RMTF), or Rotation Measure Spread Function (RMSF). The RMTF is expressed as:

$$\mathcal{R}(\phi) = K\int_{-\infty}^{\infty} W(\lambda^2)e^{-2i\phi\lambda^2}d\lambda^2\,, \tag{2.25}$$

therefore it contains only information about the measurement conditions.

If for each of the N observed frequency channels $\phi\, d\lambda^2 \ll 1$, the rotation measure synthesis technique can be implemented using the equations:

$$\tilde{\mathcal{F}}(\phi) \approx K\sum_{i=1}^{N} \tilde{\mathcal{P}}_i e^{-2i\phi(\lambda_i^2-\lambda_0^2)}\,, \tag{2.26}$$

$$\mathcal{R}(\phi) \approx K\sum_{i=1}^{N} W_i e^{-2i\phi(\lambda_i^2-\lambda_0^2)}\,, \tag{2.27}$$

$$K = \left(\sum_{i=1}^{N} w_i\right)^{-1}, \tag{2.28}$$

where λ_i^2 is the λ^2 that corresponds to the central frequency of the channel i, $\tilde{\mathcal{P}}_i = \tilde{\mathcal{P}}(\lambda_i^2) = w_i\mathcal{P}(\lambda_i^2)$ and $w_i = W(\lambda_i^2)$. The constant shift λ_0^2 is the weighted average of the observed λ^2 and is introduced to attenuate the oscillations of the real part of the reconstructed approximation to the Faraday dispersion function and RMTF. Indeed, the real and imaginary parts of the RMTF have big oscillations in the main maximum, and it can make difficult to calculate the polarization angle χ.

The RM synthesis technique uses a series of trial RM values and finds the one which maximizes the signal level resulting from the coaddition of the polarized flux from all channels. The flux as a function of ϕ, $\tilde{F}(\phi)$, peaks at the value of ϕ corresponding to the RM of the source. At other values of ϕ, the polarization will not constructively interfere throughout the band, and the total flux will be lower. The RM synthesis minimizes the $n\pi$ ambiguity by splitting up the observing bandwidth into many individual narrow frequency channels: only the brightest polarized emission will be detected above the noise level in each narrow channel. The RM synthesis is also capable of detecting emissions at multiple Faraday depths along a particular line of sight, this helps to distinguish the contributions from different objects along the same line of sight.

The theoretical limits for what is possible to detect with RM synthesis involve the channel width $\delta\lambda^2$, the width of the distribution $\Delta\lambda^2$ in λ^2-space, and the shortest wavelength squared $\lambda^2_{\rm min}$. For a top hat weight function which is 1 between $\lambda^2_{\rm min}$ and $\lambda^2_{\rm max}$ and zero elsewhere, we can estimate the resolution in Faraday space $\delta\phi$, the maximum observable Faraday depth *maxscale* and the largest scale in ϕ space to which one is sensitive:

$$\delta\phi \approx \frac{2\sqrt{3}}{\Delta\lambda^2}\,, \tag{2.29}$$

$$maxscale \approx \frac{\pi}{\lambda^2_{\rm min}}\,, \tag{2.30}$$

$$||\phi_{\rm max}|| \approx \frac{\sqrt{3}}{\delta\lambda^2}\,. \tag{2.31}$$

The maximum scale, *maxscale*, gives the upper limit to which structures in ϕ–space are smaller than the maximum scale can be resolved, but larger structures are not detected as a whole structure. The largest scale in ϕ-space to which one is sensitive, $||\phi_{\rm max}||$, gives the maximum value in ϕ-space which can be detected with a sensitivity greater than 50%.

The RM-synthesis technique can be thought of as a method where different trial RM values, $\phi_{\rm test}$, are tested, and the one maximizing the signal level from combined polarized flux across all channels is chosen. Therefore the flux, described by the reconstructed Faraday dispersion function, $\tilde{F}(\phi)$, peaks at the actual RM of the source ϕ_0. If $\phi_{\rm test}$ assumes different values than ϕ_0, the polarization vector rotates at an incorrect rate in λ^2 space and does not

constructively interfere throughout the band, resulting in a lower total flux. Fig. 2.9 shows an example of Faraday spectrum of a polarized sources detected in our data.

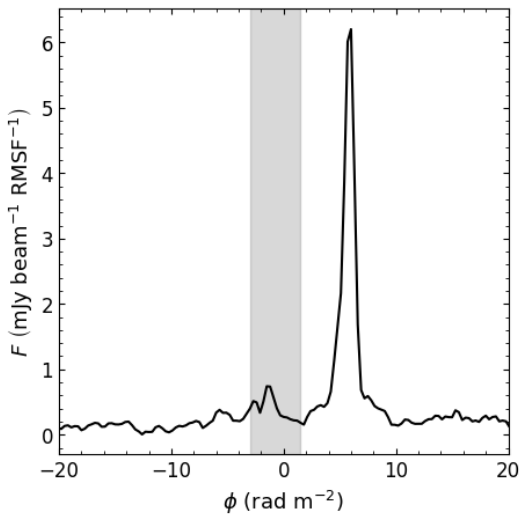

Figure 2.9: Example of Faraday spectrum of a polarized source found in my work (source 07 from Paper I). The peak is located at the actual RM of the source. The height of the peak is the polarized intensity per RMSF.

2.6 qu-fitting

A powerful technique that allows a description of the Faraday complexity of magneto-ionic medium of the radio source environment is the qu-fitting. The qu-fitting consists of modeling the q and u parameters, defined as $q = {}^{Q}/_{I}$ and $u = {}^{U}/_{I}$ (or equivalently, fractional polarization and polarization angle), using wavelength-dependent analytical models, to exploit the recent broad-band polarization observations and determine the more plausible scenario causing the depolarization of the radiation. We refer to Pasetto (2021) for a review on this method.

The importance of this technique was highlighted by Farnsworth et al. (2011). Studying a sample of sources at 350 MHz and comparing the re-

sults from RM-synthesis and qu-fitting, they found that the last method gives a more comprehensive description of the Faraday structures along the line of sight.

O'Sullivan et al. (2012) used qu-fitting in the range 1-3 GHz and demonstrated that a simple RM component modified by depolarization from a foreground Faraday screen was not adequate to describe some sources. They suggested that polarized structures come from the compact inner regions of the radio sources themselves (either from their intrinsic emissions or from their local environments) and not from polarized emissions from galactic or intergalactic foreground regions. This has very important implications for using background extragalactic radio sources as probes of the Galactic and intergalactic magneto-ionic media, indeed they showed that narrow-bandwidth observations can produce erroneous results on RM estimations in case of multiple interfering Faraday components. They further suggest that this may contribute significantly to any RM time variability seen in RM studies at the same angular scale.

O'Sullivan et al. (2017) found no significant difference between the Faraday rotation or Faraday depolarization properties of jet-mode (objects with weak or non-existent optical emission lines, possibly due to radiatively inefficient accretion) and radiative-mode (objects with strong, high-ionization, optical emission lines powered by accretion onto the central super-massive black holes at rates in excess of about 1% of the Eddington limit) AGN. They showed that generally sources with high integrated degrees of polarization at 1.4 GHz have low Faraday depolarization, are typically dominated by a single RM component, have a steep spectral index and have a high intrinsic degree of polarization. They found no significant difference between the Faraday rotation or Faraday depolarization properties of jet-mode and radiative-mode AGN. However, the jet-mode sources showed more intrinsically ordered magnetic field structures than the radiative-mode sources, and may be related to the inner jet regions of FR I radio galaxies where the magnetic field is expected to have a high degree of order.

At 1-12 GHz Pasetto et al. (2018) found that for a sample of sources with high RM, the very large RM and strong depolarization were due to turbulent magnetic fields local to the sources in most cases.

The qu-fitting method has not only been applied to extragalactic sources but also in our Galaxy. For example, Thomson et al. (2021) found that Galactic

Faraday spectra can be produced by several Faraday dispersive sources along the line of sight.

The most recent studies use a model adopted by O'Sullivan et al. (2017) for the complex polarization:

$$p_j = q_j + u_j = \mathrm{p}_{0,j}\, e^{2i\left(\chi_0 + \mathrm{RM}_j \lambda^2\right)} \frac{\sin \Delta\mathrm{RM}_j \lambda^2}{\Delta\mathrm{RM}_j \lambda^2} e^{-2\sigma^2_{\mathrm{RM,j}} \lambda^4} \,, \tag{2.32}$$

where a more complicated behavior is obtained by adding extra jth complex polarization components (Pasetto et al., 2018; Anderson et al., 2019; Thomson et al., 2021). This model describes the effects of both random and uniform magnetic fields and uses a simple multiplication of various factors; while it is a useful equation to use to capture a broad range of possible Faraday rotation behavior, it does not exactly correspond to a physical reality (the corrected equation would be more complicated; see, e.g. Sokoloff et al. 1998).

2.7 Rotation Measure Grid

RM values of discrete extragalactic polarized sources can be used to build a Rotation Measure grid of the sky, an important resource to investigate cosmic magnetism at different scales (Heald et al., 2020).

The observed RM from an extragalactic source, $\mathrm{RM_{obs}}$, is given by the sum of all the RM due the magneto-ionic media between the source and observer: the Galactic interstellar medium, any intergalactic magnetic fields, intervening galaxies on the line of sight, as well as magnetic fields in the source itself. The observed RM is affected by measurement errors, $\mathrm{RM_{noise}}$, as well:

$$\mathrm{RM_{obs}} = \mathrm{RM_{Extragal}} + \mathrm{RM_{Gal}} + \mathrm{RM_{ion}} + \mathrm{RM_{noise}} \,, \tag{2.33}$$

where $\mathrm{RM_{Extragal}}$ is the extragalactic RM contribution, $\mathrm{RM_{Gal}}$ is due to the Galactic medium, $\mathrm{RM_{ion}}$ is the contribution from the time-variable RM of the Earth's ionosphere.

After correction for the ionospheric contribution, we obtain the rotation measure:

$$\mathrm{RM} = \mathrm{RM_{obs}} - \mathrm{RM_{ion}} \,. \tag{2.34}$$

An estimate of the extragalactic RM is calculated by subtracting the Galac-

tic RM component. This so-called Residual Rotation Measure (RRM) is:

$$\mathrm{RRM} = \mathrm{RM} - \mathrm{RM}_{\mathrm{Gal}} + \mathrm{RM}_{\mathrm{noise}}\,, \tag{2.35}$$

A large number of studies use the RM grid to probe the Galactic magnetized foreground (e.g. Hutschenreuter et al. 2022; Reissl et al. 2023) and the extragalactic magnetized Universe (e.g. Vacca et al. 2016; Carretti et al. 2022). In particular, the Galactic contribution is determined by distinguishing between Galactic and extragalactic components based on the similarity of RM values of nearby sources in the sky. Indeed, extragalactic emission should be uncorrelated on angular scales of the order, or larger than, arcminutes, while large scale correlation should likely be due to local effects (Akahori & Ryu, 2010). Large-scale magnetic field in proximity to our Galaxy may be exceptional cases (Xu et al., 2006).

Early RM grid studies were conducted at 1.4 GHz and contain large systematic uncertainties, due to their poor frequency sampling. Among them, the catalog of Taylor et al. (2009), produced from the NRAO VLA Sky Survey (NVSS, Condon et al. 1998), remains the most complete single all-sky polarization survey. The catalog contains RM values for 37 543 lines of sight to polarized radio sources and covers the 82% of the sky north of declination $-40°$, with an average number density of 1 polarized source per deg^2.

A new generation of radio telescopes operating at lower frequencies is mapping the sky with high precision on the inferred RM values through low-frequency broad-band polarimetry.

In the southern hemisphere, S-PASS/ATCA (Australia Telescope Compact Array, Schnitzeler et al. 2019) cataloged about 3800 RMs of polarized sources in the range 1.3–3.1 GHz. The POlarised GLEAM Survey (POGS) cataloged 517 RMs covering 25 489 deg^2 of the sky between declinations $+30°$ and $-82°$ in the frequency range 169–231 MHz (Riseley et al., 2018, 2020). The Spectral and Polarisation in Cutouts of Extragalactic sources from the Rapid ASKAP Continuum Survey (SPICE-RACS, Thomson et al. 2023) lists around 6000 RMs found in the frequency range 744–1032 MHz across 1300 deg^2. Recently, pilot observations from the Australian Square Kilometre Array Pathfinder (ASKAP, Hotan et al. 2021) were used to produce prototype RM grids and show the capabilities of the Polarisation Sky Survey of the Universe's Magnetism (POSSUM, Gaensler et al. 2010; Vanderwoude et al. 2024), and make denser RM grids for smaller regions of the sky (Anderson et al., 2021).

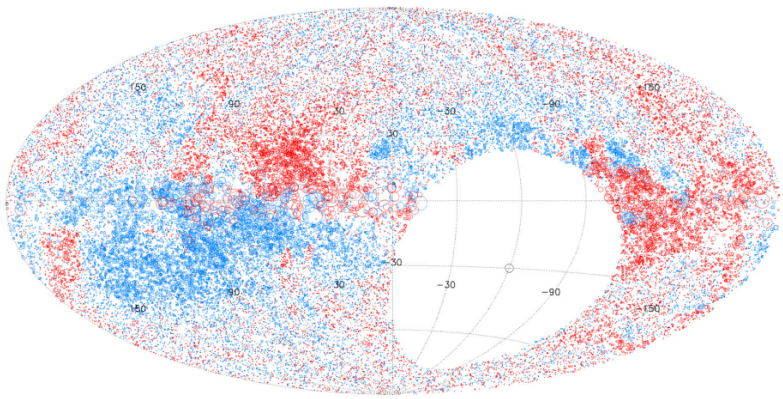

Figure 2.10: RM grid at 1.4 GHz. Red circles are positive rotation measure and blue circles are negative. The size of the circles scales linearly with the magnitude of rotation measure. From Taylor et al. (2009)

Using SKA1-mid at ∼1 GHz, a proposed future RM grid is expected to cover a large field of view and, reaching μJy sensitivity levels, may provide a density ∼300–1000 times higher than the current RM grid based on the NVSS survey (Govoni et al., 2014). In the frequency range 50–350 MHz, SKA1-Low will observe the sky at a resolution of $10''$ and sensitivity of 20 μJy beam^{-1} after an hour of observing time.

In the northern hemisphere, the APERture Tile in Focus (Apertif), a phased-array feed for the Westerbork Synthesis Radio Telescope (WSRT), surveyed an area of 56 deg^2 and detected 1357 RM from 1170 polarized sources in the frequency range 1220–1520 MHz (Adebahr et al., 2022). A polarization all-sky survey will be conducted also at 2–4 GHz with the Very Large Array Sky Survey (VLASS, Lacy et al. 2020).

In the frequency range of 120 to 168 MHz the LOFAR Two-Metre Sky Survey (LoTSS) collected RM values in two northern fields (O'Sullivan et al., 2023). In addition to these surveys, deeper polarization studies on smaller fields were carried out, allowing for denser grids (e.g. Neld et al. 2018; Herrera Ruiz et al. 2021 at 120–168 MHz). I will return to RM grid studies with LOFAR in Sect. 4.

Fig. 2.11 shows a plot from Heald et al. (2020), where RM grid survey

parameters of various existing and future radio surveys are illustrated. I added a point, highlighted in the red box, to illustrate where my research on polarized sources fits within this context, which will be explained in detail in Chap. 5.

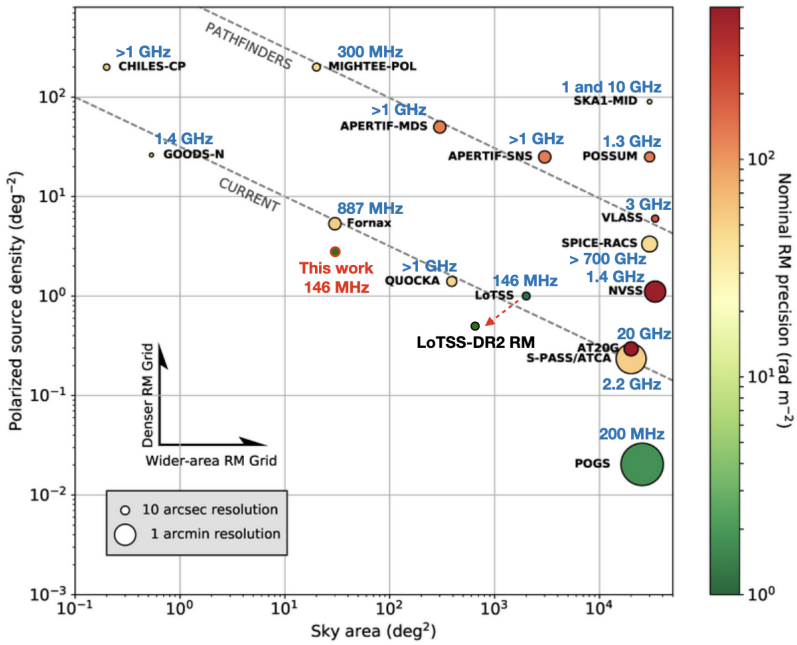

Figure 2.11: From Heald et al. (2020): illustration of the RM Grid survey strengths of various existing and future radio surveys. The size of each marker reflects the angular resolution of the survey, and the color indicates the nominal RM precision that can be reached, where green indicates the capacity for measurements with lower RM uncertainties. Diagonal dashed lines highlight the locus of "current" (lower) and "pathfinder" (upper) survey capability. The added point highlighted in red corresponds to my work (sky area of 25 deg^2 and polarized source density of 1.3 deg^{-2}) that will be introduced in Sect. 5. The point indicated by the red arrow represents the updated result from the LoTSS-DR2 RM catalog (O'Sullivan et al., 2023).

Since RM values correspond to line-of-sight integrations of physical quanti-

ties, it is crucial to attribute optical counterparts and redshifts to the sources constituting the RM grid. This attribution is fundamental for distinguishing the different contributions to RM values originating from magnetic fields at different distances.

In environments characterized by dense and/or multiple magneto-ionic media, some radio source populations experience depolarization at longer wavelengths but remain observable at shorter wavelengths. The combination of RM grid catalogs at different radio wavelengths holds the potential to enhance our comprehension and differentiation of the diverse contributions to Faraday rotation along the line of sight. Vernstrom et al. (2019) studied the RM and the variance of the RM difference between physical pairs (e.g. double-lobed radio galaxies) and non-physical, random pairs (i.e. physically different sources with close projected separations on the sky) in the NVSS; they found that polarized extragalactic sources that are close on the sky but at different redshifts have larger differences in RM than do two components of one single source. Furthermore, they were able to set an upper limit on the comoving intergalactic magnetic field strength of 40 nG. With the same strategy but using the first release of the LOFAR Two-metre Sky Survey (120 to 168 MHz, Shimwell et al. 2019), O'Sullivan et al. (2020) found no significant difference between the RM distributions of the physical and non-physical pairs and placed an upper limit on the comoving magnetic field strength of 4 nG. Carretti et al. (2022) used the LoTSS-DR2 RM and comparison with NVSS to detect and measure magnetic fields in cosmic web filaments. They suggested that the observed extragalactic RM and degree of polarization are most likely to have an origin local to the source at 1.4 GHz, while at 144 MHz they generated in the cosmic web filaments, and they estimated a magnetic field in filaments of $\simeq$30 nG. In a follow up paper (Carretti et al., 2023) used these data to estimate the behavior with redshift of the magnetic field in cosmic web filaments, deriving a better estimation of 32 ± 3 nG in filaments.

Over the past decades, many surveys and independent projects measured RM across the sky for a broad range of astronomical studies. These individual catalogs have been published in many different places and in many different formats, making it difficult to collect and homogenize them. Van Eck et al. (2023) proposed a standard which defines a set of parameters that are beneficial to include in RM catalogs when publishing radio polarization data, with the aim of making data as easy as possible to access and use.

CHAPTER 3

Polarized source counts

Total source counts, i.e. counts of sources as a function of total flux density, and *polarized source counts*, i.e. counts as a function of polarized flux density, are useful tools for studying the statistical properties and cosmological evolution of radio sources. A historical pivotal achievement in the study of source counts was the evidence against non-evolving (Steady State) cosmological models, as I will give an overview in Sect. 3.2. This motivated numerous studies to develop models that describe the cosmic evolution of extragalactic radio sources. The source counts indeed result from the evolution of the local luminosity function of sources across all redshifts. For instance, Šlaus et al. (2024) modeled the evolution of active galactic nuclei by constructing their radio luminosity functions, demonstrating that a model featuring luminosity-dependent density evolution (where the number density of sources changes with redshift and depends on their luminosity) better describes the source counts in the 151–3000 MHz frequency range. An additional use of source counts is in the context of constraining the star and galaxy formation history of the Universe. Matching the local luminosity functions of star-forming galaxies and active galactic nuclei to radio source counts using combinations of luminosity and density evolution, it is possible to show that the star for-

mation rate density grows rapidly at early times, peaks at "cosmic noon" (at redshift of 2), and subsequently decreases (e.g. Matthews et al. 2021).

Polarized source counts of very faint sources can be used to predict the number density of rotation measures that will be produced by future deep polarization surveys with the SKA (Beck & Gaensler, 2004; O'Sullivan et al., 2008; Stil et al., 2014). Furthermore, polarized source counts are important for studies of primordial polarization in the Cosmic Microwave Background (CMB), as polarization from extragalatic sources contaminates the polarized signal from the CMB and its contribution to the power spectrum must be estimated and removed (i.e. Tucci & Toffolatti 2012; Puglisi et al. 2018).

Polarized source counts are often calculated from the total source counts since, especially at low radio frequencies, the small number of polarized sources is not sufficient for statistical studies. Most of the studies on this topic have been conducted at 1.4 GHz. Beck & Gaensler (2004) constructed a polarized source counts model from data of polarized sources in NVSS Condon et al. (1998) to predict detection statistics for the SKA RM Survey. Stil et al. (2014) derived the polarized radio source counts from stacked NVSS data, predicting fewer polarized radio sources for future surveys as the SKA and its pathfinders. Mesa et al. (2002) and Tucci et al. (2004) also used NVSS data to study the fractional polarization distributions for steep- and flat/inverted-spectrum sources, finding their distributions to exhibit a log-normal form. O'Sullivan et al. (2008) modeled polarized sources using data from NVSS and the DRAO ELAIS-N1 deep field survey of Taylor et al. (2007), using a luminosity-dependent model for the polarization of FR I and FR II radio galaxies.

Empirical studies on polarized source counts at 1.4 GHz were carried out in several projects (Taylor et al., 2007; Grant et al., 2010; Subrahmanyan et al., 2010; Hales et al., 2014b; Berger et al., 2021), covering areas of several degrees. The deepest polarized source counts so far were conducted by Rudnick & Owen (2014) (down to a noise level of about 3 μJy beam^{-1}), for a small area of approximately 0.3 deg^2 (the GOODS-N field), and by Grant et al. (2010) (down to a noise level of about 45 μJy beam^{-1}) for an area of 16.15 deg^2 (the ELAIS-N1 field).

Deeper survey with lower sensitivity σ and wide field of view would improve our knowledge on polarized source counts. Indeed, for instance, an anti-correlation trend between fractional polarization and total flux density

of the faint extragalactic radio source population at 1.4 GHz was observed by Mesa et al. (2002), Tucci et al. (2004), Taylor et al. (2007) and Grant et al. (2010), and it was supposed to be dependent on physical properties of the sources. Reaching a better sensitivity, Hales et al. (2014b) ($\sigma \sim$100 μJy beam^{-1}) and Berger et al. (2021) ($\sigma \sim$7 μJy beam^{-1}) found this relation to have its origin from the incompleteness affecting the faintest sources in the sample. Wider fields of view instead minimize the cosmic variance that may cause differences between the results of small fields.

In the following sections I explain the theory of source counts following Condon & Ransom (2016) and Condon (1988). While I present the definition of total source counts in Sect. 3.1, the methodology extends to polarized source counts, which are the subjects of my analysis and will be showcased in figures and tables. In Sect. 3.2 I will explain how the source counts are computed, and in Sect. 3.3 how the polarized source counts can be modeled.

3.1 Definition

Statistical samples of the radio source population are given by radio surveys. Let us consider a radio survey that covers a certain region of the sky Ω, in sr or deg^2, at frequency ν and is complete above a flux density $S_{\rm lim}$. We can compute the histogram of the flux density values S of the sources, in order to see how many sources have a flux density in the bin ΔS. Fig. 3.1 shows the histogram of the polarized flux densities of sources detected in a region of 25 deg^2 at 150 MHz in our studies (more details in Sect. 5).

To facilitate the comparison between results from different surveys, the number of sources is normalized by the area covered by the survey and by the width of the polarized flux density bin.

During the normalization by unit of area, we must take into account that our data are primary-beam corrected. The primary beam can be considered as the sensitivity of the interferometer as a function of direction. The antennas of an interferometer are not uniformly sensitive to incoming radiation from all directions, and the maximum sensitivity is reached at the center of the image and drops off in the outskirt. Primary-beam-corrected images are obtained by dividing the image by the primary beam of the telescope, that generally is described by a Gaussian function. This corrects the intensities, but also increases the noise of the resulting image towards the edge of the map. For a

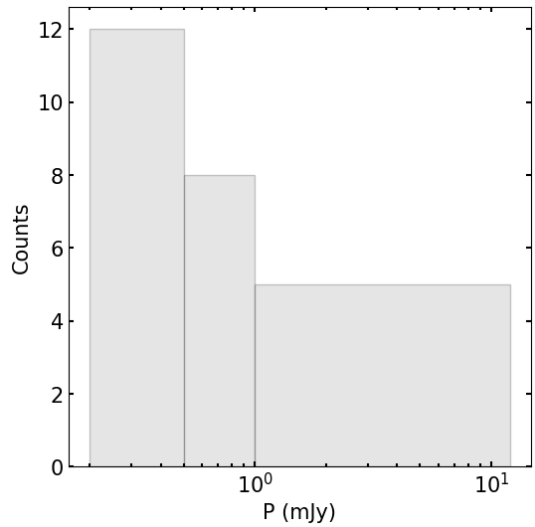

Figure 3.1: Histogram of polarized flux densities for a population of polarized source detected in the ELAIS-N1 LOFAR deep field in my work.

Gaussian primary beam, the noise σ varies with the radius r as:

$$\sigma = \sigma_0 e^{-\frac{r^2}{2\sigma^2}} , \tag{3.1}$$

where σ_0 is the noise at the center of the field. In Fig. 3.2 and 3.3 we see the noise map and its the noise values as a function of the radius, that can be used to infer the shape of the primary beam of our telescope.

If we combine Eq. 3.1 with the expression for the full width half-maximum of the Gaussian beam θ_{FWHM}, $e^{-\frac{(\theta_{\mathrm{FWHM}}/2)^2}{2\sigma^2}} = 1/2$, we can express the area A of the image with noise less than a certain value σ as:

$$A(\text{noise} < \sigma) = \frac{\pi}{4\ln 2}\, \theta^2_{\mathrm{FWHM}} \ln \frac{\sigma}{\sigma_0} . \tag{3.2}$$

Imposing a threshold in the signal-to-noise ratio for detection, the effective area A_{eff} in which we can actually find a polarized source depends on the noise in the image. Therefore we can detect the faintest polarized sources only in the center of the image. For this reason the number of sources N in each bin

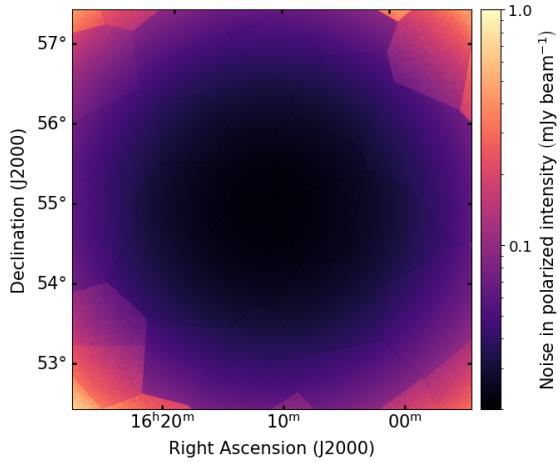

Figure 3.2: Noise map over the field studied in my work on ELAIS-N1. A Gaussian primary beam should lead to a noise map where the noise increases with the radius from the center of the field. Here this behavior is visible but not immediately evident due to the data calibration process, which divides the field into facets, distinguishable in the image.

normalized by unit of area, n_{eff}, is computed using the effective area A_{eff}:

$$n_{\text{eff}} = \frac{N}{A_{\text{eff}}}\,, \tag{3.3}$$

where A_{eff} indicates the area where the noise is small enough we can detect a source with polarized flux density with at a given signal to noise-ratio.

Differential number counts $n(S)$, in $\text{sr}^{-1}\text{Jy}^{-1}$ or $\text{deg}^{-2}\text{Jy}^{-1}$, are defined as the number of sources per unit area with flux density between S and $S + dS$:

$$n(S) = \frac{dn_{\text{eff}}}{dS}\,. \tag{3.4}$$

The differential number counts in polarization from our data are shown in Fig. 3.4.

Cumulative source counts $N(\geq S)$ give the distribution of the number of

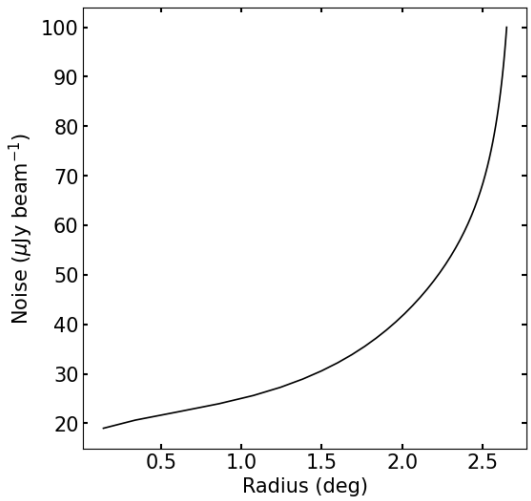

Figure 3.3: Noise values as a function of the radius of the noise map of my work. Here we can see clearly how the noise increases with the radius, with trend that reflects the Gaussian shape of the primary beam.

sources per unit of area brighter than a flux density S:

$$n_{\rm cum}(>S) = \int_S^{+\infty} n(S)dS = \int_S^{+\infty} \frac{dN}{dS} dS \,. \tag{3.5}$$

3.2 Measurements in total flux density and polarized flux density

Let us consider first the measurements in total flux density.

In a static Euclidean Universe uniformly filled with sources of luminosity L and density ρ, the number of sources N can be expressed as the product of ρ and the volume V. In a spherical volume of radius r, N is:

$$N = \rho V = \rho \frac{4}{3} \pi r^3 \,, \tag{3.6}$$

We can observe only the sources above the flux density limit of our survey, then we are able to observe only the sources within a certain radius r that

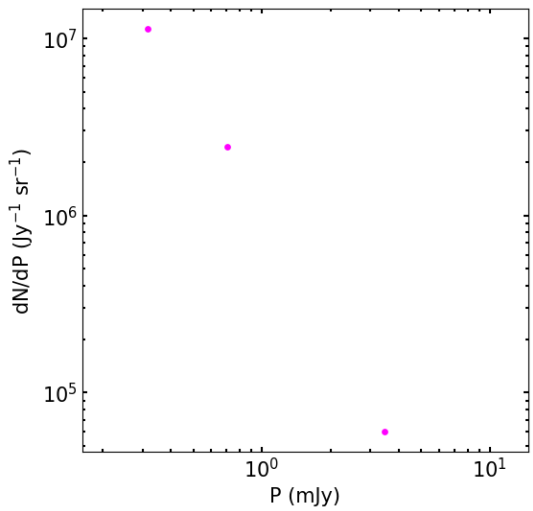

Figure 3.4: Differential polarized source counts for a population of polarized sources detected in the ELAIS-N1 LOFAR Deep Field in my work.

depends on L and S:

$$r = \left(\frac{L}{4\pi S}\right)^{\frac{1}{2}} . \tag{3.7}$$

The number of sources is therefore related to S:

$$N \propto S^{-\frac{3}{2}} , \tag{3.8}$$

and the differential number $n(S)$ depends on S as:

$$n(S) = \frac{dN}{dS} \propto S^{-\frac{5}{2}} . \tag{3.9}$$

Plotting the *Euclidean normalized differential source count* $n(S)S^{\frac{5}{2}}$ as a function of S should then yield a horizontal line in a static Euclidean Universe. However, the observations at radio frequencies show a different trend, as demonstrate in Figure 3.5 from Condon (1984) at 1.4 GHz. Indeed, the slope of source counts was studied and used as evidence against the non-evolving, Steady State cosmological models from early radio surveys (e.g.

Ryle & Scheuer 1955). The slope of the source counts is determined by the different types of sources that contribute at every flux, that depends on their luminosity function at various redshifts. In Fig. 3.5 the dashed line in the flux density range $10^{-5} < S < 10^{-2}$ Jy is representative of the star forming galaxy population; the dashed line in the flux density range $2.5\times10^{-4} < S < 1$ Jy corresponds to the AGN population, and the plateau above 1 Jy is related to the bright local radio sources.

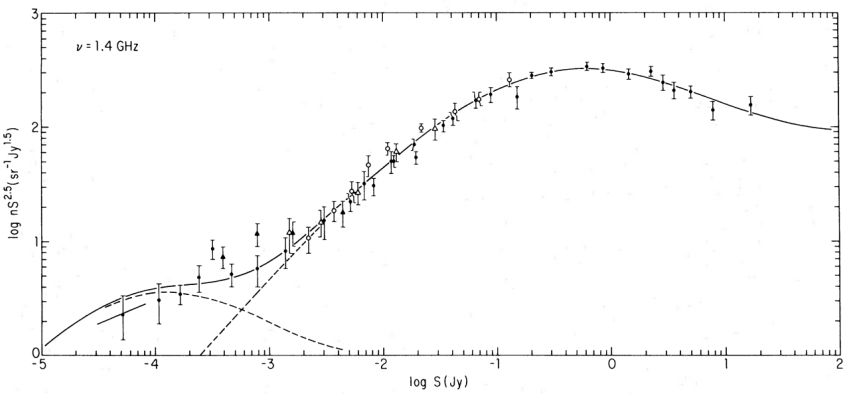

Figure 3.5: Euclidean normalized differential source counts in total flux density at 1.4 GHz. From Condon (1984).

Similar slopes in total source counts are found also at 150 MHz, as shown in Figure 3.6, where the euclidean normalized source counts from Mandal et al. (2021) are reported.

Euclidean normalized differential source counts are computed also in polarization. Figure 3.7 shows the total flux density and polarized flux density Euclidean normalized differential source counts at 1.4 GHz from Grant et al. (2010). Models are also shown, which will be discuss in the following Sect. 3.3.

3.3 Modeling source counts in polarization

Polarized source counts can be modeled from the total source counts and polarization distributions derived from analysis of polarization observations.

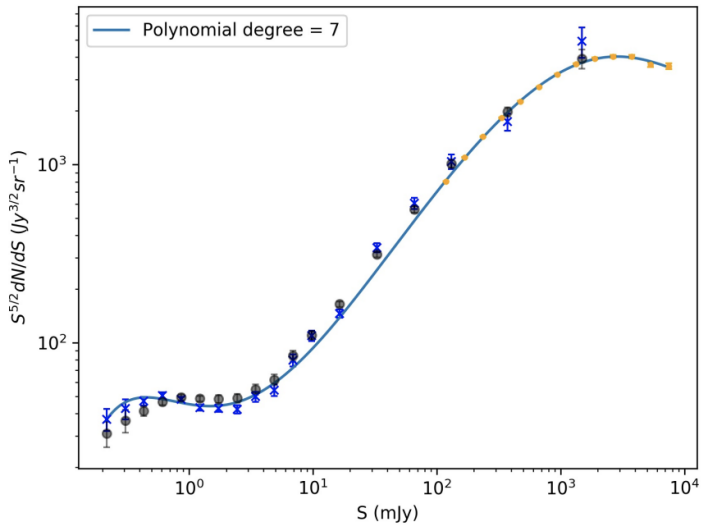

Figure 3.6: Euclidean normalized differential source counts and their best fit in total flux density at 150 MHz, from Mandal et al. (2021).

The simplest model consists in assuming a constant fractional polarization for the source population, then the polarized source counts are made by multiplying the total source counts times the constant fractional polarization (Tucci & Toffolatti, 2012; Stil et al., 2014). We see in Figure 3.8 an example of this method from Tucci & Toffolatti (2012), where they used a constant fractional polarization of 3.3% for all the extragalactic sources.

Other models calculate polarized source counts through the convolution of source counts in total flux density with a probability density function of fractional polarization.

As shown in Tucci & Toffolatti (2012), the polarization number counts $n(P)$ can be expressed as:

$$n(P) = N \int_{S_0}^{\infty} \mathcal{P}(P, S)\, dS\,, \tag{3.10}$$

where N is the total number of sources with total flux density $S \geq S_0$, and $\mathcal{P}(P, S)$ is the probability function of observing a source with polarized flux density P and total flux density S. It is possible to write $\mathcal{P}(P, S)$ in terms of

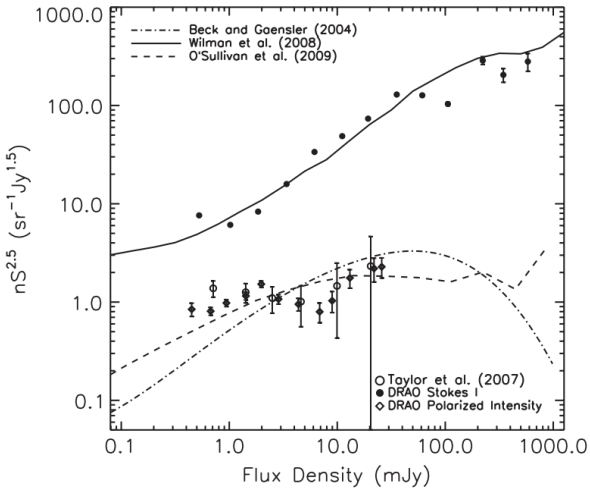

Figure 3.7: Euclidean normalized differential source counts at 1.4 GHz, from Grant et al. (2010). The solid line represents source counts in total flux density, the discontinuous lines are moodeled source counts.

the fractional polarization $\Pi = P/S$:

$$\mathcal{P}(P,S) = \mathcal{P}(\Pi,S)\,\frac{d\Pi}{dP} = \frac{1}{S}\mathcal{P}(\Pi,S)\,, \tag{3.11}$$

and the polarized source counts are then:

$$n(P) = N\int_{S_0=P}^{\infty}\mathcal{P}(\Pi,S)\frac{dS}{S}\,. \tag{3.12}$$

Assuming that $\Pi = P/S$ is independent of S, $n(P)$ can be expressed as

$$n(P) = \int_{S_0=P}^{\infty}\mathcal{P}\left(\Pi = \frac{P}{S}\right)\,n(S)\,\frac{dS}{S}\,, \tag{3.13}$$

where $n(S)$ is the density of number of sources per unit of polarized flux density bin.

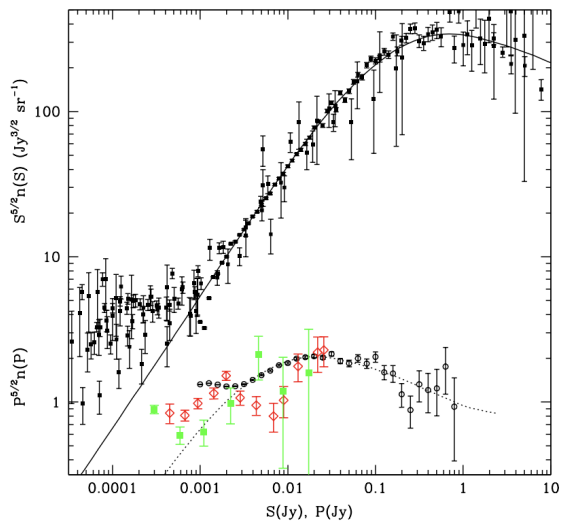

Figure 3.8: Euclidean normalized differential source counts at 1.4 GHz, as function of total intensity (upper points) and of polarized intensity (lower points). The dotted line, that represents the polarized source counts, is obtained by the counts in total intensity (solid line) and assuming a constant fractional polarization of 3.3% for all the extragalactic sources. From Tucci & Toffolatti (2012).

The probability function $\mathcal{P}(\Pi)$ can be modeled as a log-normal distribution:

$$\mathcal{P}(\Pi) = \frac{1}{\sqrt{2\pi}\sigma\Pi} \exp\{-\log[(\Pi/\Pi_{\rm med})]^2/2\sigma^2\} \tag{3.14}$$

where $\Pi_{\rm med}$ and σ^2 are the median and the scale parameter of the distribution, respectively. The reason to use such distribution is due to the work of Mesa et al. (2002), where it is shown that the distribution of the number of sources with flux densities >80 mJy as a function of the fractional polarization in NVSS data can be approximated with a log-normal function, both for steep and flat spectrum sources.

CHAPTER 4

Polarization with LOFAR

4.1 LOFAR

LOFAR, the LOw-Frequency ARray, is a new-generation radio interferometer built in the Netherlands and across Europe. Utilizing a new phased-array design, LOFAR covers the largely unexplored low-frequency range from 10–240 MHz. LOFAR is the largest radio interferometer operating at the lowest frequencies that can be observed from Earth. It uses almost 20 000 small antennas, located mainly in the Netherlands; while other stations are in Germany, Poland, France, Ireland, Latvia, Sweden, and the United Kingdom; stations in Italy and Bulgaria are funded to be built soon. Still more countries are considering to join as well[1]. This interferometer can observe the sky in the 10 to 240 MHz frequency range with two types of antennas: Low Band Antenna (LBA), from 10 to 90 MHz, and High Band Antenna (HBA), from 110 to 250 MHz, with a large number of frequency channels across the observational bandwidth. It can produce Stokes parameters I, Q, U, V, using a large number of channels across an observational bandwidth. These channels allow for measurements of the linearly polarized emission and Faraday rota-

[1] `https://www.astron.nl/telescopes/lofar`

tion. To measure weak magnetic fields in intergalactic space is difficult, but LOFAR provides the ability to measure the Faraday rotation effect of these weak fields with unprecedented accuracy.

Radio observations with LOFAR are making possible several fundamental studies of the Universe. The LOFAR community is currently organized into Key Science Projects (KSPs) which aim to study phenomena closest to us, starting from the Sun, up to the investigation of the early universe at the epoch of reionization (redshift from 6 to 11.4).

Figure 4.1: The LOFAR station in Netherlands. Credits: `https://www.astron.nl/`

The LOFAR community is working also to produce the LOFAR Two-metre Sky Survey (LoTSS) (Shimwell et al., 2017, 2019, 2022), a deep 120-168 MHz imaging survey that will eventually cover the entire northern sky. 3 170 LOFAR pointings will be observed for eight hours, which, at most declinations, is sufficient to produce $6''$ resolution images with a sensitivity of 100 μJy beam^{-1} and accomplish the main scientific aims of the survey, which are to explore the formation and evolution of massive black holes, galaxies, clusters of galaxies and large-scale structure. In comparison to higher frequencies, the LoTSS will match the high resolution achieved by Faint Images of the Radio Sky at Twenty-Centimeters (FIRST; Becker et al. 1995) but over a wider area and, for a typical radio source of spectral index $\alpha \sim 0.7$, it will be 7 times more sensitive. Similarly, the LoTSS will be 20 times more sensitive to typical radio sources than the lower resolution NRAO VLA Sky Survey (NVSS; Condon 1984). The comparison between surveys in terms of sensitivity and resolution is shown in Fig. 4.2.

The LoTSS-data release 1 (LoTSS-DR1) Shimwell et al. (2019) covers 2% of the northern sky, for which a catalogue of more than 325 000 sources is derived from Stokes I continuum maps. The Stokes I continuum maps at

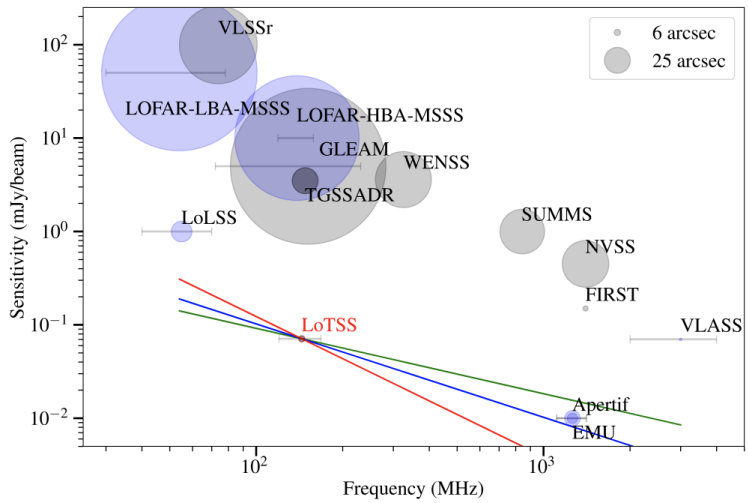

Figure 4.2: Sensitivity, frequency, and angular resolution (linearly proportional to the radius of the markers) of LoTSS-data release 1 (LoTSS-DR1) in comparison to a selection of existing wide-area completed (grey) and upcoming (blue) radio surveys. The horizontal lines show the frequency coverage for surveys with large fractional bandwidths. The green, blue, and red lines show an equivalent sensitivity to LoTSS for compact radio sources with spectral indices of -0.7, -1.0, and -1.5, respectively. From Shimwell et al. (2019).

$6''$-resolution have a sensitivity better than 0.1 mJy beam^{-1}. LoTSS-DR1 includes optical counterparts for 71% of the radio sources (Williams et al., 2019) and photometric redshifts for these sources (Duncan et al., 2019). The lastest data release from LoTSS, the LoTSS-DR2 (Shimwell et al., 2022), covers 27% of the northern sky, and provides a catalog of more than 4 million radio sources. The Stokes I continuum maps at $6''$-resolution have a median rms sensitivity of 83 μJy beam^{-1}. The LOFAR community, together with other astronomers and non-astronomers who were involved through "LOFAR galaxy zoo" project, worked to find the host galaxies of the LoTSS-DR2 catalog, of which 84% have an optical ID candidate and 57% have a spectroscopic or photometric redshift estimate (Hardcastle et al., 2023). The LOFAR community is also working at longer wavelength to produce the LOFAR LBA Sky

Survey (LoLSS) and cover the entire northern sky with 3 170 pointings in the frequency range between 42 to 66 MHz, at a resolution of 15″ and a sensitivity of 1 mJy beam^{-1} (de Gasperin et al., 2021, 2023).

The higher frequency wide area survey LoTSS is complemented by a few deeper fields, known as the LoTSS-Deep Fields (Sabater et al., 2021; Tasse et al., 2021). The deep fields include the Bootes, Lockman Hole, and European Large Area Infrared Space Observatory Survey- North 1 (ELAIS-N1) fields. These fields have a multiwavelength coverage and are ideal to probe a new fainter population of radio sources and study the unknown polarized radio source population at sub-mJy flux densities at very low frequencies.

The LOFAR facilities have been jointly operated by the International LOFAR Telescope (ILT) foundation, recently superceded in 2024 by the LOFAR-ERIC (LOFAR European Research Infrastructure Consortium). With baselines of up to about 2 000 km, LOFAR has the capability of achieving sub-arcsecond resolution imaging (Morabito et al., 2022).

At present, LOFAR LBA is the only telescope that can perform deep, high-resolution imaging below 100 MHz. The LOFAR LBA Sky Survey (LoLSS) will cover the entire northern sky above declination 24° in the frequency range 42-66 MHz, achieving a resolution of 15″ at an average rms noise of 1 mJy beam^{-1} (de Gasperin et al., 2021, 2023). LoLSS will probe new ultra-steep spectrum sources, from high redshift radio galaxies, to ageing radio emitting plasma, to radio-emitting exoplanets.

In the near future, the LOFAR consortium is seeking to advance its capabilities through LOFAR 2.0, facilitating simultaneous observations with HBA and LBA, improving resolution and sensitivity, and ensuring the telescope remains cutting-edge for the coming decade.

LOFAR2.0 will continue to be unique and world-leading instrument, with an angular resolution more than ten times higher than that of the planned Square Kilometre Array low-frequency component (SKA-Low), and also accessing the largely unexplored spectral window below 50 MHz.

4.2 Constraining cosmic magnetic fields with LOFAR

Cosmic magnetic fields at radio wavelengths can be studied indirectly by the Faraday rotation of polarized background emission due to magnetic media

along the line of sight. However, investigation of linear polarization at these frequencies is complicated by the effects of wavelength-dependent depolarization. Observing at low radio frequencies can provide important information on the properties of magnetic fields in low-density plasma regions and weak magnetic fields, but also means that a smaller fraction of radio sources are polarized at detectable levels. Fig. 4.3 shows how the degree of polarization decreases when a polarized radiation propagates in a turbulent slab (external Faraday dispersion, $p \propto e^{-2\sigma_{\rm RM}^2 \lambda^4}$, where $\sigma_{\rm RM}$ is the Faraday dispersion of the field about the mean RM across the source on the sky). For observations in the frequency range 114.9–177.4 MHz (i.e. 2.5–7 m^2), LOFAR is sensitive to values of $\sigma_{\rm RM}$ of the order of 0.3 rad m^{-2}.

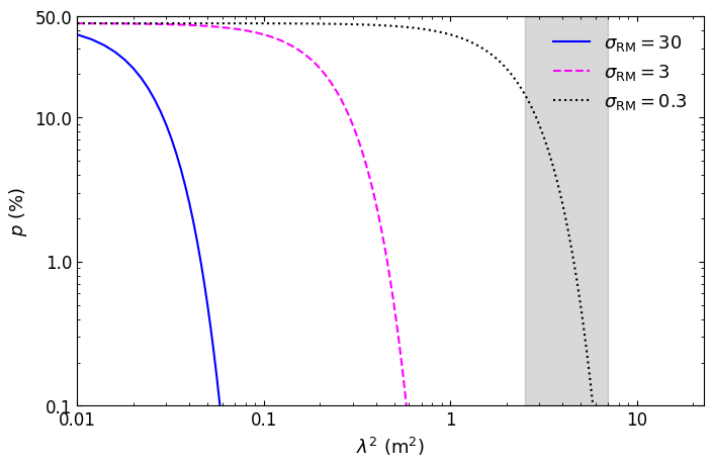

Figure 4.3: Degree of polarization as function of λ^2 in case of external polarization. The lines represent the depolarization behavior in case of different values of $\sigma_{\rm RM}$. The grey region outlines the λ^2 range of the LOFAR observations considered (2.5–7 m^2, that correspond to 114.9–177.4 MHz).

Furthermore, ionospheric Faraday rotation (Sotomayor-Beltran et al., 2013), instrumental polarization, uncertainty in the primary beam model, all makes polarization studies challenging with LOFAR. Calibration and imaging at high resolution ($\leq 1'$) is difficult at low frequencies, so beam depolarization can often be a limitation. Despite these difficulties, polarization studies are possible as the nature of the data and the characteristics of the instrument become

better understood.

Fig. 4.4 shows the RMTF for LOFAR in HBA configuration with 640 equally spaced frequency channels in the range from 114.9 to 177.4 MHz. This permits to reach a resolution in Faraday depth of 0.9 rad m^{-2} (from Eq. 2.29), a maximum observable Faraday depth of 300 rad m^{-2} (from Eq. 2.31), and the largest scale in ϕ space to which the data are sensitive is 1.07 rad m^{-2} (from Eq. 2.30).

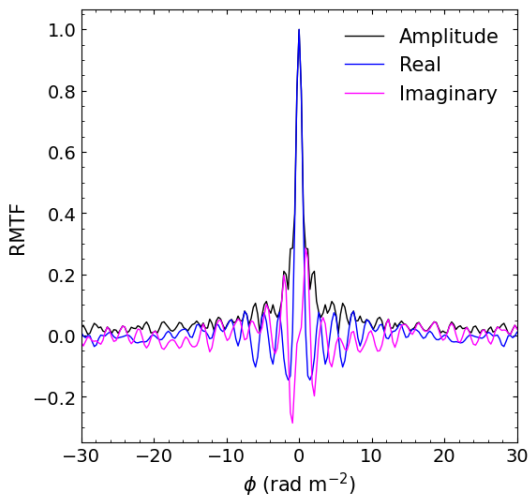

Figure 4.4: LOFAR RMTF in HBA configuration with 640 equally spaced frequency channels in the range from 114.9 to 177.4 MHz.

Following Eq. 2.24, the RM synthesis technique allows to obtain the reconstructed Faraday dispersion function $\tilde{\mathcal{F}}(\phi)$ from the convolution of the true emission, i.e. the Faraday dispersion function $\mathcal{F}(\phi)$, with the RMTF. Faraday components broader than the maximum scale are strongly depolarized and thus filtered out, while Faraday components narrower than the resolution appear as unresolved peaks. Fig. 4.5 shows the absolute $\tilde{\mathcal{F}}(\phi)$ for a simulated $\mathcal{F}(\phi)$ convolved with the LOFAR RMTF, from Van Eck et al. (2017). The narrow component, called *Faraday thin* and modelled as a Dirac delta function, is not strongly depolarized at low frequencies. The component extended in Faraday depth, significantly broader than the RMSF and modeled as top-hat function, appears as two low-intensity Faraday-thin peaks: one peak where it

sharply increases from zero to the top-hat amplitude, and the second where it decreases back to zero.

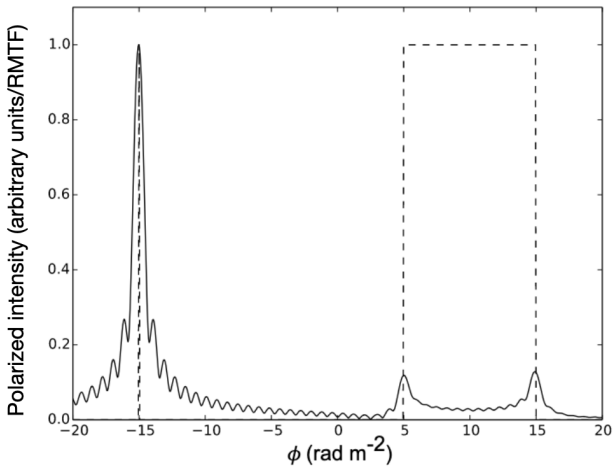

Figure 4.5: From Van Eck et al. (2017): the dashed line represents the input Faraday spectrum containing a delta function at $\phi = -15$ rad m^{-2} and a broad Faraday component between 5 and 15 rad m^{-2}, both with amplitude of 1. The solid line represents the resulting spectrum from the convolution of the input Faraday spectrum and the LOFAR RMTF. The broad Faraday component is almost completely depolarized.

LOFAR has the potential to minimize the effect of beam depolarization with observations at higher angular resolution. Van Eck et al. (2018) reported developments in polarization processing for the 570 deg^2 preliminary data release region from the LoTSS (Shimwell et al., 2017, 2019), finding 0.16 polarized radio sources per square degree at 150 MHz with resolution of 4.3′ and sensitivity of 1 mJy beam^{-1} root mean square (rms). Neld et al. (2018) developed a computationally efficient and rigorously defined algorithm to find linearly polarized sources in LOFAR data and applied it to previously calibrated data of the M51 field (Mulcahy et al., 2014); they found 0.3 polarized sources per square degree at 150 MHz, at resolution of 20″ and rms of 100 μJy beam^{-1}. O'Sullivan et al. (2019) presented the Faraday RM and depolarization properties of a giant radio galaxy using LOFAR, demonstrating the potential of LOFAR to probe the weak signature of the intergalactic magnetic field (see

also O'Sullivan et al. 2020; Stuardi et al. 2020; Mahatma et al. 2019, 2021).

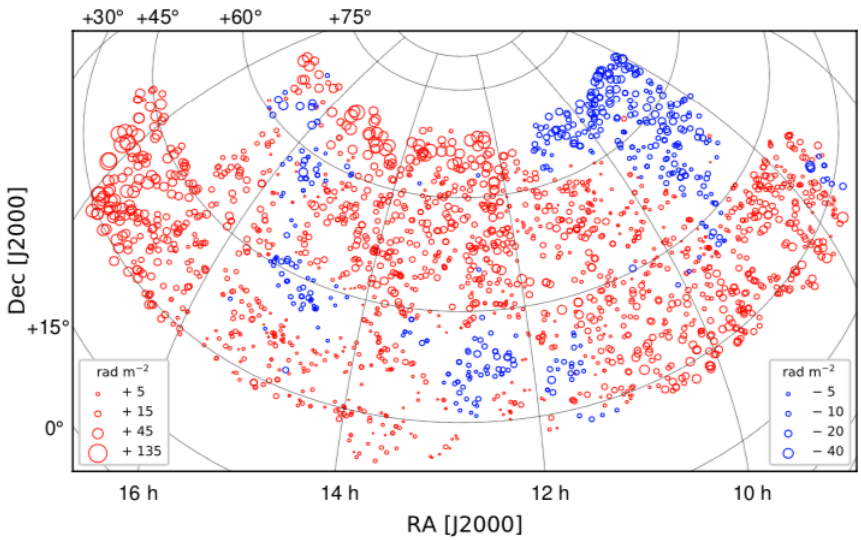

Figure 4.6: From O'Sullivan et al. (2023): Sky distribution of the polarized sources across the LoTSS-DR2 13 hr field, in equatorial coordinates and with an orthographic projection. The red/blue colored circles correspond to positive/negative RM values, and the size of the circles are proportional to the magnitude of the RM (as quantified in the figure legends). There are 2 039 sources in the 13 hr field, which corresponds to an number density of 0.48 deg^{-2}.

Herrera Ruiz et al. (2021) worked on the ELAIS-N1 field, developed a new algorithm to stack different observation epochs in polarization, finding 10 polarized sources in 16 deg^2 at resolution of 20″ in Stokes Q, U data cube.

From the LoTSS-DR2, a catalogue of more than 2 500 high precision RM values ($\sim$1 rad m^{-2}) from extragalactic polarized sources over 5 720 deg^2 was produced, for a number density of 0.43 polarized sources per square degree (O'Sullivan et al., 2023). The linear polarization and RM properties of the sources were derived from an image made at 20″-resolution. The catalog contains the host galaxy identification for 88% of the sources, along with redshifts for 79%, both photometric and spectroscopic. Fig. 4.6 shows the LoTSS DR2 RM grid.

The LoTSS-DR2 RM data were used by Carretti et al. (2022) and Carretti et al. (2023) for their studies on the magnetism in the cosmic web filaments summarized in Sect. 2.7. Fig. 4.7 shows the LoTSS-RRM DR2 grid.

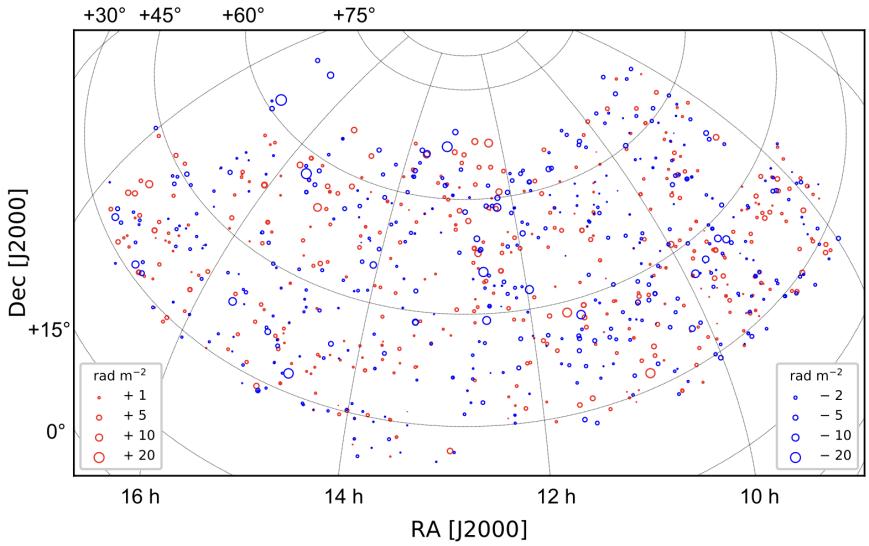

Figure 4.7: From Carretti et al. (2023): Sky distribution of the RRM across the LoTSS-DR2 13 hr field, in equatorial coordinates and with an orthographic projection. The red/blue colored circles correspond to positive/negative RM values, and the size of the circles is proportional to the magnitude of the RRM (as quantified in the figure legends).

CHAPTER 5

Polarization in the ELAIS-N1 LOFAR Deep Field

In this Chapter I introduce the ELAIS-N1 LOFAR deep field, the target of my polarization studies. I will explain the theory behind the stacking method and show the challenges of its application on the data in Sect. 5.4. In Sect. 5.5 and Sect. 5.6 I will provide information on the polarized source counts, Rotation Measure and Residual Rotation Measure of the field. Finally, in Sect. 5.7 I compare my findings with the results from LoTSS-DR2 RM.

5.1 The European Large-Area ISO Survey-North 1 (ELAIS-N1)

The ELAIS-N1 field is a a region of the Northern Hemisphere (RA = 16h10m01s, Dec = 54^o30m36s) observed by the ELAIS survey (Oliver et al., 2000), originally chosen for deep extragalactic observations with the Infrared Space Observatory (ISO) because of its low infrared background (Rowan-Robinson et al., 2004; Vaccari et al., 2005). The ELAIS-N1 field has an ample multiwavelength coverage, of which a detailed description can be found in Kondapally et al. (2021).

At radio frequencies, this region has been covered by several radio surveys such as the Westerbork Northern Sky Survey (WENSS, 325 MHz, Rengelink et al. 1997), the NRAO Very Large Array Sky Survey (NVSS, 1.4 GHz, Condon et al. 1998), and the Faint Images of the Radio Sky at Twenty Centimeters Survey (FIRST, 1.4 GHz, Becker et al. 1995; White et al. 1997). The ELAIS-N1 field has also been observed with the Giant Metrewave Radio Telescope (GMRT) at 325 MHz (Sirothia et al., 2009), at 610 MHz (Ocran et al., 2020) and with the upgraded GMRT at 300-500 MHz (Chakraborty et al., 2020). Deep field observations in total intensity with the LOw Frequency ARray (LOFAR) at 115-177 MHz have recently been examined by Sabater et al. (2021). Studies on the polarization of radio sources in ELAIS-N1 at 1.4 GHz were conducted by Taylor et al. (2007) and Grant et al. (2010). Taylor et al. (2007) imaged a region of 7.43 deg^2 to a maximum sensitivity in Stokes Q, U of 78 μJy beam^{-1}, detecting about 11 polarized sources per square degree. Grant et al. (2010) imaged a region of 15.16 deg^2, to a maximum sensitivity in Stokes Q, U of 45 μJy beam^{-1}, and detected about 9 sources per square degree. They constructed also the Euclidean-normalized polarized differential source counts down to 400 μJy and found that fainter radio sources have a higher fractional polarization than the brighter ones.

5.2 The ELAIS-N1 LOFAR Deep Field

The ELAIS-N1 LOFAR Deep Field is the deepest of the LoTSS deep fields to date (Tasse et al., 2021; Sabater et al., 2021). Over a frequency range of 114.9–177.4 MHz, it was observed for an effective observing time of 163.7 hours, reaching a root mean square noise level of $\lesssim$20 μJy beam^{-1} in the central region and below 30 μJy beam^{-1} in the internal 10 square degrees in the Stokes I image at 6″ resolution. More than 80 000 radio sources were detected in the full area of 68 deg^2. The source associations, cross-identifications, and multi-wavelength properties of the faint radio source population detected in the central $\sim$ 7.15 deg^2 were performed by Kondapally et al. (2021) for more than 31 000 sources. A photometric and spectroscopic catalog for more that 2 100 000 sources is also available Duncan et al. (2021).

Thanks to its exceptional depth and image quality, the ELAIS-N1 LOFAR deep field presents an optimal setting for diverse scientific investigations, such as the search for diffuse emissions within galaxy clusters (Osinga et al., 2021),

examination of alignment in radio galaxies (Simonte et al., 2023) and studies of the radio, optical and environmental properties of giant radio galaxies (Simonte et al., 2024). Data from this field were also used to study the spectral properties of star-forming galaxies (An et al., 2024).

The ELAIS-N1 LOFAR deep field was studied in polarization by Herrera Ruiz et al. (2021) and Šnidarić et al. (2023). Herrera Ruiz et al. (2021) combined 6 8-hours observation epochs in an area of 16 deg^2, finding about 0.6 polarized sources per square degree at a resolution of 20$''$ and reaching a sensitivity of 26 μJy beam^{-1} in the central area. Šnidarić et al. (2023) combined 20 8-hours observation epochs in an area of $\sim$36 deg^2 at 4.3$'$ resolution to detect faint component of diffuse polarized emission, not clearly visible in a single observation.

We developed and used a stacking technique to be able to detect the faintest polarized sources and improve the number density of the RM grid at 150 MHz. The method allowed us to identify 5 sources detected in one single epoch and 33 sources after stacking 19 epochs, improving our detection rate of polarized emission from 0.2 to 1.3 polarized sources per square degree.

5.3 Observations

The ELAIS-N1 LOFAR deep field was observed in the observation cycles 0, 2, and 4 (proposals LC0_019, LC2_024, and, LC4_008 respectively) from May 2013 to August 2015. The data observed in early LOFAR cycles (0 and 2) were taken jointly with the LOFAR Epoch of Reionization Key Science Project team, as a potential field for EoR studies (Jelić et al., 2014). The observing configuration of cycle 0 and 2 was different from the standard LoTSS configuration. The observations of the ELAIS-N1 field were taken with the LOFAR high band antennas with a frequency ranging from 114.9 to 177.4 MHz and phase centre of the field in RA = 16h10m01s, Dec = 54°30m36s (J2000). Table 5.1 shows the LOFAR observing configurations for the cycles we used.

Observations from cycle 2 and cycles 4 contains 22 eight-hour-long epochs. They were imaged at 6$''$-resolution in Stokes Q and U frequency cubes, covering an area of 25 deg^2. Of these, five cubes were missing some expected frequency channels. We were able to reconstruct two cubes by identifying the missing channels from the processing logs, but had to exclude three cubes from the analysis as the missing channels could not be identified. The 19

Table 5.1: LOFAR observing configurations for the ELAIS-N1 deep field and parameters of RM synthesis.

LOFAR cycle	Frequency range [MHz]	Number of frequency channels	Channel width [Hz]
2	114.979 - 177.401	800	78125.00
4	114.989 - 177.391	640	97656.25

observations and datasets used are summarized in Table 5.2.

5.4 Stacking polarization data

As discussed in the previous sections, detecting polarized emission at low radio frequencies is challenging, especially for very faint sources where the polarized signal can be close to the noise level, σ.

Stacking is a method that can improve the signal-to-noise ratio by averaging several observational epochs of the same target field.

Noise

Gaussian noise

If the noise in an epoch, $\sigma_{\rm i}$, is Gaussian, stacking N epochs leads to a final noise $\sigma_{\rm fin}$ given by:

$$\frac{1}{\sigma_{\rm fin}^2} = \sum_{\rm i}^{N} \frac{1}{\sigma_{\rm i}^2} \,. \tag{5.1}$$

If the noise has same value σ for all the epochs, the signal-to-noise ratio improves by a factor $\sqrt{N}$, allowing to reveal polarized signal not detectable before.

The distribution of the Stokes Q, U values in frequency cubes is Gaussian, as shown in Fig. 5.1 for the central region of our epoch L230779, where we do not detected polarization, and at frequency ν=114.979 MHz. The dashed line represent the Gaussian drawn with the mean and standard deviation of the distribution.

By transforming from the frequency space to the Faraday depth space via RM synthesis, we expect the noise in the Stokes $Q(\phi)$, $U(\phi)$ cubes to still

Table 5.2: LOFAR ELAIS-N1 datasets used in this work.

ID	LOFAR ID	Date	Duration	σ_{QU} (μJy beam^{-1})
009	L229064	2014-05-19	8h00m05s	88
010	L229312	2014-05-20	8h00m05s	88
012	L229673	2014-05-26	8h00m05s	77
013	L230461	2014-06-02	8h00m05s	109
014	L230779	2014-06-03	8h00m05s	73
015	L231211	2014-06-05	8h00m05s	79
016	L231505	2014-06-10	7h20m06s	78
017	L231647	2014-06-12	6h59m58s	84
018	L232981	2014-06-27	4h59m58s	95
019	L233804	2014-07-06	5h00m01s	122
020	L345624	2015-06-07	7h40m06s	82
021	L346136	2015-06-14	7h40m06s	82
022	L346154	2015-06-12	7h40m06s	96
023	L346454	2015-06-17	7h40m06s	96
024	L347030	2015-06-19	7h40m06s	81
026	L347494	2015-06-26	7h40m06s	90
028	L348512	2015-07-01	7h40m06s	104
031	L369530	2015-08-22	7h40m06s	84
032	L369548	2015-08-21	7h40m06s	88

Table 5.3: Adapted from Table 1 of Sabater et al. (2021). Columns 1 and 6: internal ID code; Cols 2 and 7: standard LOFAR ID; Cols 3 and 8: date at which the observation started; Cols 4 and 9: total duration of the observation; Cols 5 and 10: noise level in polarization in the 2.5×2.5 arcmin^2 central region of the image. The epochs above the solid line belong to Cycle 2, the epochs below to Cycle 4.

be Gaussian. Fig. 5.2 shows the histograms of Stokes Q, U values for the central region of our data, where we do not detected polarization, in the region $350 \leq |\phi| \leq 450$ rad m^{-2}, where we do not expect to find a polarized signal. The dashed lines represent the Gaussians drawn with the mean and standard deviation of the distributions.

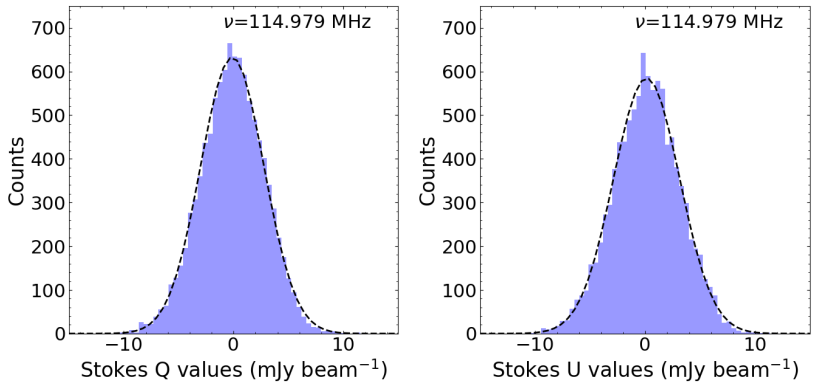

Figure 5.1: Example of histogram of the noise in the Stokes Q (left panel) and U (right panel) frequency cube of our data at frequency of 114.979 MHz, for the central region of our field of size 2.5×2.5 arcmin^2 of epoch L230779, where we do not detect a polarized signal. The dashed red lines represent the Gaussians drawn with the mean and standard deviation of the distributions. The Gaussian distributions of the Q and U values have the same mean (0.1 mJy beam^{-1}) and standard deviation (2.9 mJy beam^{-1}).

Ricean noise

Following Eq. 2.8, the polarized intensity P can be written as $P = \sqrt{Q^2 + U^2}$, and in Faraday space we can make explicit the dependence on the Faraday depth ϕ and write the Faraday spectrum $F(\phi)$ as the square root of the sum of $Q(\phi)$ and $U(\phi)$:

$$F(\phi) = \sqrt{Q^2(\phi) + U^2(\phi)}\,, \tag{5.2}$$

therefore $F(\phi)$ is described by the Ricean distribution (Kobayashi et al., 2012).

Using $\mathcal{N}$ to indicate a Gaussian distribution, if the Stokes Q, U parameters are described by $\mathcal{N}(\mu_Q, \sigma^2)$ and $\mathcal{N}(\mu_U, \sigma^2)$, respectively, with μ mean and σ^2 variance of the distributions, the complex Faraday spectrum can be written as:

$$\mathcal{F}(\mu, \sigma) = \mathcal{N}(\mu_Q, \sigma^2) + i\mathcal{N}(\mu_U, \sigma^2)\,, \tag{5.3}$$

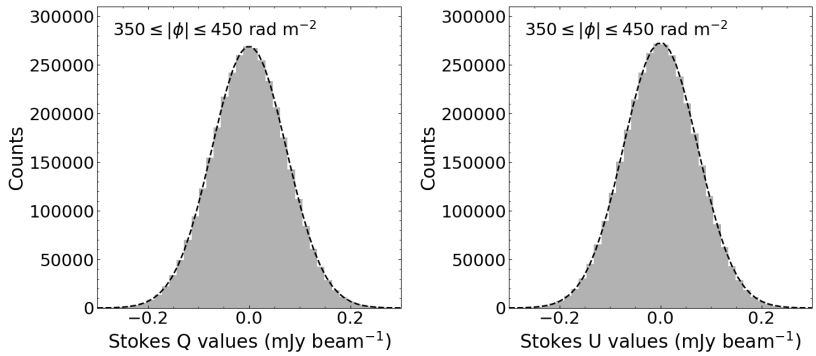

Figure 5.2: Example of histogram of the Stokes Q (left panel) and U (right panel) intensities in the range $350 \leq |\phi| \leq 450$ rad m^{-2}, where we do not expect to find a polarized signal, for the central region of our field of size 2.5×2.5 arcmin^2 with no polarized signal. The dashed black lines represent the Gaussians drawn with the mean and standard deviation of the distributions. The standard deviation is 0.07 mJy beam^{-1} in both Q and U, and the means are very close to zero (0.03×10^{-3} mJy beam^{-1} for Q and 0.03×10^{-3} mJy beam^{-1} for U).

where i is the imaginary unit. $F(\phi)$ follows a Ricean distribution, defined as:

$$f(x|\mu,\sigma) = \frac{x}{\sigma^2} e^{-\frac{x^2+\mu^2}{2\sigma^2}} I_0\left(\frac{\mu x}{\sigma^2}\right) \epsilon(x)\,, \tag{5.4}$$

where $\mu = \sqrt{\mu_Q^2 + \mu_U^2}$, $\epsilon(x)$ is unit step Heaviside function and I_0 is the 0th order modified Bessel function of the first kind:

$$I_0(y) = \frac{1}{\pi}\int_0^{\pi} e^{y\cos\psi} d\psi, \quad -\infty < x < \infty\,. \tag{5.5}$$

In Fig. 5.3 shows the histogram of the noise values of an example of Faraday cube F(ϕ). The statistics of the noise follows the Ricean distribution.

Because of the definition of F(ϕ) in Eq. 5.2, this quantity is always positive and this over-estimation is known as Ricean bias. A good estimation of the true F(ϕ), $F_{\rm true}$, was the subject of the study of George et al. (2012), that

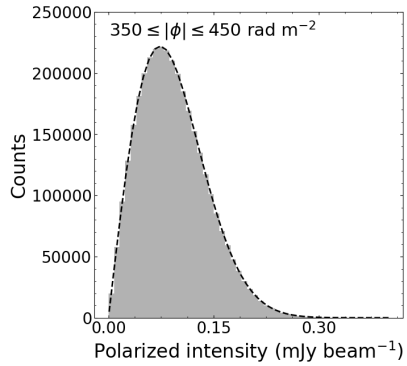

Figure 5.3: Example of histogram of values of polarized intensities, F(ϕ), in the range $350 \leq |\phi| \leq 450$ rad m^{-2}, where we do not expect to find a polarized signal, for the central region of our field of size 2.5×2.5 arcmin^2 with no polarized signal. The dashed black line represents the Ricean distribution drawn with parameters $\mu = 62$ μJy beam^{-1} and $\sigma = 74$ μJy beam^{-1}.

found, through simulations:

$$F_{\rm true} = \sqrt{F_{\rm meas}^2 - 2.3\sigma_{\rm QU}^2}\,, \tag{5.6}$$

where $F_{\rm meas}$ is the measured value of F(ϕ) and $\sigma_{\rm QU}$ is the error computed from Q(ϕ) and U(ϕ). We compute the value $\sigma_{\rm QU}$ as:

$$\sigma_{\rm QU} = \frac{\sigma_{\rm Q} + \sigma_{\rm U}}{2}\,, \tag{5.7}$$

where $\sigma_{\rm Q}$ and $\sigma_{\rm U}$ are computed as the standard deviation of $Q(\phi)$ and $U(\phi)$ from region where we do not expect to see a real signal (we note in our data the noise levels in Stokes Q and U are very similar).

The stacking method

The total electron content of plasma in the Earth's ionosphere and the geomagnetic field interact with the polarized radiation coming from the sources under examination, causing a Ionospheric Faraday rotation which results as a time- and direction-dependent propagation effect (Murray & Hargreaves, 1954;

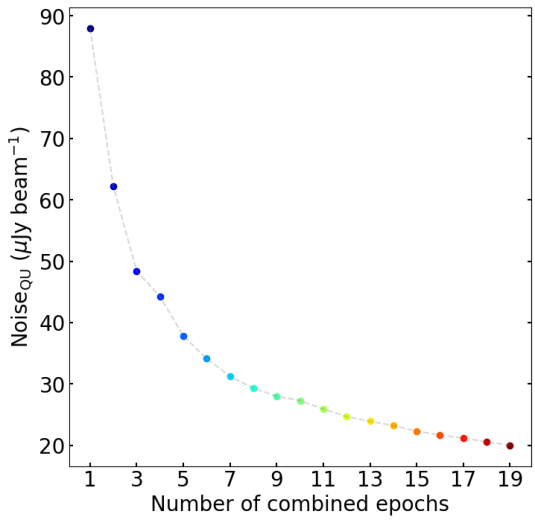

Figure 5.4: Noise levels for different numbers of stacked epochs. The noise level decreases as more epochs are combined, demonstrating the efficacy of the stacking method and highlighting the importance of combining as many epochs as possible. The noise is reduced by a factor $\sim \sqrt{N}$ after stacking N epochs, as expected from Gaussian statistics. The noise values for each epoch are extracted from Table 3 of Paper I.

Hatanaka, 1956). The LOFAR observations are usually corrected for the ionospheric Faraday rotation, but systematic uncertainties related to ionospheric Faraday rotation corrections or due the dependent calibration can strongly affect RM measurements: a wrong measure in RM of $\sim$0.8 rad m^{-2} at LOFAR observational wavelengths (150 MHz) results in a polarization vector rotated of 180°, i.e. fully depolarized. The correction for the ionospheric Faraday rotation shifts of the the total Faraday spectrum, slighlty moving the instrumental polarization peak from 0 rad m^{-2}.

Herrera Ruiz et al. (2021) showed that that possible changes in the observed polarization angle χ from different observing runs may are present. Indeed, for six studied observational epochs of ELAIS-N1, the observed Faraday depth of the brightest reference source in signal-to-noise ratio in each observation had a difference that could vary from -0.12 to 0.05 rad m^{-2}.

Therefore, a stacking method needs to take account of these changes in χ,

in order to avoid to depolarize the signals when combining the epochs and it is crucial to align the polarization angles before stacking.

The key idea is to choose a reference source in a reference epoch as calibrator, determine the polarization angle of the calibrator and the correction to apply to the polarization angle of the reference source in the epoch to be corrected in order to align it with the calibrator, and apply this difference to each polarization angle of the frequency cubes.

After the alignment, we stacked observational epochs belonging to 2 different cycles, with 2 different setup in the number of frequency channels. Fig.5.4 shows the reduction in noise levels as more epochs are combined.

Reference epoch and reference source

We can evaluate the quality of the epoch through the study of the behavior of the noise. For each epoch, we computed the noise as the standard deviation on the central region of our field, where we know there is no polarized emission, of the Stokes Q, U frequency channels. Fig. 5.5 shows the behavior of the noise for epoch 014 (Cycle 2), that we selected as reference epoch as has the lowest mean value of the noise and less spikes in the plot. The spikes correspond to flagged channels for radio-frequency interference (RFI). We chose the reference

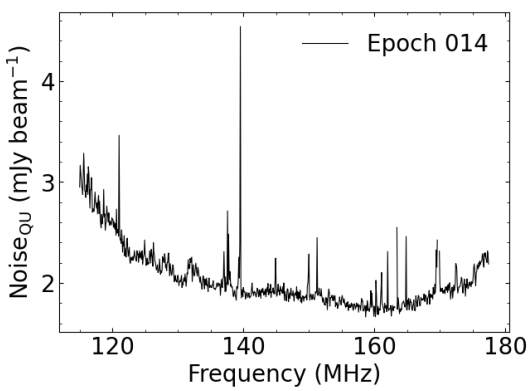

Figure 5.5: Noise level of Stokes Q and U intensity parameters for epoch 014, the reference epoch, as a function of frequency.

source used by Herrera Ruiz et al. (2021) as reference source for our work, as

it is the brightest source in signal to noise ratio closer to the center of the field.

Stacking in frequency space

We used the stacking method developed by Herrera Ruiz et al. (2021). It is based on the use of a polarized reference source in a reference epoch as polarization angle calibrator on the angles determined through the coherent addition of the signal across the full band using RM synthesis.

For each epoch we computed the polarization angle of the reference source and the relative difference with the polarization angle of the calibrator after RM synthesis, and we apply this difference to the entire Stokes Q,U frequency cubes of epoch to be corrected. This resulted into the shift of the polarization angle of the epoch to be corrected, in order to have the same vertical intercept as the reference polarization angle. Fig. 5.6 shows how the method works. The top panel shows the observed polarization angle of the calibrator as a function of the squared wavelength at the reference epoch, in black, and at the epoch to be corrected, in magenta. The slopes of the curves, i.e. the RM, are almost equal, but the vertical intercepts, i.e. χ_0, are shifted. The middle panel shows the observed polarization angle of the calibrator as a function of the squared wavelength at the epoch to be corrected, in magenta, and after the correction (i.e. derotated), in blue. The RM of the corrected epoch did not change but χ_0 was shifted. The bottom panel shows the polarization angle of the calibrator as a function of the squared wavelength at the reference epoch, in black, and at the epoch corrected, in blue. The two curves have now the same intercept.

Stacking in Faraday depth space

The stacking of Stokes Q, U frequency cubes with different number of frequency channels resulted not ideal to be done in frequency space. Herrera Ruiz et al. (2021) showed that the application of the polarization angle correction using an average angle difference across a broad range of frequencies by calculating the slope of the polarization angle as a function of λ^2 of one frequency sub-band, or even individual Q, U values per channel, causes depolarization of the signal. This is due to the channel-dependency of noise and/or artifacts, to which the polarization angle is sensitive, furthermore the shift in

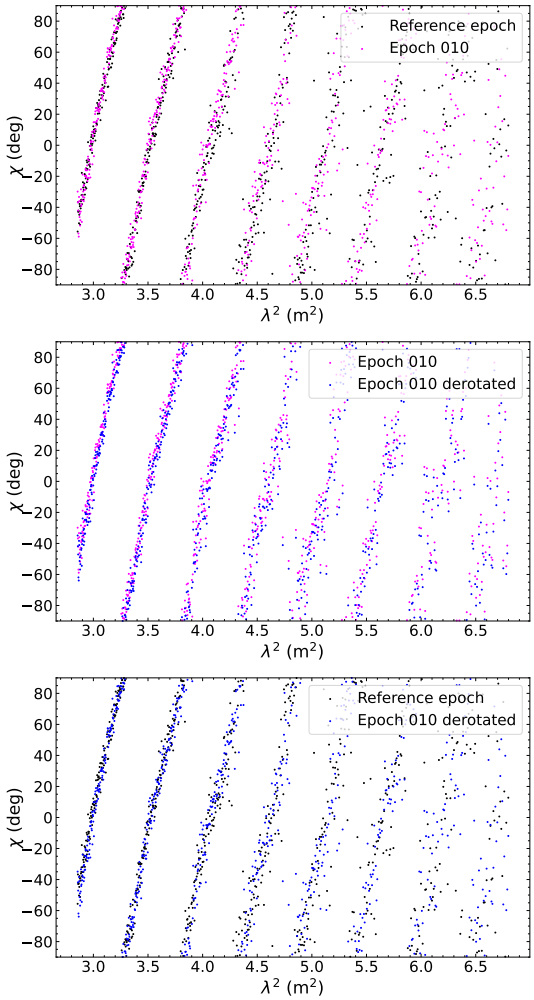

Figure 5.6: Polarization angle, in degrees, as a function of the wavelength squared, in m^2, for the reference source at the reference epoch (014), at epoch 010 and at epoch 010 after the alignment (i.e. de-rotated epoch).

the polarization angle depends on the frequency range chosen.

For these reasons we stacked epochs belonging to the same observing cycle

in frequency space, and we combined the two stacked sets of cycles in Faraday depth space. Because of the properties of the noise described in Sect. 5.4, we combined the Stokes cubes Q(ϕ) and U(ϕ) and we computed the Faraday spectrum F(ϕ) following Eq. 5.2.

Managing big data

We imaged Stokes Q, U frequency cube at $6''$ resolution for an area of 25 deg^2. The pixel size in RA-Dec is $1.5''$. For a single Stokes parameter frequency cube we have 12005×12005 pixels for each frequency channel, therefore 1.8 or 2.3×10^{11} pixels depending on whether the number of frequency channels is 640 or 800 (belonging to Cycle 4 or Cycle 2, respectively), and the relative memory size is 800 GB. Considering that for each of the 19 epochs used we made two Stokes frequency cube parameters, we needed to store almost 30.4 TB of data in our computers. The RM synthesis process can then produce several RM cubes where the size of each is almost three times the initial size of the Stokes Q, U frequency cube.

This enormous amount of data is among the problems connected to LOFAR: the management of the so-called *big data*. The analysis of LOFAR data in fact requires the use of powerful computers that can manage the calibration and analysis of large amounts of information.

The Stokes Q, U frequency cubes were processed from the uv-data by our collaboration, that provided us compressed frequency cubes of almost 50 GB each. This allowed us to save memory size in our computers; however the compression process, which "only discards the 'noise' from the floating point values without losing any significant information"[1], becomes particularly significant for us as we decrease the noise when we stack the data and that noise value, which is not important for a single epoch, becomes more evident after stacking. Also the values of the polarized intensity change. In practice, the noise and the signals that we measure after having compressed and decompressed the epochs only once, is different from those we measure after having compressed and decompressed the epochs twice. Following this reasoning, the data we analyzed are different from those produced directly by the processing of uv-data. This problem has been highlighted by our work and will probably be evaluated and solved in the future.

[1] `https://heasarc.gsfc.nasa.gov/docs/software/fitsio/compression.html`

Implementing the stacking technique

The analysis of the data was carried out on the supercomputer Vera provided by the Onsala Space Observatory, and we developed a strategy that allowed for the optimization of the processing time and the non-occurrence of RAM memory issues.

We used the programming language *Python*[2] and related modules developed and optimized for the astrophysics field. Among them, the Astropy[3] package allows the manipulation of FITS files. However, a single Stokes frequency cube cannot even be read as an entire FITS file via this package as the size of the data is too large. For this reason, in order to process and analyze our data, we worked with slices of the field for each epoch of size 12005×151 pixels (5 deg in right ascension $\times$ 3.75 arcmin in declination, size of 8.7 GB for the Stokes Q, U frequency cube), which were extracted from the entire field using the fitscopy[4] function.

Improving the stacking technique

Stacking polarized intensity data enables us to investigate the faint polarized signals from radio sources, and applying valid techniques is crucial. I want to emphasize that I have corrected only the intrinsic polarization angle, χ_0, not the RM, i.e. I aligned the intercept, but not the slope, in the plot of polarization angles as a function of squared wavelength, as shown in Fig 5.6. Herrera Ruiz et al. (2021) demonstrated the feasibility of this stacking technique, which I have applied to my data. However, this remains an emerging field, and the community is actively exploring new methodologies. Recently, a new stacking method was proposed to probe the Galactic foreground in Šnidarić et al. (2023). They stacked 20 observational epochs of ELAIS-N1 at $4'$ resolution through the cross-correlation between observations as a function of the lag in Faraday depth. This method corrects the RM values for each epoch, and the RM of successfully detected polarized sources in their final Faraday cube are consistent with those provided in Herrera Ruiz et al. (2021), further validating the approach.

An alternative approach to explore would be to use a reference source, as I have done, and correct both RM and χ_0. This could potentially reduce

[2] `https://www.python.org/`
[3] `https://www.astropy.org/`
[4] `https://heasarc.gsfc.nasa.gov/docs/software/fitsio/cexamples.html#fitscopy`

depolarization and increase the detection of polarized sources.

5.5 Polarized source counts

An introduction to the theory of source counts was given in Chap. 3 of this thesis. In Paper I we modeled and discussed the Euclidean-normalized polarized source counts in the ELAIS-N1 LOFAR deep field. We obtained the counts by convolving the source counts in Stokes I, $n(S)$, with a probability function of the fractional polarization $\mathcal{P}\left(\Pi = \frac{P}{S}\right)$:

$$n(P) = A \int_{S_0=P}^{\infty} \mathcal{P}\left(\Pi = \frac{P}{S}\right) n(S) \frac{dS}{S}\,, \tag{5.8}$$

where, in comparison to Eq. 3.13, we introduced a scaling factor A, which indicates that only a fraction of the radio sources detected in continuum have measurable polarization. The probability function $\mathcal{P}(\Pi)$ was modeled as a log-normal function:

$$\mathcal{P}(\Pi) = \frac{1}{\sqrt{2\pi\sigma^2\Pi}} \exp\left\{ \left[-\log(\Pi/\Pi_{\rm med}) \right]^2 / 2\sigma^2 \right\}, \tag{5.9}$$

where $\Pi_{\rm med}$ is the is the median fractional polarization of the distribution and σ is the scale parameter. Therefore, our model of polarized source counts

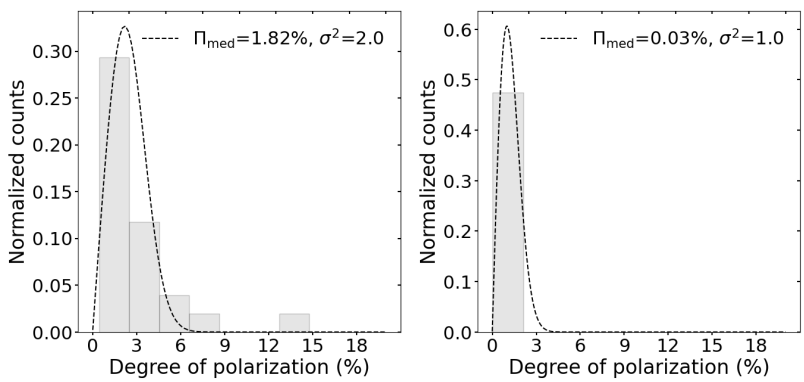

Figure 5.7: Distribution of degree of polarization of observed polarized sources (left panel), and including upper limits for the undetected polarized sources (right panel). The dashed lines show lognormal distributions with parameters in the legends. Note that for bins > 2% the values are of the order of 10^{-5} in the right panel.

have three parameters: A, $\Pi_{\rm med}$ σ. Fig. 5.7 shows the distribution of degree of polarization for the polarized sources detected, and the distribution including upper limits for undetected polarized source in the ELAIS-N1 field.

In Paper I we discussed how different combinations of parameters provide a comparable match to the data. In this section I show how our model can vary by changing the parameters.

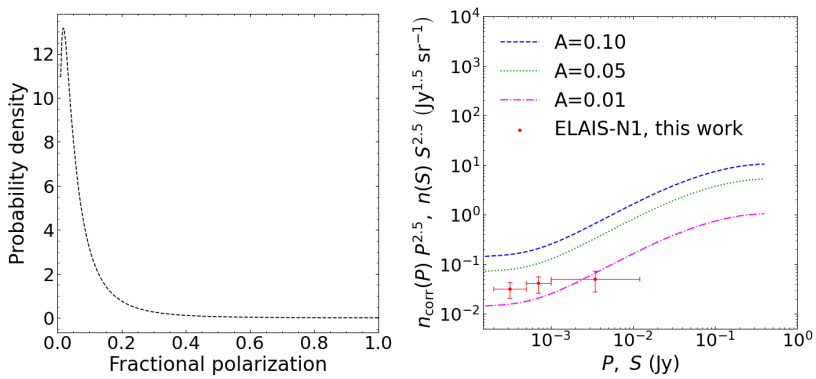

Figure 5.8: Probability distribution (left panel) and corresponding modeled polarized counts (right panels) for $\Pi_{\rm med} = 5\%$, $\sigma^2 = 1$ and varying A. The red dots represent our data and the horizontal bars indicate the widths of the bins.

Let us consider the modeled polarized counts $\Pi_{\rm med} = 5\%$, $\sigma^2 = 1$, and different values of the scaling factor A. Fig. 5.8 shows the probability distribution and the modeled polarized counts for $A = 0.10$, in blue, $A = 0.05$, in green, and $A = 0.01$, in magenta. We are not acting on the probability distribution. This factor scales the values of the counts, causing the curve to shift along the y-axis while maintaining its shape.

Now, let us consider the modeled polarized counts with $A = 0.01$, $\sigma^2 = 1$, and different values of the fractional polarization $\Pi_{\rm med}$. Fig. 5.9 shows the probability distribution and the modeled polarized counts for $\Pi_{\rm med} = 50\%$, in blue, $\Pi_{\rm med} = 5\%$, in green, and $\Pi_{\rm med} = 1\%$, in magenta. The probability distribution narrows as $\Pi_{\rm med}$ decreases, moving the peak toward the value of $\Pi_{\rm med}$. This causes the curve of the counts to move along the x-axis toward lower flux densities when $\Pi_{\rm med}$ decreases, slightly compressing the shape of the counts in total flux density.

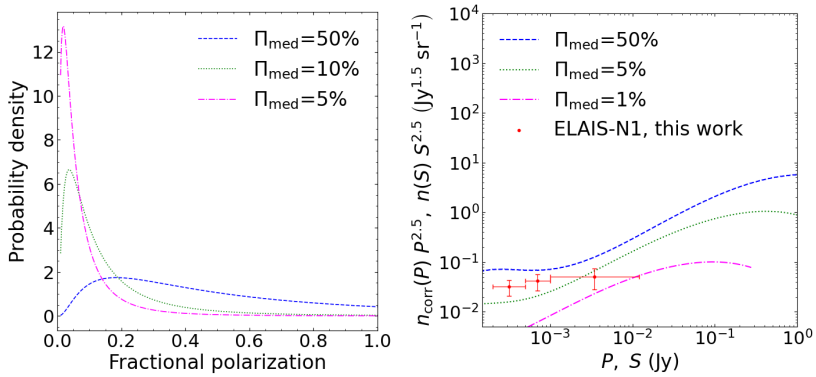

Figure 5.9: Probability distribution (left panel) and corresponding modeled polarized counts (right panels) for $A = 0.01$, $\sigma^2 = 1$ and varying $\Pi_{\rm med}$. The red dots represent our data and the horizontal bars indicate the widths of the bins.

Finally, let us consider the modeled polarized counts with $A = 0.01$, $\Pi_{\rm med} = 5\%$, and different values of the scale parameter σ^2. Fig. 5.10 shows the modeled polarized counts for $\sigma = 0.2$, in blue, $\sigma^2 = 2$, in magenta, and $\sigma^2 = 2$, in green. The value of σ influence the peak and the shape of the log-normal distribution: increasing σ, the peak of the distribution becomes lower and broader. This happens because the distribution spreads out more, causing the height of the peak to decrease. Furthermore, the right tail of the distribution becomes longer and fatter. Decreasing σ the peak of the distribution becomes higher and sharper. This is due to the concentration of values closer to the mean, making the peak more pronounced. The right tail becomes shorter and thinner. This is not intuitively reflected in the shape of the modeled counts, as we need to consider the factor $1/S$. However, it is notable that the curve becomes broader with increasing σ.

To assess whether the fractional polarization distributions used in modeling source counts are reasonable, one could compare the observed degree of polarization distribution with the assumed models (as done in Fig. 5.7) and evaluate whether these distributions are valid or should be excluded from the fitting. However, the situation is more complex. For the dotted curve of Fig. 9 in Paper I, we varied the A parameter, and for both the dashed and dotted curves, we accounted for the estimated missing sources, discussed in Sect. 6.2

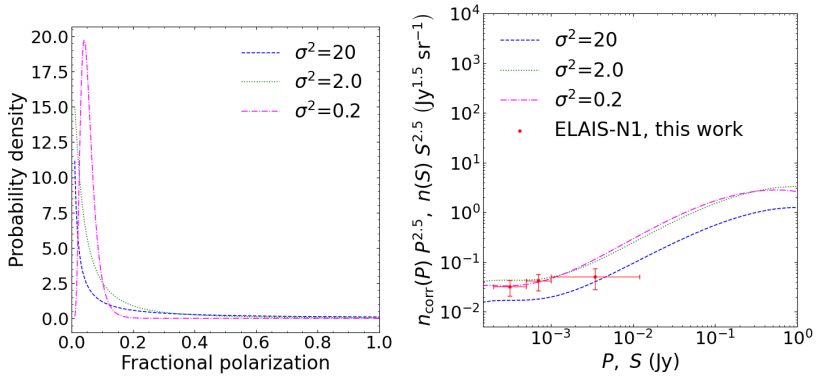

Figure 5.10: Probability distribution (left panel) and corresponding modeled polarized counts (right panels) with $A = 0.01$, $\Pi_{\rm med} = 5\%$ and varying σ^2. The red dots represent our data and the horizontal bars indicate the widths of the bins.

of Paper I. While we estimated the polarized flux density for these missing sources, no specific assumptions were made about their fractional polarization distribution. This makes it challenging to directly compare the distributions used to illustrate the degeneracies in the model to our data.

Moreover, the distribution from Mandal et al. (2021) includes sources from three deep fields, not just ELAIS-N1, and detailed information on the fractional polarization distribution for those fields is lacking. Nonetheless, it is reasonable to assume that this distribution follows a lognormal with a low median degree of polarization. Given these complexities, we adjusted the parameters of the distribution in Fig. 9 Paper I directly comparing with our data displayed in the figure itself. This led to a derived degree of polarization of approximately 5% with $\sigma^2 = 2$ for the dotted line, and 0.03% with $\sigma^2 = 1$ for the dashed line.

I showed that by varying the parameters, we can find multiple values that could represent our data. To better constrain the parameter space, we can see that it is crucial to detect more polarized sources, by studying a larger field and/or by taking deeper measurements.

Comparisons with previous work at 1.4 GHz

Here, I present the comparison between the cumulative polarized source count derived from the ELAIS-N1 field in my work and the counts from Grant et al. (2010) and Berger et al. (2021). The results in Grant et al. (2010) are particularly important to us because they derived the counts for the ELAIS-N1 field from deep polarization imaging at 1.4 GHz with the Dominion Radio Astrophysical Observatory (DRAO), identifying 136 polarized sources (9 per square degree). The observations covered an area of 15.16 deg^2 at a resolution of $42'' \times 62''$ at the field center, and reaches a sensitivity of 45 μJy beam^{-1} in Stokes Q and U. They provided counts corrected for the effective area. Therefore, to compare the cumulative counts, we assumed a uniform noise in the image and estimated the counts normalized by the area accordingly.

Berger et al. (2021) investigated the faint polarized radio source population in the Lockman Hole, using the Westerbork Synthesis Radio Telescope at 1.4 GHz, identifying 150 polarized sources (23 per square degree). Their observations achieved a noise level of 7 μJy beam^{-1} in polarized intensity, at a resolution of $15''$, and covering an area of 6.5 deg^2. They provided a comparison with polarized source counts from the literature, and they reported the effective number of sources per steradian, corrected for the effective area of the mosaic at the given flux levels.

Our poor statistics (we detect "only" 25 polarized sources against more than 100 from the considered studies at 1.4 GHz) may play an important role in all the following considerations.

The cumulative polarized counts from these two works in literature and our work are shown in Fig. 5.11.

In general, the most noticeable difference among counts is the significantly higher number of polarized sources detected at 1.4 GHz compared to those detected at 150 MHz. Grant et al. (2010) reported a polarized source density that is almost 10 times higher than what we observe at 150 MHz and Berger et al. (2021) even nearly twenty times higher. This result is expected, as detecting polarized sources at 150 MHz is much more challenging due to the strong depolarization effects caused by Faraday rotation, stronger at lower frequencies. In fact, in Paper I we found that only eight out 136 polarized sources in ELAIS-N1, with detected polarization coinciding within $6''$, were polarized in both LOFAR and DRAO images. All of these sources exhibited significant depolarization at low frequencies.

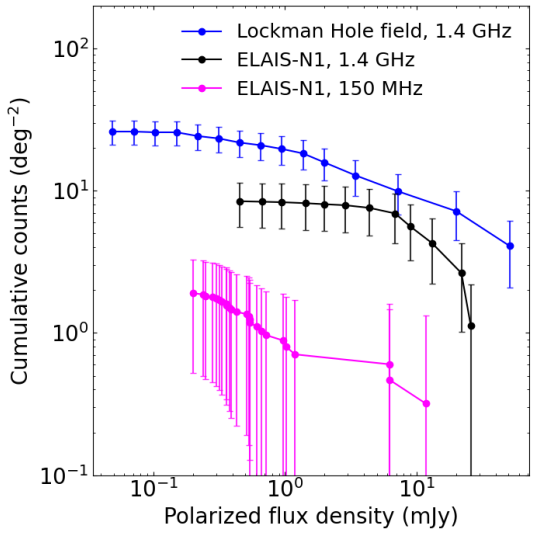

Figure 5.11: Cumulative counts of polarized sources in the Lockman Hole field at 1.4 GHz (in blue, from Berger et al. 2021), and in the ELAIS-N1 field at 1.4 GHz (in black, from Grant et al. 2010) and at 150 MHz (in magenta, from Paper I). The uncertainty is computed as the square root of the cumulative count.

Interestingly, we observe in general lower values of polarized flux densities in the ELAIS-N1 field compared to the Lockman Hole at 1.4 GHz. Indeed, the ELAIS fields were selected for their low 100 μm intensity and high galactic latitude (Oliver et al., 2000). This field selection could introduce biases in the detected source distributions, making them unrepresentative when compared to a statistically 'typical' region of the sky. Therefore, the absence of strong polarized sources in our observations is likely due to a combination of increased depolarization at lower frequencies and/or cosmic variance, as we are considering relatively small fields in both cases.

Berger et al. (2021) achieved at 1.4 GHz a higher sensitivity (six times lower noise than ELAIS-N1 at 1.4 GHz and three times lower noise than ELAIS-N1 at 150 MHz), allowing them to detect fainter polarized sources in absolute terms (the LOFAR 150 MHz observations are more sensitive if one takes into account the steepness of the source spectral indices). Berger et al. (2021)

compared their counts with counts in other deep fields: the Chandra Deep Field-South (CDF-S) and the ELAIS-South 1 (ELAIS-S1) from Hales et al. (2014a), and the Great Observatories Origins Deep Survey-North (GOODS-N) from Rudnick & Owen (2014). They found slight differences in polarized source density between the different fields, that they attributed to differences in source characteristics of different deep fields. It is reasonable to assume that similar factors apply to our field as well. Furthermore, they compared their analysis to the previous publications, especially with the simulations of O'Sullivan et al. (2008) (who used semi-empirical simulations from the European SKA Design Study (SKADS), and using the luminosity they distinguished between FR I and FR II sources) and Hales et al. (2014a) (who used the model for total-intensity source counts from Hopkins et al. (2003) and convolved it with a polarized density function fitted to their data of ELAIS-S1 and CDF-S). It is important to note that most of the sources of the Lockman Hole are unresolved, so they classified them using the radio brightness; because of this, they use "strong" (which point to FR II) and "weak" (which point to FR I) sources. They found lower source counts compared to the simulations of O'Sullivan et al. (2008) and Hales et al. (2014a), i.e. a dearth of faint sources (i.e. FR I) in their sample. Berger et al. (2021) attributed this to sample variance caused by large-scale structures within different small on-sky areas that causes different source populations to be observed within the various fields.

At 150 MHz, we also find a majority of FR II radio sources by morphological classification. In our work and in O'Sullivan et al. (2023), FR I radio galaxies are more commonly found in galaxy clusters, where strong Faraday depolarization occurs. This makes it difficult to detect polarized sources embedded in or behind these environments at 150 MHz. Additionally, the brightest and most polarized regions of FR II radio galaxies are typically located at the extremities of the source, often extending beyond the host galaxy's environment. These regions experience less depolarization due to their location. The compact nature of FR II hotspots also results in less variation in RM across the emission region, reducing depolarization.

While samples of sources observed at GHz frequencies allow for dividing sources into FR I and FR II types to study their evolution in the counts, our statistics (with only three bins) are too limited for such analysis. This highlights the crucial need to increase the number of polarized sources detected

at low frequencies.

5.6 Rotation Measure and Residual Rotation Measure grids

In Sect. 2.7 I introduced the RM grid, a valuable method for studying magnetism in different astrophysical environments, including the Milky Way (e.g. Hutschenreuter et al. 2022), radio galaxies (e.g. O'Sullivan et al. 2020), clusters of galaxies (e.g. Anderson et al. 2021), and the cosmic web (e.g. Carretti et al. 2022). The observed RM, $\mathrm{RM_{obs}}$, is the sum of contributions from all magneto-ionized media along the line of sight, and is also affected by measurement errors, $\mathrm{RM_{noise}}$. After correction for the ionospheric contribution, $\mathrm{RM_{ion}}$, we obtain the rotation measure

$$\mathrm{RM} = \mathrm{RM_{obs}} - \mathrm{RM_{ion}}\,. \tag{5.10}$$

Fig. 5.12 shows the Faraday rotation measure grid of the ELAIS-N1 LOFAR deep field produced in my work. This represents the densest RM grid so far produced at low radio frequencies, namely almost three times the number density found by O'Sullivan et al. (2023) in the LoTSS-DR2 at 20″ resolution.

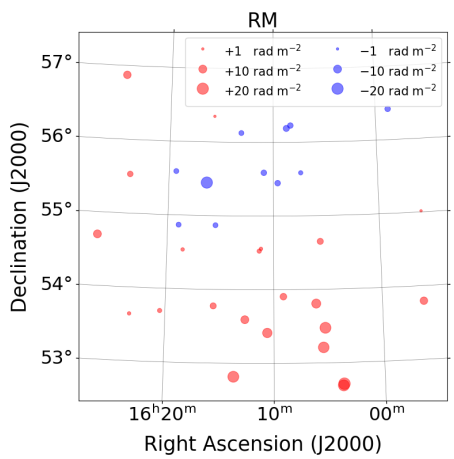

Figure 5.12: RM grid derived in our work on the ELAIS-N1 LOFAR deep field. By stacking 19 epochs at 6 arcsec resolution, I found 1.3 polarized sources per square degree.

From the RM values, the extragalactic RM, so-called Residual Rotation Measure (RRM), is calculated by subtracting the Galactic RM component:

$$\mathrm{RRM} = \mathrm{RM} - \mathrm{GRM} + \mathrm{RM}_{\mathrm{noise}}\,, \tag{5.11}$$

where GRM represents an estimate of the Galactic RM. As explained in Sect. 2.7, considering that Galactic components exhibit correlated RM values on large angular scales, while extragalactic emission is expected to be uncorrelated on scales of arcminutes or larger, Hutschenreuter et al. (2022) reconstructed the Galactic Faraday map, which I used to compute the RRM values. The data used to infer the map included the LoTSS-DR2 RM dataset; therefore, the GRM at the exact source position might be slightly biased towards the source RM, as also noted by Carretti et al. (2022). Fig. 5.13 shows the RRM grid of the ELAIS-N1 LOFAR deep field produced in my work.

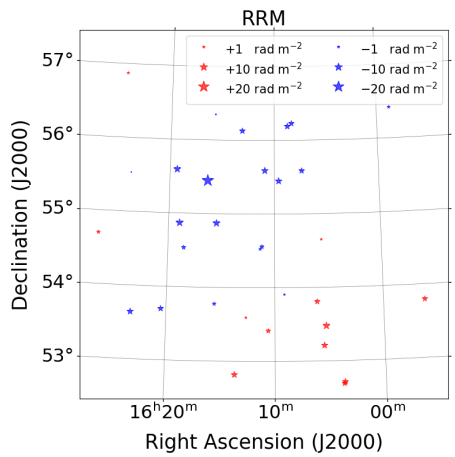

Figure 5.13: RRM grid derived in our work on the ELAIS-N1 LOFAR deep field.

5.7 LOFAR ELAIS-N1 Deep Field and Sky Survey comparison

The LoTSS-DR2 RM and ELAIS-N1 LOFAR deep field can offer complementary insights due to the differences in their observational strategies. LoTSS-

DR2 is a wide-area survey that covers a significant portion of the northern sky but at relatively high sensitivity (~ 80 μJy beam^{-1}). It predominantly detects bright polarized sources and provides important data for mapping the Galactic and extragalactic RM over large scales. The ELAIS-N1 LOFAR deep field focuses on a much smaller area of the sky (0.44% of the LoTSS-DR2 RM catalog coverage) but with significantly longer integration times (almost 20 times longer), enabling the detection of fainter polarized sources. The ELAIS-N1 LOFAR deep field is also imaged at higher resolution ($6''$ instead of $20''$) which should help reduce the beam depolarization and increase the source detection rate.

In Paper II, we found that in the ELAIS-N1 field, approximately half of the sources exhibit morphological features consistent with FR II radio galaxies, while the remaining half comprises FR I-type radio galaxies, compact sources, and diffuse sources. In terms of FR I and FR II, these proportions align with the findings from the LoTSS-DR2 RM catalog.

Additionally, we observed that the ELAIS-N1 detections have a higher median redshift compared to the LoTSS-DR2 RM catalog. To determine whether the difference in median redshift between our population and that of the LoTSS-DR2 RM catalog is statistically significant, I conducted a Kolmogorov-Smirnov (K-S) test. This test evaluates the distributions of the two samples by comparing features such as spread, shape, and, crucially, the median. The K-S test assesses the cumulative distribution functions (CDFs) of both samples, measuring the maximum difference between them. I calculated the p-value, which indicates the probability that the observed difference is due to random chance, assuming no real correlation between the two variables. A lower p-value suggests that the difference observed is less likely to be random; in our case, the K-S test yielded a p-value of 0.7. This result implies that the difference in median redshift between the two populations is not statistically significant.

Although I cannot conclude that the statistical properties of the source populations in ELAIS-N1 differ significantly from those in LoTSS-DR2 RM catalog, our deeper analysis allowed us to detect nearly three times more polarized components. This denser RM grid enhances our capacity to investigate how cosmic magnetic fields vary across the field, providing a better understanding of their structures and implications for astrophysical processes.

CHAPTER 6

Depolarization study of the reference source

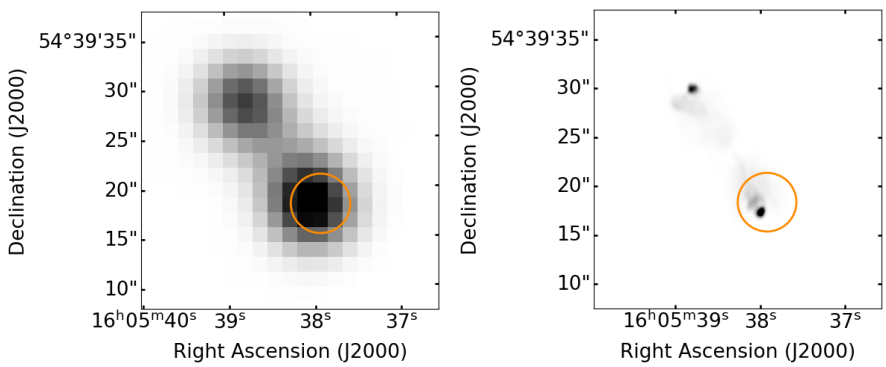

Figure 6.1: LOFAR image of source 07 at resolution of 6″ (left panel, from Sabater et al. 2021) and at 0.3″ (right panel, adapted from de Jong et al. (2024). The orange circle represents the 6″-resolution beam at the location of the polarized detection.

The depolarization of polarized signals is related to the properties of magnetic fields and of polarized emission along a line of sight. The *qu*-fitting

method, which fits depolarization models to the fractional Stokes parameters $q = Q/I$ and $u = U/I$ as a function of λ^2 (or frequency), has proven to be more effective than RM synthesis in detecting multiple Faraday components (Farnsworth et al., 2011; O'Sullivan et al., 2012; Sun et al., 2015). This technique was applied to LOFAR data of the giant radio galaxy NGC 6251 at 150 MHz and 40″-resolution by Cantwell et al. (2020), who used the code of Sun et al. (2015) (a Bayesian approach and the Multi-Nest algorithm of Feroz & Hobson 2008; Feroz et al. 2009, 2019) to converge on solutions. Their data suffered from strong instrumental polarization near Faraday depth of zero (about 2.5 times stronger than the polarized signal from the radio galaxy). They attempted to model the instrumental polarization as a first-order polynomial as a function of the frequency, but this didn't give satisfactory results, probably due to the ionospheric calibration that causes the instrumental polarization to deviate from zero by different amounts as a function of time. Cantwell et al. (2020) did not study the depolarization and used only models of Faraday-thin screens (that is, only Faraday-rotating and not synchrotron emitting).

In this section, I analyze the depolarization properties of the reference source (source 07 in Paper I), as it has the highest signal-to-noise ratio. This source, at redshift 0.7911, is an FR II radio galaxy, where we detected polarization in the southern lobe. The right panel of Fig 6.1 shows the 150 MHz morphology of this source at 0.3″ resolution, as revealed using the LOFAR international baseline data (de Jong et al., 2024), in comparison to the 6″ resolution total intensity image shown in the left panel, from the data I analyzed.

6.1 The data

In Paper I the Stokes Q, U frequency cubes from Cycle 2 and Cycle 4 were stacked separately; RM cubes were produced for each cycle and were then combined in Faraday space. For the study presented in this section, I selected the Stokes Q, U frequency cubes from Cycle 2, because these data are less affected by radio frequency interference than in Cycle 4, have lower noise values, and have more frequency channels. The effective number of frequency channels is 651 for each Stokes Q, U parameter, as a total of 149 channels out of 800 were flagged during the imaging of the data from different epochs. The central frequency was 146 MHz and the frequency range was 114.9–177.4 MHz.

The dataset was obtained by stacking ten observing epochs and has an rms of about 1 mJy beam^{-1} per frequency channel. The polarization characteristics of the source, i.e. the Stokes Q and U intensities, polarized intensity P and polarization angle χ are shown as a function of frequency and wavelength squared (λ^2) in Fig. 3 of Paper I.

There is no corresponding Stokes I frequency cube, but three images were produced in "extended bands" by Sabater et al. (2021). Table 6.1 shows the central frequencies of the extended band images and the intensities of source 07 in each image.

Table 6.1: Intensity values at the pixel of peak polarization in source 07 in the three extended bands.

ν (MHz)	127.63	149.12	167.67
I_ν (mJy beam^{-1})	726.90	709.15	682.02

I used those Stokes I images to compute the intra-band spectral index, α, through a linear fit of $\log I_\nu = \alpha \log \nu + const$, where I_ν and ν are the total intensity and frequency, respectively, from the three extended band images of Cycle 2. I assigned a 10% uncertainty to the intensities. The derived best-fit value for the spectral index was:

$$\alpha = -0.23 \pm 0.52\,.$$

The measurements and the best fit are shown in Fig. 6.2.

Then I used the best-fit parameters of the power law to construct an array with values of I_ν at the same frequency channels as for the Stokes Q and U arrays. The precision of LOFAR in measuring intra-band spectral indices is limited by the uncertainties in the flux density scale calibration (e.g., Sabater et al. 2021; Shimwell et al. 2022). Consequently, the derived α primarily reflects the observed variations across the band rather than the physical spectral index of the source. However, this is a step in removing effects from variations across the band on the Q/I and U/I ratios that are used to model the depolarization.

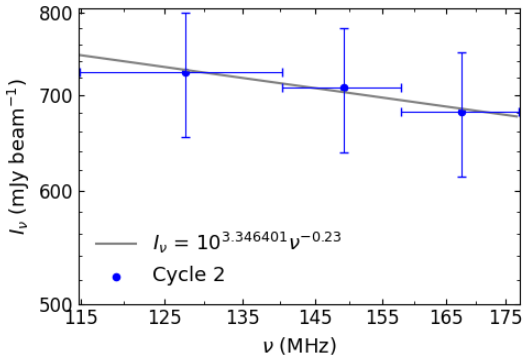

Figure 6.2: Measurements and best fit to the intensities in the three extended band images for source 07. The horizontal bars indicate the width of each band. The vertical bars are the associated 10% uncertainties on the measurements.

Uncertainties

In the frequency spectra, the uncertainties on the Stokes parameter I, δI, were computed as 10% of each I value for each channel.

The uncertainties on the Stokes parameters Q and U, δQ and δU, for each frequency channel were assigned by computing the rms noise from a small, source-free area close to the source position in each channel map.

Faraday spectrum of source 07 in Cycle 2

Fig. 6.3 shows the Faraday spectrum of the source from Cycle 2. The information from this spectrum will be used as priors in the qu-modeling. In that cycle, the reference source has a signal-to-noise ratio above 100, and the peak of the instrumental polarization ($\sim$0.8 mJy beam^{-1}) is about 10% of the polarized intensity peak ($\sim$6 mJy beam^{-1}). The values of RM and fractional polarization for source 07 in Cycle 2 are given in Table 6.2; they are in agreement with what found in the final Cycle 2+Cycle 4 dataset.

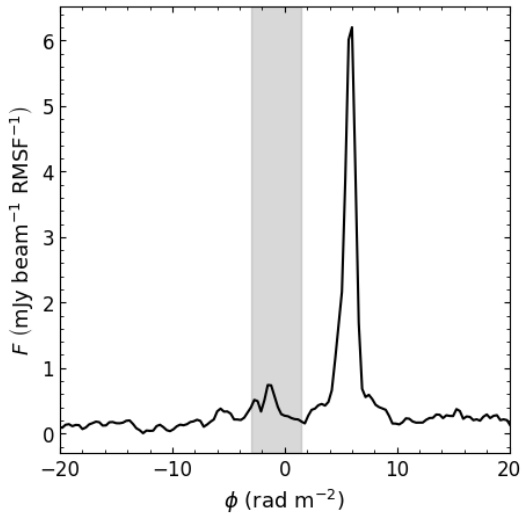

Figure 6.3: Faraday spectrum of the source 07, the reference source, from Cycle 2, computed following the methods described in Paper I. The gray region outlines the range in Faraday depths susceptible to instrumental polarization.

Table 6.2: Properties of source 07 in Cycle 2 data derived from the Faraday spectrum. Columns (1) and (2): Right ascension and declination of polarized source. Column (3): Peak polarized intensity of the source. Column (4): RM and RM error of polarized source. Column (5): Degree of polarization. The values are consistent with what found in the Cycle 2+Cycle 4 data.

RA(J2000) (deg)	Dec(J2000) (deg)	$P_{\rm p}$ (mJy beam^{-1})	RM (rad m^{-2})	Π (%)
241.4080	54.6551	6.39	6.03±0.01	1.80

6.2 The method

The models

LOFAR polarization measurements are affected by instrumental polarization that appears as a component near Faraday depth 0 rad m^{-2} in the Faraday

Table 6.3: Summary of the models used in the *qu*-fitting.

Model	Description	Equations
1ED	External Faraday dispersion	6.2
1T+1ED	Faraday thin + 1 External Faraday dispersion	6.1+6.2
1T+2ED	Faraday thin + 2 External Faraday dispersion	6.1+6.2+6.2
1Tk+1ED	Faraday thick + 1 External Faraday dispersion	6.3+6.2
1Tk+2ED	Faraday thick + 2 External Faraday dispersion	6.3+6.2+6.2

spectrum (as shown in Fig. 6.3 for our source of interest). This needs to be taken into account in the modeling. I do this by introducing a component in the region of -3 to 1.5 rad m^{-2} that is either Faraday-thin or a Burn slab (i.e. a top-hat Faraday-thick component). Indeed, the instrumental polarization can be spread over a range of RM values as it is created by RM variations in the ionosphere during an observation and/or by stacking.

As for detection of a real polarization, in LOFAR HBA observations we are sensitive only to Faraday-thin components, as structures thicker than $\approx$1 rad m^{-2} would be filtered out.

I combined different models to fit the observed q and u values of the selected source. I considered, in addition to the Faraday-thin (T) and Faraday-thick (Tk) components mentioned above, an external Faraday dispersion (ED) model. Those three models are described by:

$$p_{\mathrm{T}}(\lambda^2; p_0, \chi_0, \mathrm{RM}) = p_0\, e^{2i(\chi_0 + \mathrm{RM}\lambda^2)}\,, \tag{6.1}$$

$$p_{\mathrm{ED}}(\lambda^2; p_0, \chi_0, \mathrm{RM}, \sigma_{\mathrm{RM}}) = p_0\, e^{2i(\chi_0 + \mathrm{RM}\lambda^2)} e^{-2\sigma_{\mathrm{RM}}^2 \lambda^4}\,, \tag{6.2}$$

$$p_{\mathrm{Tk}}(\lambda^2; p_0, \chi_0, R) = p_0\, e^{2i\left(\chi_0 + \frac{1}{2}R\lambda^2\right)}\, \frac{\sin R\lambda^2}{R\lambda^2}\,, \tag{6.3}$$

where λ^2 is the variable and $(p_0, \chi_0, \mathrm{RM}, \sigma_{\mathrm{RM}}, R)$ are the parameters. I combined these models in the five models that are listed in Table 6.3.

Priors

The *qu*-fitting (described after this paragraph) requires priors on the model parameters. The choice of some priors was done by considering the Faraday spectrum of the source, shown in Fig. 6.3.

- The sum of p_0, for combined models, must be smaller than 1, and each angle χ_0 must have a value between 0° and 180° for all models.
- For model 1ED, the value of RM is constrained in the range 3–10 rad m^{-2}, as we observe the main peak at ~ 6 rad m^{-2} in the Faraday spectrum (Fig. 6.3).
- For models with 2ED, one RM component is constrained in the range from 3–10 rad m^{-2} and the other in the range from -100 to 100 rad m^{-2}.
- As the value of RM for instrumental polarization is expected to be in the range from -3 to 1.5 rad m^{-2} (Fig. 6.3), I used this constraint for the model where the leakage is represented as Faraday-thin component, and in the range from -6 to 3 rad m^{-2} if represented as pseudo-Faraday thick, as RM $= \frac{1}{2}R$.
- The value of $\sigma_{\rm RM}$ is forced to be positive and smaller than 1 rad m^{-2} to be detectable with LOFAR, as shown in Fig. 4.3.

qu-fitting

I performed the 1D *qu*-fitting at the pixel of the polarization detection (given in Table 6.2) using the RM-TOOLS[1] (Purcell et al., 2020), which utilizes the MultiNest algorithm (Feroz & Hobson, 2008; Feroz et al., 2009, 2019) implemented as `PYMULTINEST` (Buchner et al., 2014), to explore the parameter space, find the best fit, and estimate the uncertainties in the fitted parameters. The algorithm returns the posterior distribution for the model parameter, and the *Bayesian evidence* $\mathcal{Z}$ of the model, providing the capability to assess various goodness-of-fit metrics. This represents the probability of the observed data given a specific model. To select between two models, a and b, it is common to consider the Bayes odds ratio ($\Delta\ln\mathcal{Z}$):

$$\Delta \ln \mathcal{Z} = \ln \mathcal{Z}_a - \ln \mathcal{Z}_b = \ln \frac{\mathcal{Z}_a}{\mathcal{Z}_b}\,, \tag{6.4}$$

where $\mathcal{Z}_a$ and $\mathcal{Z}_b$ are the Bayesian evidences of models a and b, respectively. Following Kass & Raftery (1995), we evaluate the evidences based on the derived value $2\Delta \ln \mathcal{Z}$: for values of 0–2, the evidence of model a over b is "not

[1] `https://github.com/CIRADA-Tools/RM-Tools/wiki/QUfitting`

worth more than a bare mention", for 2–6 the evidence is positive, for 6–10 the evidence is strong, and for > 10 the evidence of a over b is very strong. If values are negatives, we consider the absolute values and it functions similarly but applies to the b model. Computing the odds ratio between the model with the highest evidence and all other models, the model with the lowest Bayesian odds ratio value represents the best-fitting model. The fitting software requires as input parameters a list of frequencies, the corresponding Stokes parameters I, Q and U, and their associated errors.

In addition to the Bayesian odds ratio, the software calculates, for each model, the reduced chi-square χ^2_{red}:

$$\chi^2_{\mathrm{red}} = \frac{1}{\mathrm{DoF}} \left[\Sigma_{i=1}^{N} \left(\frac{q_i - q_{\mathrm{model},i}}{\delta q_i} \right)^2 + \Sigma_{i=1}^{N} \left(\frac{u_i - u_{\mathrm{model},i}}{\delta u_i} \right)^2 \right], \tag{6.5}$$

where DoF is the number of degrees of freedom, N is the number of data points (i.e. the effective number of frequency channels), q_{model} and u_{model} are the model's values, δq and δu are the uncertainties on q and u.

6.3 Results

Table 6.4: Summary of the best-fitting metrics for each model used in qu-fitting. Column (1): The model's name. Column (2): The number of free parameters, $\mathrm{N_{free}}$. Column (3): The number of components, $\mathrm{N_{comp}}$. Column (4): The number of degree of freedom, DoF. Column(5): The logarithm of the evidence, $\ln \mathcal{Z}$. Column (6): The odd ratio, $2\Delta \ln \mathcal{Z}$. The rows are sorted by the odd ration values.

Model	$\mathrm{N_{free}}$	$\mathrm{N_{comp}}$	DoF	χ^2_{red}	$\ln(\mathcal{Z})$	$2\Delta \ln(\mathcal{Z})$
1T+2ED	11	3	1290	2.7	5331	0
1Tk+2ED	11	3	1290	3.7	4755	1152
1T+1ED	7	2	1294	3.9	4637	1388
1Tk+1ED	7	2	1294	4.4	4337	2208
1ED	4	1	1297	4.9	3990	2682

The summary of the best-fitting metrics,with rows sorted by the $2\Delta \ln \mathcal{Z}$ value, is shown in Table 6.4. Table 6.5 lists the best-fitting parameters of the models.

Table 6.5: Best-fitting parameters.

Model	$p_{0,(1,2,3)}$ (%)	$RM_{(1,2,3)}$ (rad m^{-2})	$\sigma_{RM,(1,2,3)}$ (rad m^{-2})	R (rad m^{-2})	$\chi_{0,(1,2,3)}$ (deg)
1T+2ED	$0.18^{+0.04}_{-0.04}$,	$-1.15^{+0.01}_{-0.01}$,	–	–	105^{+3}_{-3},
	$2.54^{+0.04}_{-0.04}$,	$5.972^{+0.003}_{-0.003}$,	$0.143^{+0.001}_{-0.001}$,	–	59^{+1}_{-1},
	15^{+3}_{-4}	$5.94^{+0.01}_{-0.03}$	$0.377^{+0.002}_{-0.002}$	–	173^{+3}_{-2}
1Tk+2ED	$0.49^{+0.02}_{-0.01}$,	–	–	$-0.71^{+0.01}_{-0.01}$,	125^{+1}_{-1},
	$3.79^{+0.07}_{-0.05}$,	$5.910^{+0.002}_{-0.004}$,	$0.168^{+0.001}_{-0.001}$,	–	63^{+1}_{-1},
	25^{+2}_{-3}	$6.09^{+0.06}_{-0.07}$	$0.44^{+0.01}_{-0.01}$	–	65^{+11}_{-9}
1T+1ED	$0.17^{+0.01}_{-0.01}$,	$-1.09^{+0.01}_{-0.02}$,	–	–	87^{+4}_{-4},
	$4.54^{+0.04}_{-0.04}$	$5.817^{+0.004}_{-0.004}$	$0.181^{+0.001}_{-0.001}$	–	$81.2^{+0.4}_{-0.5}$
1Tk+1ED	$0.49^{+0.02}_{-0.02}$,	–	–	$-0.66^{+0.01}_{-0.01}$	113^{+2}_{-2},
	$4.52^{+0.4}_{-0.4}$	$5.847^{+0.002}_{-0.002}$	$0.181^{+0.001}_{-0.001}$	–	79^{+1}_{-1}
1ED	$4.41^{+0.4}_{-0.4}$	$5.845^{+0.002}_{-0.002}$	$0.179^{+0.001}_{-0.001}$	–	$79.9^{+0.5}_{-0.5}$

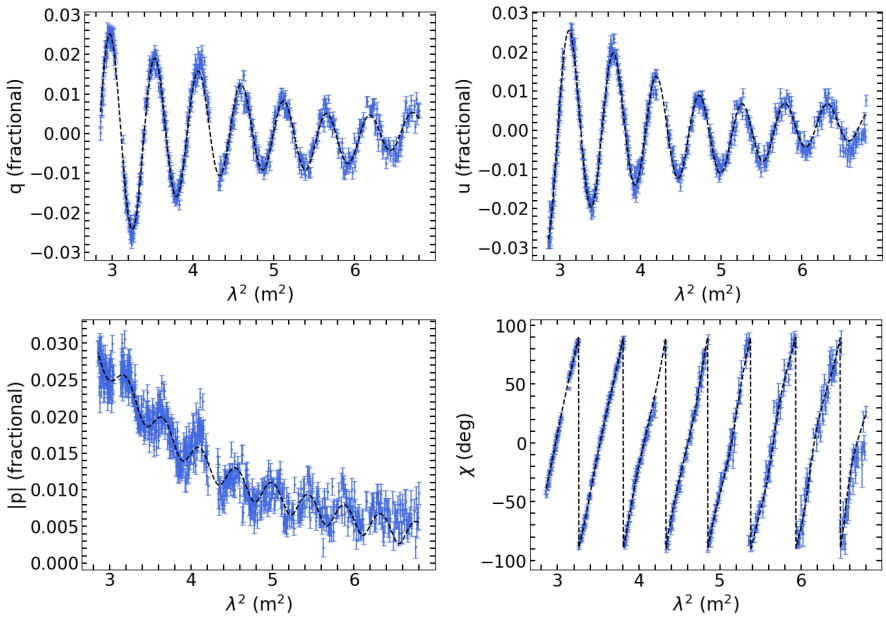

Figure 6.4: Polarization data for source 07, and the corresponding best-fitting model 1T+2ED overplotted (black dashed line).

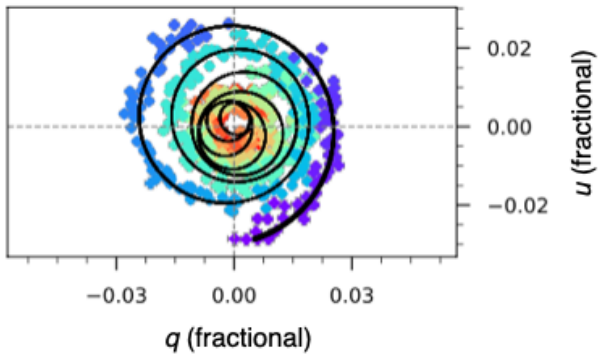

Figure 6.5: Polarization data q as a function of u for source 07, and the corresponding best-fitting model 1T+2ED overplotted (black line). The decrease of the radius indicates depolarization. Figure adapted from the output plot of `RM_Tools`.

Considering the odds ratio and the $\chi^2_{\rm red}$ values, the model 1T+2ED seems to be the best model to describe the depolarization behavior of the source, with one Faraday thin component that represents the instrumental polarization at RM $= -1.15$ rad m^{-2}, and two other components both at around RM $= 6$ rad m^{-2}. Fig 6.4 shows the behavior of the observed q, u, $|p|$ and χ as a function of λ^2, and the curve resulting from the best fit parameters, while Fig. 6.5 shows the observed q as a function of the observed u; the decrease of the radius indicates depolarization. Fig. 6.6 shows, as an example, the posterior distribution of the model 1ED parameters visualized as one-dimensional and two-dimensional projections in a corner plot.

To investigate if the model might not represent the underlying data well, as the $\chi^2_{\rm red}$ is larger than 1, I studied the residuals for q and u. Fig. 6.7 shows the plots of these quantities, normalized by the errors in δq and δu, as a function of λ^2. An initial observation is the presence of outliers in the dataset, which may contribute to the high value of $\chi^2_{\rm red}$. To explore this further, I computed the value of $\chi^2_{\rm red}$ by excluding points where the absolute value of the normalized residual exceeded 6, and progressively lowered the threshold to 3. However, even with these adjustments, the $\chi^2_{\rm red}$ never dropped below approximately 2. I then conducted a visual inspection of the normalized residuals within the

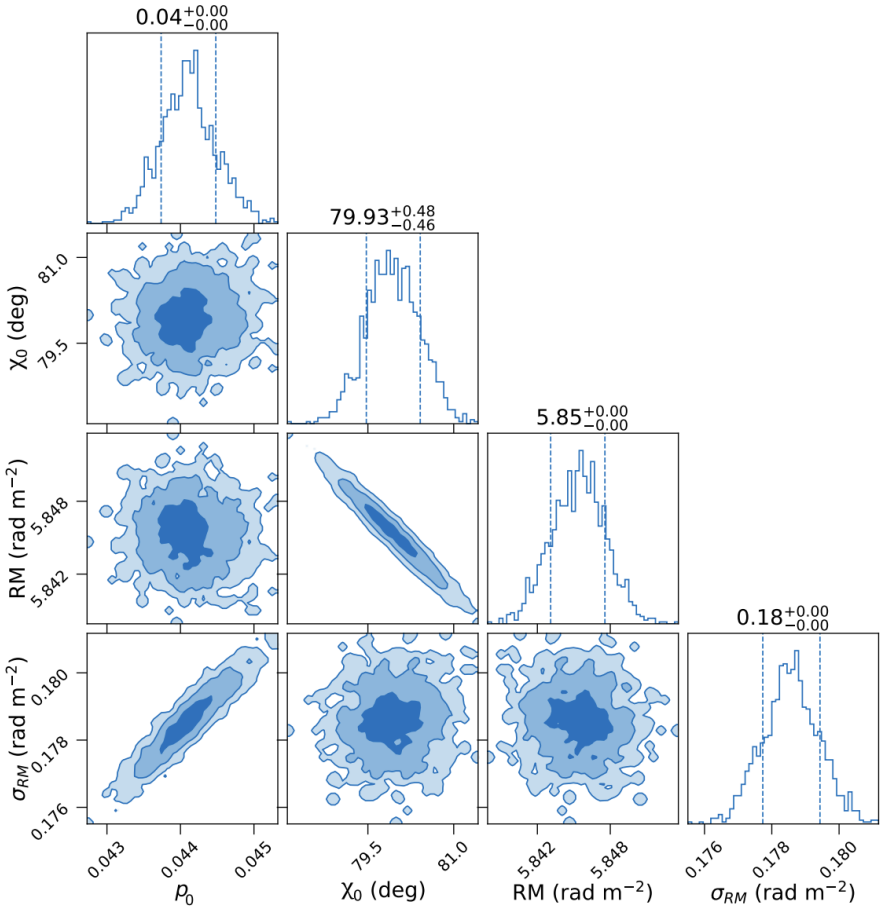

Figure 6.6: Posterior distribution of the model 1ED parameters visualized as one and two-dimensional projections in a corner plot. The corner plot illustrates the distributions and correlations of the parameters in the dataset. The diagonal elements display histograms representing the distribution of each individual parameter. The off-diagonal elements show scatter plots that visualize the relationships between pairs of parameters. Note that the derived values of χ_0 are not meaningful because of the absence of absolute calibration of the polarization angles.

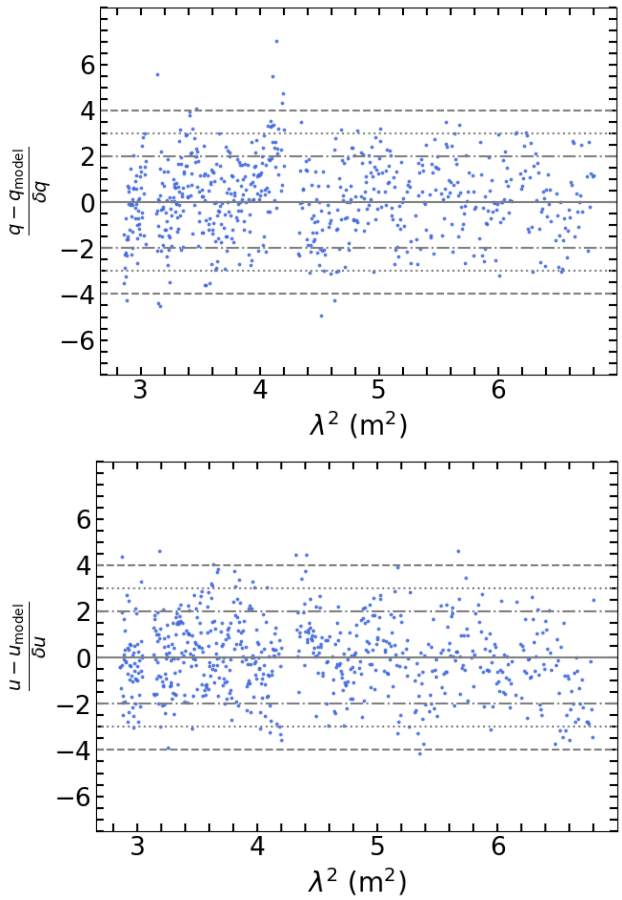

Figure 6.7: Residual q and u normalized by the errors in δq and δu as a function of λ^2.

range of -3 to 3, but found no discernible patterns or structures that would indicate a systematic issue with the model.

The persistently high χ^2_{red} values suggest that the model does not represent well the data or that error estimates are wrong. However, identifying the exact source of the discrepancy is challenging, as it likely stems from a combination of model inadequacies and underestimated noise.

In the context of Bayesian analysis, while evidence is the primary measure for model comparison, the $\chi^2_{\rm red}$ is often included to provide a familiar metric for evaluating fit quality. However, it is important to highlight that the $\chi^2_{\rm red}$ is not the best tool for assessing goodness of fit within a Bayesian framework.

The second best-fitting model is model 1Tk+2ED, where the instrumental polarization is modeled as a pseudo-Faraday-thick components, and other two RM components. The last two RM parameters of 5.9 rad m^{-2} and 6.1 rad m^{-2} are consistent with what was found with the model 1T+2ED.

The instrumental polarization is described as an RM component at around -1.2 rad m^{-2} in all the models that include this component.

It is important to note the intrinsic polarization angle values, χ_0, are not absolute, as we lack a polarization angle calibrator at LOFAR frequencies.

Although it is possible to determine which proposed model best fits the data, the $\chi^2_{\rm red}$ values indicate that no model fully captures the data, suggesting that the models are incomplete and/or the errors are underestimated.

Discussion

The best two models have two RM components due to external dispersion separated by less than the resolution in Faraday depth for the RM synthesis, equal to 0.9 rad m^{-2}. Multiple RM components are due to different regions emitting polarized emission along the line of sight within the beam. As the polarized diffuse emission from the Galaxy is resolved out in our observation and there are not other possible source of polarized emission along the line of sight (such as galaxy clusters or radio halos), the origin of the multiple RM components may be in spatially unresolved structures of the radio galaxy at resolution of $6''$. In fact, as shown in Fig.6.1, at the location of the southern lobe of our radio galaxy at resolution of $0.3''$, i.e. from where we observe polarized emission, we can observe two distinct hotspots, which are unresolved in the image at $6''$. Fig. 6.8 shows the Faraday spectrum of source 07 and the position of RM components fitted with the model 1T+2ED.

An RM component with value of $\sigma_{\rm RM} \sim 0.16$ rad m^{-2} is consistent with all the models. This quantity, which is the dispersion about the mean RM across the source on the sky, is higher for more significant fluctuations in the magnetic field along different lines of sight within the beam. This suggests a more turbulent or irregular magnetic field. Conversely, a smaller $\sigma_{\rm RM}$ suggests a more uniform magnetic field with fewer fluctuations. As shown in Fig. 4.3,

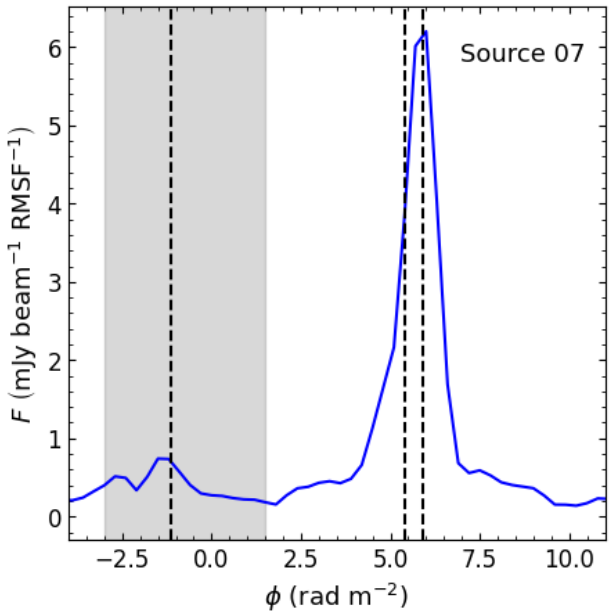

Figure 6.8: Faraday spectrum of source 07 from Cycle 2, and dashed vertical lines at the location of the RM components from the best-fitting model 1T+2ED. The grey region outlines the part of the Faraday spectrum that is expected to be contaminated by instrumental polarization.

we can detect polarized sources with LOFAR with only small amounts of external Faraday depolarization, attributed to the intergalactic magnetic fields (Carretti et al., 2022).

Let us use the derived best-fit values of RM to estimate the strength of the total magnetic field, and of σ_{RM} to estimate the strentgh of the turbulent component of the magnetic field. We consider the Faraday screen that caused external depolarization made of cells of uniform size, electron density and magnetic field strength. We assume also that the magnetic field orientation has random angles in each cell. The observed RM along a line of sight is the result of a random walk process through numerous cells. The expected RM follows a Gaussian distribution with mean equal to zero and variance given

by (Murgia et al., 2004):

$$\sigma^2_{\mathrm{R}M} = 812^2 \lambda_B \int_{l=0}^{l=L} \left(n_e B_\parallel\right)^2 dl \tag{6.6}$$

where n_e is measured in cm^{-3}, $B_\parallel$ in μG, L is the depth of the screen in kpc and λ_B, in kpc, is the coherence scale of the magnetic field[2]. In case of an external Faraday screen, the computed dispersion σ_{RM} provides an upper limit to constrain the turbulent magnetic field strength (e.g. Lawler & Dennison 1982; Murgia et al. 2004; Carretti et al. 2022).

First, we compute the RM due to the extragalactic contribution, i.e. the RRM, using the GRM value reported in Paper II for source 07 and the RM parameters from model 1T+2ED, that is GRM $= 5.17 \pm 2.15$ rad m^{-2}, RM$_2$ $= 5.972 \pm 0.003$ rad m^{-2} and RM$_3$ $= 5.94 \pm 0.03$ rad m^{-2}:

$$\mathrm{RRM}_2 \approx 0.80 \pm 2.15 \ \mathrm{rad\,m^{-2}}\,, \tag{6.7}$$

$$\mathrm{RRM}_3 \approx 0.77 \pm 2.15 \ \mathrm{rad\,m^{-2}}\,. \tag{6.8}$$

Considering a typical value for the electron density in filaments of $n_e = 10^{-5}$ cm^{-3} (Akahori & Ryu, 2010, 2011) and a filament width $L = 3$ Mpc, the strength of the parallel component of the magnetic field to the line of sight of the screen is:

$$B_{\parallel,2} \approx 33 \ \mathrm{nG}\,, \tag{6.9}$$

$$B_{\parallel,3} \approx 32 \ \mathrm{nG}\,, \tag{6.10}$$

and, considering $B_\parallel = B/\sqrt{3}$, a total magnetic field strength of

$$B_2 \approx 57 \ \mathrm{nG}\,, \tag{6.11}$$

$$B_3 \approx 55 \ \mathrm{nG}\,. \tag{6.12}$$

From Eq. 6.6, using the values of n_e and L as above and a coherence length in the range $400 < \lambda_B < 1000$ kpc (according to Carretti et al. 2022), the parallel to the line of sight turbulent component of the magnetic field in the

[2] The coherence scale of a magnetic field is the characteristic length over which the magnetic field maintains a consistent direction and strength. Beyond this scale, the magnetic field tends to change its direction and magnitude due to turbulence or other processes.

screen, $B_{\mathrm{turb},\parallel}$ for $\sigma_{\mathrm{RM},2} = 0.143$ rad m^{-2} and $\sigma_{\mathrm{RM},3} = 0.377$ rad m^{-2} is:

$$0.03 \lesssim B_{\mathrm{turb},\parallel 2} \lesssim 0.05 \text{ n}G\,, \tag{6.13}$$

$$0.08 \lesssim B_{\mathrm{turb},\parallel 3} \lesssim 0.13 \text{ n}G\,, \tag{6.14}$$

while the total turbulent component in the screen, considering $B_{\mathrm{turb},\parallel} = B_{\mathrm{turb}}/\sqrt{3}$, is:

$$0.06 \lesssim B_{\mathrm{turb},2} \lesssim 0.09 \text{ n}G\,,$$

$$0.15 \lesssim B_{\mathrm{turb},3} \lesssim 0.23 \text{ n}G\,.$$

The component B_{turb} is small compared to the total strength of B.

Carretti et al. (2022) estimated a total magnetic field strength of $B = 32.3 \pm 3.2$ nG and a magnetic field strength for the turbulent components of $3.5 < B_{\mathrm{turb}} < 5.3$ nG per cosmic web filament. My results regarding the estimation of the magnetic field, even derived from a single source and having an error comparable to the estimated magnetic field strength itself, are consistent with the broader statistical average of magnetic field strengths observed in the larger sample of 1 003 sources analyzed by Carretti et al. (2022). In contrast, the turbulent component is estimated to be an order of magnitude lower, which may indicate that it is an outlier in the LoTSS-DR2 RM sample.

CHAPTER 7

Summary of included papers

7.1 Paper I

Quantifying the number density and physical characteristics of extragalactic polarized sources is crucial for future Faraday Rotation Measure studies to probe Galactic and intergalactic magnetic fields. In this paper, we presented the deepest and highest-resolution polarization study at 114.9–177.4 MHz to date. The study was carried out on the European Large Area ISO Survey-North 1 (ELAIS-N1) deep field with LOFAR. The ELAIS-N1 LOFAR deep field is the deepest of the LOFAR Two-Metre Sky Survey (LoTSS) deep fields so far, and it was studied at several radio frequencies.

We imaged an area of 25 deg^2 at 6$''$-resolution in the Stokes Q, U parameters. A sensitivity of 19 μJy beam^{-1} was reached in the central region by aligning the polarization angles and stacking datasets from 19 eight-hour-long epochs taken in two different observing cycles.

Twenty-six polarized components were detected above $8\sigma_{\rm QU}$, five of which had not been detected in polarization at any other radio frequencies before. Seven additional polarized components were found by lowering the threshold to $6\sigma_{\rm QU}$ at positions corresponding to sources known to be polarized at

1.4 GHz (Taylor et al., 2009; Grant et al., 2010). In two radio galaxies, polarization was detected from both radio lobes, so the final number of detected radio galaxies is 31. The detected sources are weakly polarized, with a median degree of polarization of 1.75%. The sources previously detected in polarization at 1.4 GHz are significantly depolarized at 150 MHz. The catalog is used to model the polarized source counts at 150 MHz from the counts in total flux density of the LOFAR deep field (Mandal et al., 2021) combined with a function for the fractional polarization depending on the statistical properties of the polarized sources.

7.2 Paper II

The evolution of cosmic magnetic fields along the line of sight can be studied through the behavior with redshift of the Rotation Measure (RM) and the depolarization of extragalactic radio sources. In a first paper, we presented a search for polarized sources in deep observations of the 25-square-degree area of the European Large Area ISO Survey-North 1 (ELAIS-N1) field with the LOw Frequency ARray (LOFAR) at 114.9–177.4 MHz. In this follow-up paper, we investigate the properties of the polarized radio galaxies and use the catalog to produce a rotation measure (RM) and a residual rotation measure (RRM) grid of the field. The classifications of the source properties such as the host galaxy, redshift, morphology, linear size, luminosity, are indeed crucial to identify and study the different underlying populations. In particular, having redshifts and therefore distances of the sources is crucial for distinguishing the different contributions to RM values from magnetic fields at varying distances.

We found that the fractional polarization of the detected radio galaxies increases as their projected linear sizes increase beyond 100 kpc, probably because of their expansion into low-density environments, where the distant hotspots and lobes experience less depolarization.

We studied the environment in the field, and its possible effect on the interaction with the background polarized sources. We found that sources coincident with clusters and superclusters are consistent in their properties with regard to the general population, suggesting that the magnetic fields of these structures are weak and/or with low plasma density. We found a gradient in the RRM grid across the field, consistent with what found in the Galactic RM map of Hutschenreuter et al. (2022), which might be a sign of residual Galactic contamination.

CHAPTER 8

Summary and possible future work

We have presented in this current work new methods to align the polarization angles and stack the $6''$-resolution Stokes Q, U parameter data cubes. The resulting stacked dataset represents the deepest LOFAR polarization data so far, achieving a noise level at the center of the field of 19 μJy beam^{-1}. In this ELAIS-N1 LOFAR deep field (25 deg^2), after stacking data from 19 epochs, we confidently detected polarization in 31 radio sources (1.24 polarized sources per deg^2), within sources that show a variety of morphologies. Although the number density of polarized sources detected is the highest so far at low frequencies, we still suffer from low number statistics. The future optimization of the algorithm for stacking and searching for polarized sources will allow the detections of more polarized sources, and the comparison with other frequencies will give the opportunity to study the depolarization properties of sources and to better understand and discern the different contributions to the Faraday rotation along the line of sight. The developed algorithm can be applied to the large area Northern hemisphere LoTSS survey, in the regions of overlapping of pointings, and to other LOFAR deep fields (GOODS-North, Boötes and Lockman Hole), to help us to characterize them and study the cosmic variance of source properties and intergalactic medium.

Currently, the LOFAR long-baselines Working Group of the Surveys Key Science Project is producing low radio frequency images at the highest resolution in total intensity so far, equal at $0.3''$, through the use of the international baselines. We expect depolarization to be smaller at this resolution, but that is as yet unknown territory.

LOFAR2.0 represents the next step in the LOFAR project, promising to significantly enhance the capabilities of the radio telescope. As a major upgrade to the existing system, LOFAR2.0 is designed to improve both sensitivity and resolution. These enhancements are expected to push the boundaries of what is possible in low-frequency radio astronomy, further solidifying LOFAR's role in cutting-edge astrophysical research.

The advanced capabilities of LOFAR come with substantial challenges, particularly in terms of data management. The telescope generates enormous volumes of data, requiring sophisticated processing and storage solutions.

My work, which is technically challenging due to the nature of polarization observations and the complexities of big data manipulation and analysis, is a step forward in addressing these issues. Our methods could also be used for future generations of radio telescopes such as SKA, of which LOFAR represents the largest precursor in terms of effective area and generated data rates.

Bibliography

Adebahr B., et al., 2022, *The Apertif science verification campaign. Characteristics of polarised radio sources*, A&A, 663, A103

Akahori T., Ryu D., 2010, *Faraday Rotation Measure Due to the Intergalactic Magnetic Field*, ApJ, 723, 476

Akahori T., Ryu D., 2011, *Faraday Rotation Measure due to the Intergalactic Magnetic Field. II. The Cosmological Contribution*, ApJ, 738, 134

An F., et al., 2024, *Radio spectral properties of star-forming galaxies between 150 and 5000 MHz in the ELAIS-N1 field*, MNRAS, 528, 5346

Anderson C. S., O'Sullivan S. P., Heald G. H., Hodgson T., Pasetto A., Gaensler B. M., 2019, *Blazar jet evolution revealed by multi-epoch broadband radio polarimetry*, MNRAS, 485, 3600

Anderson C. S., et al., 2021, *Early Science from POSSUM: Shocks, turbulence, and a massive new reservoir of ionised gas in the Fornax cluster*, PASA, 38, e020

Beck R., Gaensler B. M., 2004, *Observations of magnetic fields in the Milky Way and in nearby galaxies with a Square Kilometre Array*, New Astron. Rev., 48, 1289

Becker R. H., White R. L., Helfand D. J., 1995, *The FIRST Survey: Faint Images of the Radio Sky at Twenty Centimeters*, ApJ, 450, 559

Berger A., Adebahr B., Herrera Ruiz N., Wright A. H., Prandoni I., Dettmar R. J., 2021, *Faint polarised sources in the Lockman Hole field at 1.4 GHz*, A&A, 653, A155

Brentjens M. A., de Bruyn A. G., 2005, *Faraday rotation measure synthesis*, A&A, 441, 1217

Buchner J., et al., 2014, *X-ray spectral modelling of the AGN obscuring region in the CDFS: Bayesian model selection and catalogue*, A&A, 564, A125

Burn B. J., 1966, *On the depolarization of discrete radio sources by Faraday dispersion*, MNRAS, 133, 67

Cantwell T. M., et al., 2020, *Low-frequency observations of the giant radio galaxy NGC 6251*, MNRAS, 495, 143

Carretti E., et al., 2022, *Magnetic field strength in cosmic web filaments*, MNRAS, 512, 945

Carretti E., O'Sullivan S. P., Vacca V., Vazza F., Gheller C., Vernstrom T., Bonafede A., 2023, *Magnetic field evolution in cosmic filaments with LOFAR data*, MNRAS, 518, 2273

Chakraborty A., Dutta P., Datta A., Roy N., 2020, *The study of the angular and spatial distribution of radio-selected AGNs and star-forming galaxies in the ELAIS N1 field*, MNRAS, 494, 3392

Choudhuri A. R., 1998, *The Physics of Fluids and Plasmas: An Introduction for Astrophysicists*. Cambridge University Press, doi:10.1017/CBO9781139171069

Condon J. J., 1984, *Cosmological evolution of radio sources.*, ApJ, 287, 461

Condon J. J., 1988, *Galactic and Extragalactic Radio Astronomy*. Springer

Condon J. J., Ransom S. M., 2016, *Essential Radio Astronomy*. Princeton University Press, doi:10.2307/j.ctv5vdcww

Condon J. J., Cotton W. D., Greisen E. W., Yin Q. F., Perley R. A., Taylor G. B., Broderick J. J., 1998, *The NRAO VLA Sky Survey*, AJ, 115, 1693

Duncan K. J., et al., 2019, *The LOFAR Two-metre Sky Survey. IV. First Data Release: Photometric redshifts and rest-frame magnitudes*, A&A, 622, A3

Duncan K. J., et al., 2021, *The LOFAR Two-meter Sky Survey: Deep Fields Data Release 1. IV. Photometric redshifts and stellar masses*, A&A, 648, A4

Durrer R., Neronov A., 2013, *Cosmological magnetic fields: their generation, evolution and observation*, A&AR, 21, 62

Erceg A., et al., 2022, *Faraday tomography of LoTSS-DR2 data. I. Faraday moments in the high-latitude outer Galaxy and revealing Loop III in polarisation*, A&A, 663, A7

Fan J.-H., et al., 2008, *Radio Polarization Properties for Blazars*, PASJ, 60, 707

Fanaroff B. L., Riley J. M., 1974, *The morphology of extragalactic radio sources of high and low luminosity*, MNRAS, 167, 31P

Farnsworth D., Rudnick L., Brown S., 2011, *Integrated Polarization of Sources at $\lambda \sim 1$ m and New Rotation Measure Ambiguities*, AJ, 141, 191

Feretti L., Giovannini G., Govoni F., Murgia M., 2012, *Clusters of galaxies: observational properties of the diffuse radio emission*, A&AR, 20, 54

Feroz F., Hobson M. P., 2008, *Multimodal nested sampling: an efficient and robust alternative to Markov Chain Monte Carlo methods for astronomical data analyses*, MNRAS, 384, 449

Feroz F., Hobson M. P., Bridges M., 2009, *MULTINEST: an efficient and robust Bayesian inference tool for cosmology and particle physics*, MNRAS, 398, 1601

Feroz F., Hobson M. P., Cameron E., Pettitt A. N., 2019, *Importance Nested Sampling and the MultiNest Algorithm*, The Open Journal of Astrophysics, 2, 10

Ferrière K., West J. L., Jaffe T. R., 2021, *The correct sense of Faraday rotation*, MNRAS, 507, 4968

Gaensler B. M., Landecker T. L., Taylor A. R., POSSUM Collaboration 2010, in American Astronomical Society Meeting Abstracts #215. p. 470.13

George S. J., Stil J. M., Keller B. W., 2012, *Detection Thresholds and Bias Correction in Polarized Intensity*, PASA, 29, 214

Govoni F., et al., 2014, *Cosmic Magnetism Science in the SKA1 Era*, Square Kilometre Array Organisation Science Working Group Assessment Workshop Summary, no. 6, Cosmic Magnetism, 26 pages. Published online by the SKA Organisation, March 2014.

Grant J. K., Taylor A. R., Stil J. M., Landecker T. L., Kothes R., Ransom R. R., Scott D., 2010, *The DRAO Planck Deep Fields: The Polarization Properties of Radio Galaxies at 1.4 GHz*, ApJ, 714, 1689

Gurnett D. A., Bhattacharjee A., 2005, *Introduction to Plasma Physics*. Cambridge University Press, doi:10.1017/9781139226059

Hales C. A., Norris R. P., Gaensler B. M., Middelberg E., 2014a, *ATLAS 1.4 GHz data release 2 - II. Properties of the faint polarized sky*, MNRAS, 440, 3113

Hales C. A., et al., 2014b, *ATLAS 1.4 GHz Data Release 2 - I. Observations of the CDF-S and ELAIS-S1 fields and methods for constructing differential number counts*, MNRAS, 441, 2555

Hardcastle M. J., et al., 2023, *The LOFAR Two-Metre Sky Survey. VI. Optical identifications for the second data release*, A&A, 678, A151

Hatanaka T., 1956, *The Faraday Effect in the Earth's Ionosphere with Special Reference to Polarization Measurements of the Solar Radio Emission*, PASJ, 8, 73

Heald G., 2009, in Strassmeier K. G., Kosovichev A. G., Beckman J. E., eds, Vol. 259, Cosmic Magnetic Fields: From Planets, to Stars and Galaxies. pp 591–602, doi:10.1017/S1743921309031421

Heald G., et al., 2020, *Magnetism Science with the Square Kilometre Array*, Galaxies, 8, 53

Heesen V., et al., 2023, *Detection of magnetic fields in the circumgalactic medium of nearby galaxies using Faraday rotation*, A&A, 670, L23

Herrera Ruiz N., et al., 2021, *LOFAR Deep Fields: probing a broader population of polarized radio galaxies in ELAIS-N1*, A&A, 648, A12

Hopkins A. M., Afonso J., Chan B., Cram L. E., Georgakakis A., Mobasher B., 2003, *The Phoenix Deep Survey: The 1.4 GHz Microjansky Catalog*, AJ, 125, 465

Hotan A. W., et al., 2021, *Australian square kilometre array pathfinder: I. system description*, PASA, 38, e009

Hutschenreuter S., et al., 2022, *The Galactic Faraday rotation sky 2020*, A&A, 657, A43

Jelić V., et al., 2014, *Initial LOFAR observations of epoch of reionization windows. II. Diffuse polarized emission in the ELAIS-N1 field*, A&A, 568, A101

Johnston-Hollitt M., et al., 2015, in Advancing Astrophysics with the Square Kilometre Array (AASKA14). p. 92 (arXiv:1506.00808), doi:10.22323/1.215.0092

Kass R., Raftery A., 1995, *Bayes factors*, Journal of the American Statistical Association, pp 773–795

Klein U., Fletcher A., 2015, *Galactic and Intergalactic Magnetic Fields*. Springer, doi:10.1007/978-3-319-08942-3

Kobayashi H., Mark B. L., Turin W., 2012, *Probability, Random Processes and Statistical Analysis*. Cambridge University Press, doi:10.1017/CBO9780511977770

Kondapally R., et al., 2021, *The LOFAR Two-meter Sky Survey: Deep Fields Data Release 1. III. Host-galaxy identifications and value added catalogues*, A&A, 648, A3

Lacy M., et al., 2020, *The Karl G. Jansky Very Large Array Sky Survey (VLASS). Science Case and Survey Design*, PASP, 132, 035001

Lawler J. M., Dennison B., 1982, *On intracluster Faraday rotation. II - Statistical analysis.*, ApJ, 252, 81

Mahatma V. H., et al., 2019, *LoTSS DR1: Double-double radio galaxies in the HETDEX field*, A&A, 622, A13

Mahatma V. H., Hardcastle M. J., Harwood J., O'Sullivan S. P., Heald G., Horellou C., Smith D. J. B., 2021, *A low-frequency study of linear polarization in radio galaxies*, MNRAS, 502, 273

Mandal S., et al., 2021, *Extremely deep 150 MHz source counts from the LoTSS Deep Fields*, A&A, 648, A5

Mao S. A., Zweibel E., Fletcher A., Ott J., Tabatabaei F., 2015, *Properties of the Magneto-ionic Medium in the Halo of M51 Revealed by Wide-band Polarimetry*, ApJ, 800, 92

Matthews A. M., Condon J. J., Cotton W. D., Mauch T., 2021, *Cosmic Star Formation History Measured at 1.4 GHz*, ApJ, 914, 126

Mesa D., Baccigalupi C., De Zotti G., Gregorini L., Mack K. H., Vigotti M., Klein U., 2002, *Polarization properties of extragalactic radio sources and their contribution to microwave polarization fluctuations*, A&A, 396, 463

Morabito L. K., et al., 2022, *Sub-arcsecond imaging with the International LOFAR Telescope. I. Foundational calibration strategy and pipeline*, A&A, 658, A1

Mulcahy D. D., et al., 2014, *The nature of the low-frequency emission of M 51. First observations of a nearby galaxy with LOFAR*, A&A, 568, A74

Murgia M., Govoni F., Feretti L., Giovannini G., Dallacasa D., Fanti R., Taylor G. B., Dolag K., 2004, *Magnetic fields and Faraday rotation in clusters of galaxies*, A&A, 424, 429

Murray W. A. S., Hargreaves J. K., 1954, *Lunar Radio Echoes and the Faraday Effect in the Ionosphere*, Nature, 173, 944

Neld A., et al., 2018, *Reliable detection and characterization of low-frequency polarized sources in the LOFAR M51 field*, A&A, 617, A136

O'Sullivan S., Stil J., Taylor A. R., Ricci R., Grant J. K., Shorten K., 2008, in The role of VLBI in the Golden Age for Radio Astronomy. p. 107 (arXiv:0902.1995), doi:10.22323/1.072.0107

O'Sullivan S. P., et al., 2012, *Complex Faraday depth structure of active galactic nuclei as revealed by broad-band radio polarimetry*, MNRAS, 421, 3300

O'Sullivan S. P., Purcell C. R., Anderson C. S., Farnes J. S., Sun X. H., Gaensler B. M., 2017, *Broad-band, radio spectro-polarimetric study of 100 radiative-mode and jet-mode AGN*, MNRAS, 469, 4034

O'Sullivan S. P., et al., 2019, *The intergalactic magnetic field probed by a giant radio galaxy*, A&A, 622, A16

O'Sullivan S. P., et al., 2020, *New constraints on the magnetization of the cosmic web using LOFAR Faraday rotation observations*, MNRAS, 495, 2607

O'Sullivan S. P., et al., 2023, *The Faraday Rotation Measure Grid of the LOFAR Two-metre Sky Survey: Data Release 2*, MNRAS, 519, 5723

Ocran E. F., Taylor A. R., Vaccari M., Ishwara-Chandra C. H., Prandoni I., 2020, *Deep GMRT 610 MHz observations of the ELAIS N1 field: catalogue and source counts*, MNRAS, 491, 1127

Oliver S., et al., 2000, *The European Large Area ISO Survey - I. Goals, definition and observations*, MNRAS, 316, 749

Osinga E., et al., 2021, *Diffuse radio emission from galaxy clusters in the LOFAR Two-metre Sky Survey Deep Fields*, A&A, 648, A11

Pasetto A., 2021, *Message in a Bottle: Unveiling the Magneto-Ionic Complexity of AGNs through the Stokes QU-Fitting Technique*, Galaxies, 9, 56

Pasetto A., Carrasco-González C., O'Sullivan S., Basu A., Bruni G., Kraus A., Curiel S., Mack K.-H., 2018, *Broadband radio spectro-polarimetric observations of high-Faraday-rotation-measure AGN*, A&A, 613, A74

Piras S., et al., 2024, *LOFAR Deep Fields: Probing the sub-mJy regime of polarized extragalactic sources in ELAIS-N1. I. The catalog*, A&A, 687, A267

Puglisi G., et al., 2018, *Forecasting the Contribution of Polarized Extragalactic Radio Sources in CMB Observations*, ApJ, 858, 85

Purcell C. R., Van Eck C. L., West J., Sun X. H., Gaensler B. M., 2020, *RM-Tools: Rotation measure (RM) synthesis and Stokes QU-fitting*, Astrophysics Source Code Library, record ascl:2005.003

Reissl S., et al., 2023, *A reproduction of the Milky Way's Faraday rotation measure map in galaxy simulations from global to local scales*, Nature Astronomy, 7, 1295

Rengelink R. B., Tang Y., de Bruyn A. G., Miley G. K., Bremer M. N., Roettgering H. J. A., Bremer M. A. R., 1997, *The Westerbork Northern Sky Survey (WENSS), I. A 570 square degree Mini-Survey around the North Ecliptic Pole*, A&AS, 124, 259

Riseley C. J., et al., 2018, *The POlarised GLEAM Survey (POGS) I: First results from a low-frequency radio linear polarisation survey of the southern sky*, PASA, 35, e043

Riseley C. J., et al., 2020, *The POlarised GLEAM Survey (POGS) II: Results from an all-sky rotation measure synthesis survey at long wavelengths*, PASA, 37, e029

Robishaw T., Heiles C., 2021, in Wolszczan A., ed., , The WSPC Handbook of Astronomical Instrumentation, Volume 1: Radio Astronomical Instrumentation. pp 127–158, doi:10.1142/9789811203770_0006

Rowan-Robinson M., et al., 2004, *The European Large-Area ISO Survey (ELAIS): the final band-merged catalogue*, MNRAS, 351, 1290

Rudnick L., Owen F. N., 2014, *The Distribution of Polarized Radio Sources >15 μJy in GOODS-N*, ApJ, 785, 45

Rybicki G. B., Lightman A. P., 1979, *Radiative processes in astrophysics.* Wiley-VCH

Ryle M., Scheuer P. A. G., 1955, *The Spatial Distribution and the Nature of Radio Stars*, Proceedings of the Royal Society of London Series A, 230, 448

Sabater J., et al., 2021, *The LOFAR Two-meter Sky Survey: Deep Fields Data Release 1. II. The ELAIS-N1 LOFAR deep field*, A&A, 648, A2

Saikia D. J., Salter C. J., 1988, *Polarization properties of extragalactic radio sources.*, ARA&A, 26, 93

Schnitzeler D. H. F. M., Carretti E., Wieringa M. H., Gaensler B. M., Haverkorn M., Poppi S., 2019, *S-PASS/ATCA: a window on the magnetic universe in the Southern hemisphere*, MNRAS, 485, 1293

Shimwell T. W., et al., 2017, *The LOFAR Two-metre Sky Survey. I. Survey description and preliminary data release*, A&A, 598, A104

Shimwell T. W., et al., 2019, *The LOFAR Two-metre Sky Survey. II. First data release*, A&A, 622, A1

Shimwell T. W., et al., 2022, *The LOFAR Two-metre Sky Survey. V. Second data release*, A&A, 659, A1

Simonte M., Andernach H., Brüggen M., Best P. N., Osinga E., 2023, *Revisiting the alignment of radio galaxies in the ELAIS-N1 field*, A&A, 672, A178

Simonte M., Andernach H., Brüggen M., Miley G. K., Barthel P., 2024, *Giant radio galaxies in the LOFAR deep fields*, A&A, 686, A21

Sirothia S. K., Dennefeld M., Saikia D. J., Dole H., Ricquebourg F., Roland J., 2009, *325-MHz observations of the ELAIS-N1 field using the Giant Metrewave Radio Telescope*, MNRAS, 395, 269

Sokoloff D. D., Bykov A. A., Shukurov A., Berkhuijsen E. M., Beck R., Poezd A. D., 1998, *Depolarization and Faraday effects in galaxies*, MNRAS, 299, 189

Sotomayor-Beltran C., et al., 2013, *Calibrating high-precision Faraday rotation measurements for LOFAR and the next generation of low-frequency radio telescopes*, A&A, 552, A58

Stil J. M., Keller B. W., George S. J., Taylor A. R., 2014, *Degree of Polarization and Source Counts of Faint Radio Sources from Stacking Polarized Intensity*, ApJ, 787, 99

Stuardi C., et al., 2020, *The LOFAR view of intergalactic magnetic fields with giant radio galaxies*, A&A, 638, A48

Subrahmanyan R., Ekers R. D., Saripalli L., Sadler E. M., 2010, *ATLBS: the Australia Telescope Low-Brightness Survey*, MNRAS, 402, 2792

Sun X. H., et al., 2015, *Comparison of Algorithms for Determination of Rotation Measure and Faraday Structure. I. 1100-1400 MHz*, AJ, 149, 60

Tasse C., et al., 2021, *The LOFAR Two-meter Sky Survey: Deep Fields Data Release 1. I. Direction-dependent calibration and imaging*, A&A, 648, A1

Taylor A. R., et al., 2007, *Radio Polarimetry of the ELAIS N1 Field: Polarized Compact Sources*, ApJ, 666, 201

Taylor A. R., Stil J. M., Sunstrum C., 2009, *A Rotation Measure Image of the Sky*, ApJ, 702, 1230

Thomson A. J. M., et al., 2021, *The Global Magneto-Ionic Medium Survey (GMIMS): the brightest polarized region in the southern sky at 75 cm and its implications for Radio Loop II*, MNRAS, 507, 3495

Thomson A. J. M., et al., 2023, *The Rapid ASKAP Continuum Survey III: Spectra and Polarisation In Cutouts of Extragalactic Sources (SPICE-RACS) first data release*, PASA, 40, e040

Tucci M., Toffolatti L., 2012, *The Impact of Polarized Extragalactic Radio Sources on the Detection of CMB Anisotropies in Polarization*, Advances in Astronomy, 2012, 624987

Tucci M., Martínez-González E., Toffolatti L., González-Nuevo J., De Zotti G., 2004, *Predictions on the high-frequency polarization properties of extragalactic radio sources and implications for polarization measurements of the cosmic microwave background*, MNRAS, 349, 1267

Urry C. M., Padovani P., 1995, *Unified Schemes for Radio-Loud Active Galactic Nuclei*, PASP, 107, 803

Vacca V., et al., 2016, *Using rotation measure grids to detect cosmological magnetic fields: A Bayesian approach*, A&A, 591, A13

Vacca V., et al., 2022, *Puzzling large-scale polarization in the galaxy cluster Abell 523*, MNRAS, 514, 4969

Vaccari M., et al., 2005, *Final analysis of ELAIS 15-μm observations: method, reduction and catalogue*, MNRAS, 358, 397

Van Eck C. L., et al., 2017, *Faraday tomography of the local interstellar medium with LOFAR: Galactic foregrounds towards IC 342*, A&A, 597, A98

Van Eck C. L., et al., 2018, *Polarized point sources in the LOFAR Two-meter Sky Survey: A preliminary catalog*, A&A, 613, A58

Van Eck C. L., et al., 2023, *RMTable2023 and PolSpectra2023: Standards for Reporting Polarization and Faraday Rotation Measurements of Radio Sources*, ApJA, 267, 28

Vanderwoude S., et al., 2024, *Prototype Faraday Rotation Measure Catalogs from the Polarisation Sky Survey of the Universe's Magnetism (POSSUM) Pilot Observations*, AJ, 167, 226

Vernstrom T., Gaensler B. M., Rudnick L., Andernach H., 2019, *Differences in Faraday Rotation between Adjacent Extragalactic Radio Sources as a Probe of Cosmic Magnetic Fields*, ApJ, 878, 92

Vernstrom T., Heald G., Vazza F., Galvin T. J., West J. L., Locatelli N., Fornengo N., Pinetti E., 2021, *Discovery of magnetic fields along stacked cosmic filaments as revealed by radio and X-ray emission*, MNRAS, 505, 4178

White R. L., Becker R. H., Helfand D. J., Gregg M. D., 1997, *A Catalog of 1.4 GHz Radio Sources from the FIRST Survey*, ApJ, 475, 479

Williams W. L., et al., 2019, *The LOFAR Two-metre Sky Survey. III. First data release: Optical/infrared identifications and value-added catalogue*, A&A, 622, A2

Wilson T. L., Rohlfs K., Hüttemeister S., 2013, *Tools of Radio Astronomy*, doi:10.1007/978-3-642-39950-3.

Xu Y., Kronberg P. P., Habib S., Dufton Q. W., 2006, *A Faraday Rotation Search for Magnetic Fields in Large-scale Structure*, ApJ, 637, 19

de Gasperin F., et al., 2021, *The LOFAR LBA Sky Survey. I. Survey description and preliminary data release*, A&A, 648, A104

de Gasperin F., et al., 2023, *The LOFAR LBA Sky Survey. II. First data release*, A&A, 673, A165

de Jong J. M. G. H. J., et al., 2024, *Into the depths: Unveiling ELAIS-N1 with LOFAR's deepest sub-arcsecond wide-field images*, arXiv e-prints, p. arXiv:2407.13247

Šlaus B., et al., 2024, *The XXL survey. LII. The evolution of radio AGN LF determined via parametric methods from GMRT, ATCA, VLA, and Cambridge interferometer observations*, A&A, 684, A19

Šnidarić I., et al., 2023, *LOFAR Deep Fields: Probing faint Galactic polarised emission in ELAIS-N1*, A&A, 674, A119

APPENDIX A

Appendix

A.1 Complex fractional polarization from two RM components interfering inside the beam.

The polarized radio signal that traverses multiple Faraday-rotating and/or emitting regions experiences a combination of depolarization mechanisms along the line of sight and/or within the beam. In this section I calculate the polarization that results from the interference of two RM components within the beam.

Let us consider two polarized signals, p_1 and p_2, each described by a Faraday thin screen. The complex fractional polarization of each signal is:

$$p_1 = \mathrm{p}_{0,1} e^{2i(\chi_{0,1} + \mathrm{RM}_1 \lambda^2)} \,, \tag{A.1}$$

$$p_2 = \mathrm{p}_{0,2} e^{2i(\chi_{0,2} + \mathrm{RM}_2 \lambda^2)} \,. \tag{A.2}$$

If the two signals are interfering inside the beam, the total complex frac-

tional polarization we observe, $p_{\rm tot}$, is given by $p_{\rm tot} = p_1 + p_2$:

$$p_{\rm tot} = p_1 + p_2 = \mathrm{p}_{0,1} e^{2i(\chi_{0,1}+\mathrm{RM}_1\lambda^2)} + \mathrm{p}_{0,2} e^{2i(\chi_{0,2}+\mathrm{RM}_2\lambda^2)} \,. \tag{A.3}$$

Let us compute the square of the modulus of $p_{\rm tot}$, $|p_{\rm tot}|^2$:

$$\begin{aligned}
|p_{\rm tot}|^2 &= (p_1 + p_2)\,(p_1^* + p_2^*) && \text{(A.4)}\\
&= p_1\,p_1^* + p_2\,p_2^* + p_1\,p_2^* + p_1^*\,p_2 && \text{(A.5)}\\
&= |p_1|^2 + |p_2|^2 + \mathrm{p}_{0,1}\mathrm{p}_{0,2} e^{2i(\chi_{0,1}+\mathrm{RM}_1\lambda^2)} e^{-2i(\chi_{0,2}+\mathrm{RM}_2\lambda^2)} && \text{(A.6)}\\
&+ \mathrm{p}_{0,1}\mathrm{p}_{0,2} e^{-2i(\chi_{0,1}+\mathrm{RM}_1\lambda^2)} e^{2i(\chi_{0,2}+\mathrm{RM}_2\lambda^2)} && \text{(A.7)}\\
&= |p_1|^2 + |p_2|^2 + \mathrm{p}_{0,1}\mathrm{p}_{0,2} e^{2i(\chi_{0,1}-\chi_{0,2}+\mathrm{RM}_1\lambda^2-\mathrm{RM}_2\lambda^2)} && \text{(A.8)}\\
&+ \mathrm{p}_{0,1}\mathrm{p}_{0,2} e^{-2i(\chi_{0,1}-\chi_{0,2}+\mathrm{RM}_1\lambda^2-\mathrm{RM}_2\lambda^2)} \,, && \text{(A.9)}
\end{aligned}$$

and using the Euler's formula:

$$|p_{\rm tot}|^2 = |p_1|^2 + |p_2|^2 + 2\mathrm{p}_{0,1}\mathrm{p}_{0,2}\cos[2(\chi_{0,1} - \chi_{0,2} + \mathrm{RM}_1\lambda^2 - \mathrm{RM}_2\lambda^2)] \,. \tag{A.10}$$

The modulus of $p_{\rm tot}$ is then :

$$|p_{\rm tot}| = \sqrt{|p_1|^2 + |p_2|^2 + 2\mathrm{p}_{0,1}\mathrm{p}_{0,2}\cos[2(\chi_{0,1} - \chi_{0,2} + \mathrm{RM}_1\lambda^2 - \mathrm{RM}_2\lambda^2)]} \,. \tag{A.11}$$

Eq. A.11 shows that the modulus of the complex fractional polarization resulting from the sum of two interfering Faraday thin screens is modulated by a cosine function depending on the RM and χ_0 of the components. Fig A.1 shows the behaviors of the modulus of the two complex fractional polarization p_1 and p_2 in the LOFAR frequency range 115–177 MHz, which are constant as a function of λ^2. The sum of these two signals, $p_{\rm tot}$, leads to a repolarization across the band.

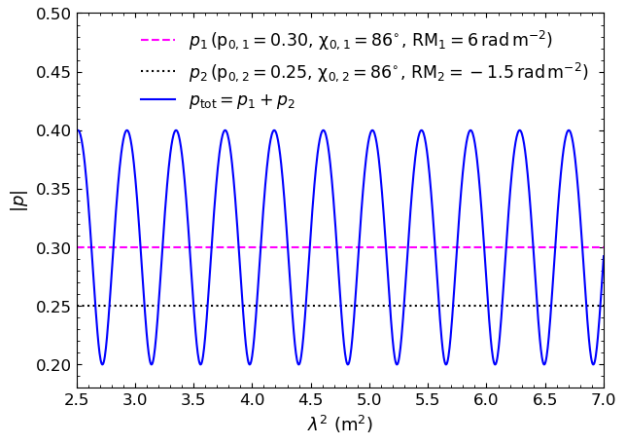

Figure A.1: Simulation of two interfering Faraday thin screen components, p_1 and p_2, in the LOFAR frequency range 115–177 MHz. The modulus of the resulting $p_{\rm tot} = p_1 + p_2$ shows repolarization across the band.